

© 2016 by Trent Graham. All rights reserved.

USING HYPERENTANGLEMENT FOR ADVANCED QUANTUM COMMUNICATION

BY

TRENT GRAHAM

DISSERTATION

Submitted in partial fulfillment of the requirements
for the degree of Doctor of Philosophy in Physics
in the Graduate College of the
University of Illinois at Urbana-Champaign, 2016

Urbana, Illinois

Doctoral Committee:

Professor Dale Van Harlingen, Chair
Professor Paul Kwiat, Director of Research
Professor David Ceperley
Professor Jen-Chieh Peng
Professor Taylor Hughes

Abstract

The field of quantum information science promises incredible enhancements in computing, metrology, simulation, and communication, but the challenge of creating, manipulating, and measuring the large quantum states has limited current implementations of such techniques. Such limitations affect photonic quantum information in particular, because photons lack the strong nonlinear interactions required for building up many-particle entangled states and performing multi-photon gates; nevertheless, because photons are currently the only “flying qubit”, i.e., qubits that are mobile, they are a required resource for quantum communication protocols. One strategy to partially mitigate this limitation is to encode multiple entangled qubits on the different degrees of freedom of a single pair of photons. Such “hyperentangled” quantum states may be created with enough qubits to enable a whole new class of quantum information experiments. Furthermore, while nonlinear interactions are required to implement multi-qubit gates between qubits encoded on different particles, such gates can be implemented between qubits encoded on the same particle using only linear elements, enabling a much broader class of measurements. We use hyperentangled states to implement various quantum communication and quantum metrology protocols. Specifically, we demonstrate that hyperentangled photons can be used to increase the classical channel capacity of a quantum channel, transport quantum information between two remote parties efficiently and deterministically, and efficiently characterize quantum channels. We will discuss how to produce, manipulate, and measure hyperentangled states and discuss how entanglement in multiple degrees of freedom enables each technique. Finally, we discuss the limitations of each of these techniques and how they might be improved as technology advances.

To my family.

Acknowledgments

This work would not have been possible without the help of many coworkers and collaborators. In particular, I would like to thank Herbert Bernstein, Tzu-Chieh Wei, and Marius Junge for providing assistance with theoretical calculations for the superdense teleportation experiments in Chapter III; Joseph Chapman for performing the tabletop beacon stabilization experiments in Chapter IV; Christopher Zeitler for helping with entanglement source bandwidth measurements and with preliminary superdense teleportation measurements in Chapter IV; and Julio Barreiro for performing initial experimental setup for the direct characterization of quantum dynamics experiments described in Chapter V. In addition, I would like to thank Thomas Jennewein, Vadim Makarov, Elena Anisimova, Brendon Higgins, and Jean-Philippe Bourgoin at the Institute for Quantum Computing at Waterloo for fitting us into their detector radiation experiments at TRIUMF accelerator; Kevin Zielnicki for help designing the mount for the radiation experiment; Michael Goggin and Fumihiro Kaneda for performing optical annealing experiments; and Daniel Kumor and Bradley Christensen for helping me setup time-tagging electronics. I am also very grateful to my labmate Rebecca Holmes and my wife, Carla Graham, for sacrificing a great deal of their time helping me edit this thesis.

Finally, I would like to thank my advisor, Paul Kwiat, for providing guidance and assistance in nearly every aspect of my graduate career. From helping with experimental design to setting up collaborations to editing all of my papers and thesis, Paul has been the key figure guiding my development as a scientist.

I would also like to acknowledge a number of funding agencies for financially supporting the experiments described in this work. Experiments described in Chapter II were supported by the Office of Naval Research (ONR) grant N000141210487 and NSF grant No. PHYS 12-05870. Experiments described in Chapter III were supported by NSF Grant No. PHY-0903865, the NASA NIAC Program and NASA Grant No. NNX13AP35A and partially supported by National Science Foundation Grants DMS-1201886, No. PHY 1314748 and No. PHY 1333903. Experiments described in chapter IV were supported by the NASA NIAC Program and NASA Grant No. NNX13AP35A. Experiments described in Chapter V were supported by NSF Grant No. PHY-0903865, the ADNA/S&T-IARPA project Hyperentanglement Enhanced Advanced Quantum Communication (NBCHC070006), the QuISM MURI Program, and the DARPA QuBE program.

Table of Contents

List of Tables	vii
List of Figures	viii
List of Abbreviations	x
Chapter 1 Introduction to Photonic Quantum Communication	
1.1 Quantum Information and Communication	1
1.2 Photonic Degrees of Freedom	2
1.2.1 Polarization	3
1.2.2 Temporal Mode	4
1.2.3 Spatial Mode	5
1.2.4 Hybrid Modes	6
1.3 Entanglement	7
1.3.1 Polarization Entanglement	8
1.3.2 Temporal-Mode Entanglement	11
1.3.3 Spatial-Mode Entanglement	13
1.4 Hyperentanglement	14
Chapter 2 Hyperdense Coding	
2.1 Quantum-Enhanced Classical Communication	16
2.1.1 Superdense Coding	16
2.1.2 Linear Optical Bell-State Measurements	18
2.2 Hyperentanglement-Enhanced Classical Communication	20
2.2.1 Hyperentanglement-Enabled Bell-State Measurement	20
2.2.2 Hyperdense Coding	22
2.2.3 Turbulence-Resistant Hyperentanglement	24
2.3 Experimental Implementation	25
2.3.1 State Creation	25
2.3.2 Hyper-Bell-State Manipulation	26
2.3.3 Hyper-Bell-State Measurement	28
2.3.4 Experimental Results	30
2.4 Outlook	31
Chapter 3 Spatial Superdense Teleportation	
3.1 Introduction	34
3.1.1 Quantum Teleportation and Remote State Preparation	34
3.2 Superdense Teleportation	39
3.3 Experimental Implementation	41
3.3.1 Hyperentangled State Creation	41
3.3.2 Quantum Message Encoding and Measurement	41
3.4 State verification through tomographic reconstruction	43

3.5 Discussion	45
3.5.1 Extending to Feed-Forward Correction	48
3.6 Conclusion and Outlook	49
Chapter 4 Designing Quantum Communication Systems for Satellites	51
4.1 Introduction	51
4.1.1 Transmitting Photonic Qubits from a Satellite	52
4.2 Superdense Teleportation	53
4.3 Experimental Prototyping	54
4.3.1 Source Development	54
4.3.2 Quantum Message Encoding and Measurement	56
4.4 Adapting for Space Applications	60
4.4.1 Satellite Beacon	60
4.4.2 Downconversion Link Analysis	64
4.4.3 Hyperentanglement Source Miniaturization	69
4.4.4 Modifications for Feed-Forward Operation	71
4.5 Quantum Key Distribution	72
4.5.1 Modifications for Quantum Key Distribution	74
Chapter 5 Quantum Channel Characterization	76
5.1 Introduction	76
5.2 Quantum Process Characterization	78
5.3 Experimental Implementation	79
5.3.1 Input State Creation	79
5.3.2 Bell State Measurement	80
5.3.3 Experimental Results	81
5.3.4 Error Compensation	82
5.3.5 Partial Process Characterization	82
5.4 Experimental Details	85
5.4.1 Source	85
5.4.2 Error Compensation	85
5.4.3 Remaining Error Sources	87
5.4.4 Scaling to Higher Dimensions	88
5.5 Outlook	89
Chapter 6 Conclusions	90
Appendix A Hybrid versus Hyperentangled Superdense Coding	91
Appendix B General versus Equimodular State Space Comparisons	93
B.1 Packing Number and Volume Ratio	93
B.2 Classical Teleportation Fidelity	94
Appendix C Using Pockels Cells and Liquid Crystals	97
Appendix D Designing Holograms	101
Appendix E Tomographic Reconstruction of Quantum States	104
E.1 Representation of Quantum states	104
E.2 Maximum Likelihood State Estimation	105
E.3 Problems With Maximum Likelihood	106
Appendix F Detector Annealing	108
Appendix G Active Stabilization of Interferometers	110
References	113

List of Tables

2.1	Parity of two-qubit hyper-Bell states.	23
2.2	Detector signatures of two-qubit hyper-Bell states.	24
2.3	Channel capacity comparison of classical and entanglement-enhanced encoding techniques.	32
3.1	Resource comparison of entanglement-enhanced quantum state communication techniques.	40
3.2	List of state parameters transmitted with superdense teleportation.	45
3.3	Using Pockels cells to perform feed-forward correction of polarization- and spatial-mode states.	48
4.1	Using Pockels cells to perform feed-forward correction of polarization- and temporal-mode states.	72
5.1	List of pump laser powers used during different quantum processes measurements.	85

List of Figures

1.1	Bloch sphere representation of qubits.	3
1.2	Methods of encoding qubits on different photonic degrees of freedom.	5
1.3	Birefringent phase-matching in spontaneous parametric downconversion	7
1.4	Types of polarization entanglement sources.	10
1.5	Temporal-mode entanglement source.	12
1.6	Orbital angular momentum entanglement source.	13
1.7	Hyperentanglement source.	14
2.1	Schematic of superdense coding.	17
2.2	Single-qubit Bell state analyzer.	20
2.3	Polarization- and spatial-mode controlled-NOT gate.	22
2.4	Two-qubit Bell state analyzer.	23
2.5	Experimental hyperdense coding layout.	25
2.6	Hyper-Bell state encoding schemes	26
2.7	Polarization- and temporal-mode Bell state analyzer.	29
2.8	Channel capacity susceptibility plot.	31
3.1	Quantum teleportation and remote state preparation layout.	36
3.2	d -dimensional probabilistic remote state preparation.	37
3.3	Classical communication resource comparison plot.	40
3.4	Experimental setup for superdense teleportation of polarization and orbital angular momentum states	42
3.5	Experimentally reconstructed density matrices of uncorrected states.	43
3.6	Toroidal representation of remotely prepared states.	44
3.7	Reconstructed density matrices of numerically corrected density matrices.	46
3.8	Measurement of the nonlocal interference fringe of Bob's photon	47
3.9	Experimental strategy for feed-forward correction of Bob's state.	49
4.1	Experimental setup for polarization- and temporal-mode superdense teleportation.	54
4.2	Bandwidth measurement of 1550-nm downconversion photons.	57
4.3	Polarization and temporal-mode measurement strategy.	58
4.4	Polarization- and temporal-mode states transmitted using superdense teleportation.	59
4.5	Density matrix reconstructions of polarization- and temporal-mode states	59
4.6	Schematic of a satellite-to-ground implementation of superdense teleportation	60
4.7	Doppler-induced phase between temporal modes.	62
4.8	Table-top phase stabilization setup.	63
4.9	Multi-spatial-mode temporal-mode measurement strategy.	66
4.10	Waveguide entanglement source.	70
4.11	Experimental strategy for feed-forward correction of polarization- and temporal-mode states.	72
4.12	Schematic of quantum key distribution.	73
4.13	Experimental layout for polarization- and temporal-mode hyperentanglement-based quantum key distribution	74

5.1	Schematic for standard quantum process tomography and direct characterization of quantum dynamics.	78
5.2	Experimental implementation of direct characterization of quantum dynamics.	81
5.3	Experimental implementation of several quantum processes.	83
5.4	Experimentally reconstructed quantum process matrices.	84
5.5	Strategy to compensate for errors in direct characterization of quantum dynamics measurements. .	86
5.6	Tomographically reconstructed density matrices representing the input states used in direct characterization of quantum dynamics.	87
5.7	Strategy to scale direct characterization of quantum dynamics to larger-dimensional quantum processes.	89
A.1	Single-photon, two-qubit classical communication scheme.	92
C.1	Liquid crystal diagram	98
C.2	An X-cut RTP Pockels cell	100
D.1	Hologram transmission screen layout	102
D.2	Spatial qubit tomography hologram gratings	103
F.1	Dark count reduction of radiated detectors using optical annealing.	109
G.1	Feedback system for stabilizing interferometers	111
G.2	Interferometer stabilization set point	112

List of Abbreviations

AAPT	Ancilla-Assisted Process Tomography
BBO	Barium Borate
BiBO	Bismuth Borate
CNOT	Controlled-NOT
DCQD	Direct Characterization of Quantum Dynamics
DM	Dichroic Mirror
HOM	Hong-Ou-Mandel
HWP	Half-waveplate
PBS	Polarizing Beamsplitter
POVM	Positive-Operator Valued Measure.
PPLN	Periodically-Poled Lithium Niobate
QPT	Quantum Process Tomography
QT	Quantum Teleportation
QWP	Quarter-Waveplate
RSP	Remote State Preparation
RTP	Rubidium Titanyl Phosphate
SDT	Superdense Teleportation
SPDC	Spontaneous Parametric Downconversion
SQPT	Standard Quantum Process Tomography

Chapter 1

Introduction to Photonic Quantum Communication

1.1 Quantum Information and Communication

Over the past 25 years, physics has seen the rise of a new field of study—quantum information science—which aims to describe how information is manipulated, stored, and measured at its most basic level. This is a difficult task because our basic understanding of the properties of everyday, macroscopic objects is based on the emergent behavior of microscopic quantum states rather than the individual behavior of the states themselves. However, through experimentation, physicists have been able to discover many of the basic rules governing quantum states, many of which do not conform to conventional intuition.

For example, a measurement made on a quantum state will almost always change the properties of that quantum state¹. This disturbance need not be due to any imperfection of the measurement device (although such uncertainty does arise in practice), but rather due to fundamental limitations of how much information can be gained about a quantum state from measurements made on a single copy. This disturbance is the reason why the order in which measurements are made on a quantum state matters. For example, subsequent measurements made on the position and the momentum of a fundamental particle will yield different results depending on the order in which the two measurements are made. This difference in ordering leads to a measurement-disturbance relation [1, 2], which in turn dictates the fundamental limit on the amount of information that can be learned about the position/momenta state of a particle from a single copy². This limitation is not specific to just position and momentum, but rather provides intrinsic limitations to how much information can be inferred about *any* quantum state from a single particle. Measurement disturbance is at the heart of the motivation and limitations of quantum communication, a subfield of quantum information science that uses the information stored in quantum states as a resource for various communication techniques.

¹I say *almost* because it is possible to make a measurement on a quantum state without disturbing it if that quantum state is already known. For example, if a photon is known to be perfectly horizontally polarized, then it will pass through a horizontal polarizing film unchanged.

²The measurement-disturbance relationship referred to here should not be confused with the position/momenta uncertainty principle. The latter refers to how well the position and momentum of a particle are defined, while the former refers to how measuring one property (e.g., position) inevitably disturbs a conjugate property (e.g., momentum).

As an example, say a sender (Alice) wants to transmit information to a receiver (Bob) over a lossy/noisy communication channel. If Alice wishes to send a classical message to Bob, there are many classical strategies for establishing a reliable communication link between the two parties. For example, Alice can digitally encode her message in bits, and then use repeaters to amplify the signal to overcome loss, and use error correcting protocols to overcome noise [3]. However, if Alice wishes to send a *quantum* message to Bob, classical strategies fail. In this case, Alice cannot simply encode her message in bits, because quantum states are defined by continuous state parameters and would require an infinite amount of information to perfectly encode classically. Instead the message must be encoded on a quantum state. If Alice transmits a single copy of a quantum state, the measurement-disturbance relation prevents a repeater from making perfect copies of the state³ [4], so it cannot be amplified to overcome loss. Classical error correcting protocols also fail for similar reasons. Alternatively, Alice can send many copies of the same quantum state; however, such a strategy is not always possible if, for example, Alice does not know the state of the particle she is sending. Classical limitations such as this provide motivation for many of the quantum communication techniques described in the main body of the text, e.g., quantum teleportation (see Chapters III and IV) [5]).

1.2 Photonic Degrees of Freedom

In order for Alice and Bob to implement any quantum communication protocol, they need a physical system on which information can be encoded. In its most basic form, quantum information is encoded on two-level systems in the form of qubits (the quantum analogue of bits) (see Fig. 1.1). Qubits have been successfully encoded, manipulated, and measured using several physical systems, including ions [6], neutral atoms [7], superconductors [8], and nitrogen vacancy centers in diamonds [9]. For this work, I will focus on encoding information on photons.

Photons have several properties that make them ideal carriers of quantum communication: they are easily prepared and manipulated using commercial optical elements, and, by definition, travel at the speed of light, allowing them to be easily prepared and quickly transmitted between remote parties. Because of these properties, photons will likely be an integral part of any future, practical quantum communication protocol regardless of what type of physical qubit is used in other quantum information applications, such as quantum computing⁴.

To encode quantum information on a photon, it is necessary to first decide which photonic degree of free-

³If the state could be perfectly copied, Bob could violate the measurement-disturbance relation. This might be accomplished by making many identical copies of the state and then making measurements on each, allowing him to gain perfect knowledge of the quantum state that Alice sent without disturbing it.

⁴The primary limitation of photonic qubits is that they also do not interact strongly with each other making two-qubit gates (required in many quantum information protocols) probabilistic at best.

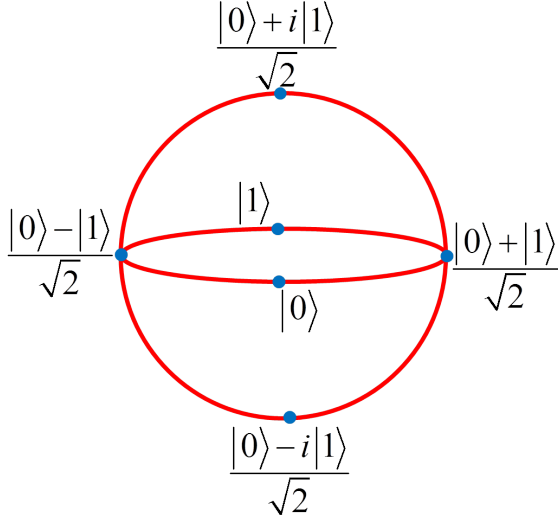


Figure 1.1: The space of possible qubit states can be geometrically represented by a sphere, known as the Bloch or (for polarization) alternately the Poincaré sphere. In this representation, orthogonal states are on opposite sides of the sphere and unitary transformations are represented by rotations of the sphere. Pure quantum states lie on the surface of the sphere; the interior describes “mixed states,” which are statistical mixtures of pure states and can be realized by ignoring a correlation to another system.

dom (polarization, time, or spatial distribution)⁵ to use for encoding information. Each of these properties has strengths and weaknesses when used to carry quantum information, as I will discuss below.

1.2.1 Polarization

Photon polarization is perhaps the most natural degree of freedom on which to encode quantum information, since it provides a natural two-level quantum state, e.g., using horizontal (H) and vertical (V) for basic state vectors (see Fig. 1.2a). This structure provides an advantage over the other continuous photonic degrees of freedom, since most quantum communication protocols use qubits rather than higher-dimensional states. In addition, polarization can be easily prepared, manipulated, and measured using simple waveplates or liquid crystals and polarizing beamsplitters, all elements which are relatively cheap, stable, and easy to align. Polarization can also be changed very quickly using the Pockels effect [11], allowing state modulation on the nanosecond time scale⁶. Furthermore, photonic polarization can be transmitted over long distances in free space without being disrupted by turbulence; fiber channels can also be used, though corrective elements are needed to avoid unintended polarization rotations.

⁵Quantum information can also be encoded on photon frequency and momentum; however, these properties are Fourier conjugates of time and spatial-mode, respectively, so I have not included them in their own section. Photon number/phase can be used to encode quantum information as well and are often used in continuous variable quantum information protocols [10] but are typically much more susceptible to loss, and in any event are beyond the scope of this work.

⁶This assumes bulk optics; waveguide modulators can achieve switching speeds below 100 ps, but are typically much more lossy.

While there are many aspects recommending the use of polarization for quantum communication, it has challenges and limitations as well. For example, while the two-level structure of polarization provides a natural qubit for basic quantum communication protocols, it is very difficult to extend to more advanced quantum communication protocols which require large quantum states⁷. Additionally, the polarization of light can change through polarization-dependent loss or rotation when reflected by mirrors or when propagating through some types of optical elements, such as optical fiber. However, these challenges included, polarization provides an appealing balance of stability and ease of manipulation.

1.2.2 Temporal Mode

Quantum states can also be encoded on the temporal distribution of photons. In contrast to polarization, the temporal distribution of a photon is a continuous degree of freedom having infinite possible state vectors⁸, thus allowing it to be used for advanced quantum protocols that require higher-dimensional states than qubits. It is also still possible to use a specific pair of temporal modes—“time-bins”—as a qubit, though more care is needed to ensure that information is not leaked into neighboring temporal modes.

Compared to polarization qubits, temporal qubits are much more difficult to prepare, manipulate, and measure. Typically, temporal qubits are prepared by transmitting a pulse through an unbalanced interferometer (see Fig. 1.2c)⁹. A single input pulse is split by the interferometer into two different pulses, which are used as the basic state vectors for the qubit. By manipulating the splitting ratio of the beamsplitter¹⁰ and controlling the phase-shift between the two pulse amplitudes, it is possible to prepare an arbitrary temporal-mode qubit. Manipulating the state of a temporal qubit is more challenging. Because the two pulses that define the qubit state are often separated by a few nanoseconds or less, deterministic state rotations require active, fast optics, such as Pockels cells or fiber modulators (see Section 2.3.3 for details). Because of the expense and experimental limitations of such fast optics, temporal modes are often manipulated probabilistically using conventional beamsplitters as passive switches. However, such rotations still require interferometers that are phase stabilized with respect to the preparation interferometers. This stabilization can be performed passively, by using very stable mounting and temperature-controlled environment; however, in practice, active stabilization is generally required for accurate qubit rotations. Measuring temporal qubits is similarly difficult as well, requiring many of the same elements that are required to manipulate

⁷It is possible to increase the dimension of polarization qubits by including more photons in the state; however, it is challenging to produce quantum states with a specific number of photons. Also, such states become increasingly sensitive to loss.

⁸There are, however, a constrained number of modes that can be transmitted in a particular time interval and bandwidth. This constraint is known as the Fourier transform limit and is a fundamental limitation constraining all communication protocols.

⁹It is also possible to form qubits from overlapping temporal modes; however, such modes require more experimental resources to use effectively [12].

¹⁰Variable transmission beamsplitters can be made using a Mach-Zehnder interferometer and a phase modulator [13].

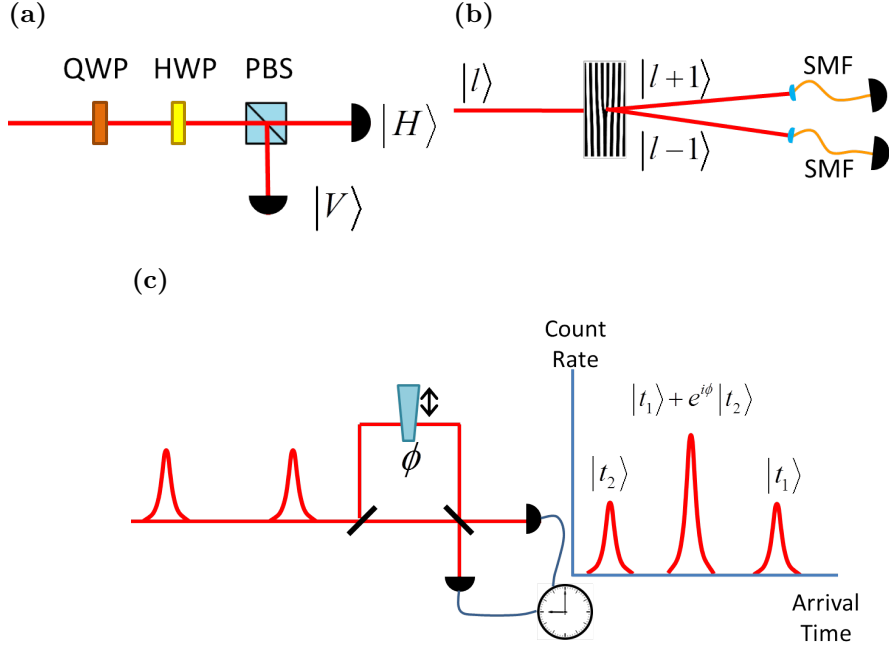


Figure 1.2: Measurement schemes for three types of photonic qubits. (a) Polarization qubits can be measured with half-waveplates (HWP), quarter-waveplates(QWP) and polarizing beamsplitters (PBS). (b) Temporal qubits are measured using unbalanced interferometers and fast clocks to measure arrival time. (c) Spatial qubits can be measured using holograms and single-mode fibers (SMF).

them, e.g., a phase-stabilized interferometer and a fast active switch to perform deterministic measurements.

See Chapter II for a more in-depth description of how to make precise temporal mode measurements.

While it is certainly more difficult to use temporal modes for quantum communication than polarization, temporal modes offer much better stability. In fact, the very same aspects which make these quantum states so difficult to manipulate also makes them robust to almost all experimental noise encountered in either the laboratory or even in a practical field environment. Only changes in the beam path on a time scale on the order of the pulse separation (usually a few nanoseconds or less) will disrupt the state. While such changes are uncommon in a laboratory setting, state changes *can* occur if temporal qubits are transmitted from a rapidly moving platform (e.g., satellites; see Section 4.4.1).

1.2.3 Spatial Mode

Similar to temporal mode, the spatial mode of a photon provides a continuous degree of freedom, allowing for complex quantum states. However, in contrast to temporal mode, the spatial distribution of a photon can be changed relatively easily using spatially varying optical elements, such as holograms or spatial light modulators. These two properties allow spatial mode to be used for high-dimensional quantum communica-

tion with relative ease. In fact, spatial-mode quantum states have been experimentally demonstrated with up to 300 different modes [14].

However, working with spatial modes also has its challenges. Just as the difficulty of manipulating temporal modes leads to their excellent stability properties, the ease of manipulating the spatial-mode of a photon gives rise to its fragility. Any non-spatially symmetric object in the beam path can change the spatial mode of the photon and lead to imperfections in the measured state. Such imperfection can easily arise in a laboratory setup due to, for example, optical aberrations or stress-induced birefringence, but are even more prevalent in long-distance quantum communication protocols. Beam pointing changes and aberrations induced by atmospheric turbulence greatly limit how cleanly high-order spatial modes can propagate through the atmosphere [15]. While there have been demonstrations of specially tailored high-order spatial modes propagating 3 km in free space [16], superpositions of these modes (which are required for most quantum communication protocols) are degraded by atmospheric turbulence. High-order spatial modes are similarly difficult to transmit though fiber. While *multimode* fibers can support propagation of high-order spatial modes, propagation through such fiber quickly scrambles input spatial modes in an unpredictable manner. However, new types of specially tailored optical fiber have recently been developed which support many different spatial modes without degradation [17]. These fibers preserve spatial modes by inducing a large spatial-mode dispersion in the fibers, preserving spatial modes in a manner similar to the way polarization-maintaining fiber preserves photon polarization. With proper dispersion compensation, these fibers may allow for faithful long-distance transmission of large spatial qubits, though first the loss needs to be reduced.

1.2.4 Hybrid Modes

Since the strengths and weaknesses of the photonic degrees of freedom described in the previous section are often complimentary, it is sometimes beneficial to combine these degrees of freedom into a hybrid quantum state. For example, ququart states (quantum states with four state vectors) of the form $\psi_A\phi_B \pm \psi_A^\perp\phi_B^\perp$ can be easily manipulated by operating on only one degree of freedom. This is particularly useful when performing measurements and rotations on states which are difficult to manipulate. In fact, the techniques described earlier for manipulating temporal-mode qubits operate by first transforming the two pulses into a spatial-temporal hybrid qubit, and then perform rotations on the resulting state.

Classical light beams with this hybrid form are also of experimental interest. Combinations of polarization and spatial mode, commonly called polarization vector beams, have been used for optimal focusing [18], high-speed communication protocols [19], and high-speed tracking of nanoparticles [20]. Similarly, beams composed of superpositions of temporal and frequency modes have been used for ultrafast photography [21].

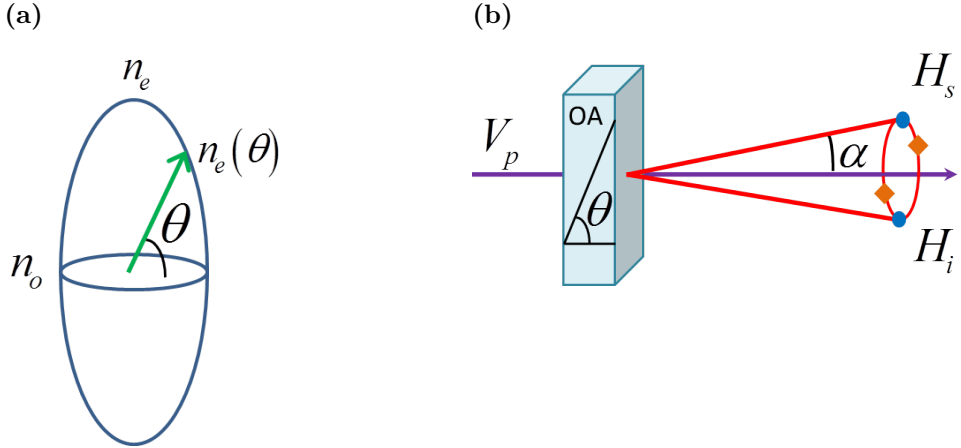


Figure 1.3: (a) The refractive index ellipse representing a uniaxial birefringent crystal where $n_e > n_o$. By tilting the polarization axis (green vector) with respect to the optic axis, the refractive index can be tuned. (b) Tuning θ in this fashion allows phase matching conditions to be satisfied at different cone angles (α). Downconversion photons exit the crystal on opposite sides of the cone of their partners, so a photon appearing at a blue circle (orange diamond) will herald its partner at the other blue circle (orange diamond).

The combined strengths of such hybrid modes often make them ideal choices for many advanced quantum communication protocols.

1.3 Entanglement

After suitable photonic degrees of freedom are selected, the next step in implementing most quantum communication protocols is the development of a source of entangled (nonlocally correlated) photon pairs. These states, typically of the form $\psi_A\phi_B \pm \psi_A^\perp\phi_B^\perp$, are known as maximally entangled and have the interesting property that *any* measurement on one qubit of the pair immediately reveals complete information about the quantum state of the other particle,¹¹ even if the two particles are spatially separated. While it might seem at first that these states could be used to transmit information instantaneously between two remote parties, such a communication scheme is not possible because any measurement made on individual particles yields completely random results. It is not until the measurement results of the pairs are compared that such a correlation is revealed. Despite this limitation, quantum entanglement is a key resource for many quantum communication protocols, such as superdense coding [22], quantum teleportation [5], remote state preparation [23], and many types of quantum key distribution [24].

Preparation of entangled states is often one of the principle challenges of quantum communication protocols. The preparation of such states generally requires two (or more) particles to interact with each other

¹¹Classically correlated states exist in which *some* measurements on one particle provide complete information about the state of the other, but quantum entanglement is needed for these correlations to exist in *every* basis.

via a nonlinear gate, such as a Controlled-NOT gate [25]. However, since it is very difficult to induce two photons to interact with each other, an alternate strategy is employed to create entangled pairs using spontaneous parametric downconversion (SPDC) [26]. SPDC is a process that occurs in certain types of nonlinear crystals in which a high-energy pump photon is split into two lower-energy photons (typically referred to as the signal and idler)¹². Since the SPCD process must conserve energy, momentum, and angular momentum, the signal and idler are only created in very specific modes which are related to the pump photon state. These conservation relations, collectively known as phase matching conditions, dictate that downconversion photons diverge from the SPDC crystal in a conical distribution (see Fig. 1.3a). However, to conserve momentum, photon pairs must be created on opposite sides of the cone, creating a continuous momentum-entangled photon state. By selecting two sets of momentum modes on opposite sides of the cone, it is possible to prepare a maximally entangled momentum qubit-state (see Fig 1.3b). Similarly, it is possible to use the phase matching conditions in SPDC as a tool to create entangled states in different photonic degrees of freedom. Below, I describe techniques for creating and measuring photon pairs that are entangled in polarization, temporal mode, or spatial mode; such photons are the central resource for the experiments described in Chapters II-V.

1.3.1 Polarization Entanglement

Twin-Crystal Source

To understand how SPDC is used to create polarization-entangled photons, a more thorough explanation of phase-matching conditions is required. These conditions can be explicitly observed from the formula describing the 2-photon state created during SPDC [28]:

$$\psi_{2\text{-photon}} \propto L^{(z)} \int d\mathbf{k}_p \phi_p(\mathbf{k}_p) \int d\mathbf{k}_s d\mathbf{k}_i \chi^{(2)} \delta(\omega_p - \omega_s - \omega_i) \prod_{m=x,y,z} \text{sinc} \left\{ \left[\kappa_p^{(m)} - \kappa_s^{(m)} - \kappa_i^{(m)} \right] L^{(m)} / 2 \right\} |\mathbf{k}_s, \mathbf{k}_i\rangle, \quad (1.1)$$

where \mathbf{k}_p , \mathbf{k}_s , and \mathbf{k}_i represent the wave-vectors of the pump, signal, and idler photons outside the crystal, κ_p , κ_s , and κ_i represent the wave-vectors of the pump, signal, and idler photons inside the crystal (where $\kappa_j = n(\omega_j)k_j$), $\omega_p (= |\mathbf{k}_p|c)$, ω_s , and ω_i represent the angular frequencies, $n^{(m)}(\omega_p)$, $n^{(m)}(\omega_s)$, and $n^{(m)}(\omega_i)$ are the refractive indices along the three axes of the crystal, $L^{(m)}$ is the length of the crystal along the three axes, $\phi_p(\mathbf{k}_p)$ represents the input momentum distribution of the pump, and $\chi^{(2)}$ is the nonlinear

¹²Entangled photon pairs can also be created through a different nonlinear process, known as four-wave mixing [27], which produces a pair of daughter photons from a pair of pump photons. Such a process can be convenient, since standard optical fibers can be used as the nonlinear medium; however, care must be taken to reduce noise due to spontaneous Raman scattering.

coefficient governing the strength of the SPDC interaction¹³. The delta function in this formula ensures that energy is conserved in the SPDC process, and the sinc function ensures that $\kappa_p^{(m)} = \kappa_s^{(m)} + \kappa_i^{(m)}$ to within approximately $1/L^{(m)}$. If the pump and downconversion photons are all the same polarization, dispersion in the SPDC crystal ($n(\omega_p) > n(\omega_{s,i})$) will cause the pump photon to have a larger momentum than the combined momenta of the signal and idler photons, violating momentum conservation. However, if the nonlinear crystal is birefringent, polarization can be used to allow momentum conservation by aligning the pump polarization with the axis with the smallest refractive index (fast axis) and aligning the polarization of at least one of the downconversion photons along the larger refractive index (slow axis). When momentum is conserved by both of the downconversion photons having the same polarization, this is known as type-I phase matching, while the case when the two downconversion photons have opposite polarization is known as type-II phase matching. By controlling the angle of the crystal optic axis with respect to the pump beam, it is possible to tune the extraordinary refractive index, and thus the momentum difference between the pump and the two downconversion photons, thereby controlling the cone angle of the downconversion (see Fig. 1.3). Details for calculating the downconversion cones and the necessary crystal optical axis orientation are available elsewhere [28].

Because downconversion photons are produced with well-defined polarizations with respect to each other, it is possible to design a source of polarization entangled photons. One example of such a source uses two orthogonally oriented nonlinear crystals with type-I phase matching [30] (see Fig 1.4a). For this source, the first (second) crystal is cut such that a horizontally (vertically) polarized pump photon is downconverted into two vertically (horizontally) polarized photons diverging at a cone opening angle that is set by the crystal-axis angle. If this cone opening angle is shallow (typically $\sim 3^\circ$) and the crystals are thin (typically ~ 0.2 to 0.6mm), then photons created in the two crystals will be indistinguishable except for their polarization. Consequently, by pumping the crystal pair with an equal superposition of horizontally and vertically polarized photons (e.g., diagonal polarization), the two downconversion photons are created in the following maximally entangled state:

$$|H_s H_i\rangle + e^{i\phi} |V_s V_i\rangle, \quad (1.2)$$

where subscripts s and i denote signal and idler photons respectively and the phase (ϕ) between horizontal and vertical components of the entangled state arises due to birefringence, dispersion, and geometric path length differences and can be compensated by tuning the phase difference between horizontal and vertical components of the pump beam with a waveplate¹⁴. A polarization entanglement source of this type is used

¹³A simplified description of the downconversion process is used in Equation 1.1, where we assume a nearly monochromatic, collimated pump. For a full description, see [29].

¹⁴If the phase between HH and VV terms is too large (due to, e.g., birefringent walk-off in the downconversion crystals),

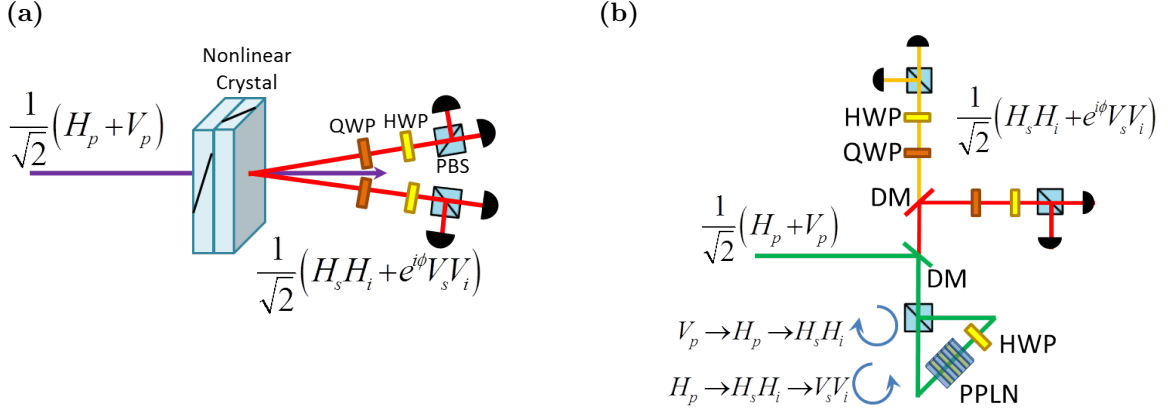


Figure 1.4: Two different polarization entanglement schemes. (a) The twin-crystal scheme allows for high-quality entangled states with very easy alignment and few optical components. (b) The Sagnac source can be used to create a very bright, narrow-band source by using long nonlinear crystals but requires more optical components than the twin-crystal source.

for experiments described in chapter II, III, and V; specific experimental details about each source are listed in the respective chapter.

Sagnac Source

It is possible to use the birefringence of a nonlinear crystal to satisfy phase-matching conditions over a wide range of wavelengths and downconversion cone opening angles; however, an alternate technique, known as quasi-phase matching, provides even greater flexibility by “poling” the SPDC crystal periodically over its length¹⁵ [31]. As mentioned previously, if momentum is not conserved for a particular downconversion process, a strong downconversion probability amplitude does not build as the photons propagate through the crystal. Instead, as shown by Equation 1.1, the conversion probability amplitude will only build up over a short crystal length before the integrand begins to oscillate and decay. However, if the crystal domain orientation is flipped every $\frac{1}{4}$ period of this oscillation, the nonlinear coefficient χ will change sign, allowing the downconversion probability amplitude to continually increase. The poling period can then be tailored to optimize, in principle, *any* downconversion process which conserves energy. In fact, this periodic-poling technique can be used to generate downconversion photons with the same polarization as the pump, known as type-0 phase matching, which is often used, since it usually has a significantly larger nonlinear coefficient (which determines the downconversion probability) than type-I and type-II phase matching.

Type-0 quasi-phase matching is often used in an interferometer-based polarization entanglement source

then the two terms will be distinguishable from each other leading to decoherence. This decoherence can be compensated by introducing a conjugate birefringent phase shift, thereby making the HH and VV terms indistinguishable again.

¹⁵Periodic poling is a technique in which a strong electric field is applied to periodically flip the domain orientation of a crystal, causing the nonlinear coefficients to change sign.

(see Fig. 1.4b). In this source the crystals are phase matched such that the downconversion cone angle is zero for the wavelengths of interest, so the downconversion photons exit the crystal in a beam that is collinear with the pump. The SPDC crystal is then placed in a polarizing Sagnac interferometer¹⁶ [32]. With the addition of a broadband half-waveplate, the crystal is pumped from both sides with horizontal polarization. Since both downconversion photons will be created in the same propagation direction as the pump, they will be in a superposition of traveling clockwise and counter-clockwise around the Sagnac loop. The counter-clockwise traveling photons will then be rotated from horizontal to vertical polarization. The two interferometer paths will then combine on the polarizing beamsplitter to form an entangled state. Like the twin-crystal source described above, there will again be a phase shift between the horizontal and vertical photon pair terms; however, the phase in this source arises from dispersion in the broadband waveplate. This phase can also be compensated by tuning the phase between horizontal and vertical components of the pump beam. Because both signal and idler photons created by this source will exit from the same polarizing beamsplitter face, this process is often phase matched so that signal and idler photons are different wavelengths. The photons can then be separated using a dichroic mirror. These Sagnac-based sources are useful when very long crystals are needed to produce bright, narrowband polarization entanglement [33]; such a source is used for the experiments described in Chapter IV.

After a polarization entangled state is created, it can be measured quite easily using waveplates and polarizers. By measuring photon polarization for both the signal and idler in a variety of different bases and correlating the results, a list of coincidence count rates (rates at which both signal and idler detectors fire at about the same time) can be compiled. These count rates can then be used to reconstruct the entangled state using one of several different tomographic inversion techniques. A comparison of the relative merits of several such techniques is provided in Appendix E.

1.3.2 Temporal-Mode Entanglement

Temporal-mode entanglement is relatively simple to produce and can be prepared in several different ways [12, 34, 35]. In one of the most common methods, a superposition of two discrete pulses (this can be created with an unbalanced interferometer as described in the previous section) is used to pump a SPDC crystal. The temporal profile of the downconversion photons will match the temporal profile of the pump, so the two downconversion photons will always be created in the same pulse, and the resulting two-photon state will be created in a maximally entangled temporal state, assuming the magnitudes of the two pump pulses are

¹⁶A type of interferometer in which the two paths are collinear but counter-propagating.

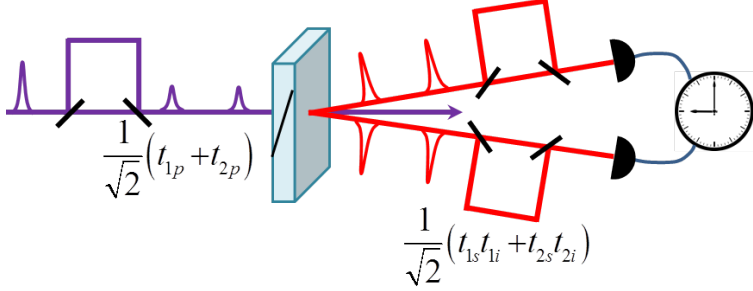


Figure 1.5: Temporal-mode entanglement can be created with few components, but precise tuning and excellent stability of the interferometers are needed for accurate state measurements. This entanglement setup can only be used to create maximally entangled states of a particular form. More components are needed to allow for general qubit “rotations” of temporal-mode entangled photons.

the same:

$$(|t_{1,p}\rangle + |t_{2,p}\rangle)/\sqrt{2} \longrightarrow (|t_{1,s}t_{1,i}\rangle + |t_{2,s}t_{2,i}\rangle)/\sqrt{2} \quad (1.3)$$

While such an entangled state is quite easy to produce, there are a few subtleties involved in accurately characterizing this type of temporal-mode entanglement. The temporal mode of the downconversion photons can be measured in the t_1/t_2 basis quite easily by simply measuring the arrival time of the photons to determine which time bin the photon was measured in; however, a time reference is needed to perform such a measurement. This may be accomplished using a photodiode to synchronize the timing electronics with the pump pulse used to create the downconversion (see Fig. 1.5). An unbalanced interferometer is needed to measure signal and idler photons in a superposition of the two time bins. Such a measurement can be made using a single interferometer (see Chapter II) or with two separate interferometers (see Chapter IV). If a single interferometer is used, then the path-length difference between the two arms of the pump and downconversion interferometers need only be matched to within the coherence length of the pump photons to obtain high visibility interference¹⁷. If two separate interferometers are used, then again the path-length difference of each interferometer must match that of the pump’s interferometer to within the coherence length of the pump; however, the path lengths of the downconversion interferometers must additionally match *each other* to within the coherence length of the *downconversion*. Often the downconversion coherence length is much smaller than the pump’s, so much more care is needed to ensure these two interferometers are adequately matched; for example the 10-nm filter bandwidth of our 710-nm photons (see Section 2.3.1) implies that the path length difference of the signal and idler interferometers must agree to within $\leq 16\mu\text{m}$. In addition to this “coarse” path length matching, the two downconversion interferometers need very fine

¹⁷For a pump wavelength λ and bandwidth $\delta\lambda$ (assuming a Lorentzian spectrum), the coherence length is given by $\frac{\lambda^2}{\pi\delta\lambda}$. If the path-length difference is larger than the coherence length, effectively a different temporal mode is being measured, and the interference visibility will be reduced, since the downconversion photons will not be correlated in this alternate measurement basis.

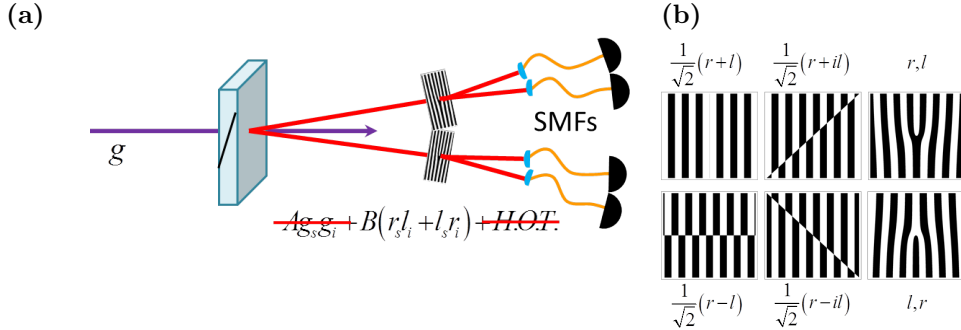


Figure 1.6: (a) Spatial-mode entanglement can be prepared with a simple setup, but (b) specialized holograms are needed to filter out unwanted modes and make projective measurements.

control as well in order to measure superposition states with a particular phase (e.g., $\frac{1}{\sqrt{2}}(|t_1\rangle + |t_2\rangle)$ versus $\frac{1}{2}(|t_1\rangle - |t_2\rangle)$). This phase difference must be held constant over the course of a measurement and often requires active stabilization of the interferometers using, e.g., an alignment laser providing feedback to a piezoelectric actuator on one of the mirrors. After coincidence measurements are made on signal and idler photons in the appropriate temporal bases, the quantum state can be reconstructed (see Appendix E).

1.3.3 Spatial-Mode Entanglement

Spatial-mode entanglement can be created using various techniques [36, 37]. One common method uses high-order spatial correlations in SPDC to create photons that are entangled in ± 1 -order orbital angular momentum states (r and l). In this technique, a Gaussian spatial mode (g) is used to pump the downconversion crystals, resulting in the following downconverted state:

$$|g_p\rangle \longrightarrow A|gsgi\rangle + B(|rsli\rangle + |lsri\rangle)/\sqrt{2} + \text{higher order terms.} \quad (1.4)$$

Because the relative amplitude of the Gaussian term is different from the amplitudes of the l/r terms and higher-order spatial modes, this state will be non-maximally entangled. However, spatial filters consisting of specially designed holograms and single-mode fibers can be used to remove all modes except the first-order orbital angular momentum states, resulting in the following maximally entangled state:

$$(|rsli\rangle + |lsri\rangle)/\sqrt{2} \quad (1.5)$$

This type of spatial-mode entangled source is used for experiments in Chapters III and V. Higher-order and/or more efficient entanglement can be created by tailoring the spatial mode of the pump beam [38], but

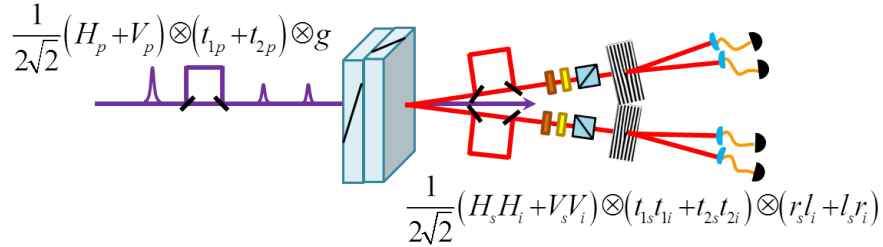


Figure 1.7: A source of photon pairs that are entangled in *every* degree of freedom. In the experiments described in this text, only two photonic degrees of freedom are simultaneously entangled.

as the dimension of the spatial mode increases, the states become more difficult to manipulate and measure.

The spatial-mode states of the downconversion photons may be characterized using various holograms in the spatial-mode filtering described above (see Fig. 1.6 and Appendix D for more details). These holograms make a projective measurement onto particular spatial modes by transforming the mode to be measured into a Gaussian beam and then filtering out all higher-order spatial modes with a single-mode fiber [39]. To obtain high-quality measurement results with this technique, it is important to have stable alignment of both the holograms and single-mode fibers with respect to the downconversion, since movement of either element will not only reduce the collection efficiency of the downconversion but can also decrease the visibility of the measurements by incorrectly filtering the spatial modes. This hologram-based measurement technique is also sensitive to changes in incident photon wavelength, since the holograms will impart different phase shifts on beams of different wavelengths. Also, since such measurement holograms often include a grating¹⁸ in addition to the measurement phase map, different wavelengths will diffract from the hologram at different angles, resulting in poor measurement efficiency and visibility. For this reason, a narrow-band downconversion source is required for optimal measurement results. Just as with polarization- and temporal-mode entangled photon states, measurements must be made on both signal and idler photons in several bases in order to obtain enough information to reconstruct the entangled state.

1.4 Hyperentanglement

Just as hybrid quantum states offer several advantages over quantum states of a single degree of freedom, states that are simultaneously entangled in multiple degrees of freedom—known as hyperentangled states—are often easier to produce, manipulate, and measure than quantum states of similar dimension encoded on a single degree of freedom (and therefore requiring multiple photon pairs). In fact, the entanglement sources listed in the previous section are able to be combined into a hyperentanglement source (see Fig. 1.7). Such

¹⁸Spatial-mode measurements can be made using holograms that do not have gratings. However, gratings can be used to perform measurements of multiple spatial modes simultaneously by placing spatial filters in multiple diffraction orders.

hyperentangled states have been used in various protocols to achieve tasks that are impossible with qubit entanglement, such as performing complete Bell-state measurements [40], creating quantum novel quantum states [41, 42], and measuring stronger nonlocal correlations than exist in qubit-entangled states [43].

In subsequent chapters, I will describe how we have combined the different entanglement sources described above to produce hyperentanglement and how we have used these states to increase the amount of classical information that can be transmitted with single photons (Chapter II), perform reliable state transmission between remote parties (Chapters III), demonstrate quantum communication techniques that might be performed from orbit (Chapter IV), and characterize quantum channels with fewer measurement settings than standard techniques (Chapter V).

Chapter 2

Hyperdense Coding

Portions reproduced in part with permission from T.M. Graham and P. G. Kwiat. Quantum Hyperdense Coding. *Proc. SPIE 9254*, Emerging Technologies in Security and Defence II; and Quantum-Physics-based Information Security III, 92540B (October 13, 2014).

2.1 Quantum-Enhanced Classical Communication

A natural goal of quantum communication is to develop methods of using quantum properties to increase the amount of *classical* information (i.e., the number of bits) that can be transmitted through a communication channel. Such a task is of theoretical interest since it reveals insights into how quantum and classical information are related. However, such methods could also be of practical use and might someday allow faster, more accurate classical communication. Since nearly all communication technology currently uses classical (rather than quantum) information, quantum-enhanced classical communication techniques could be integrated into current systems much more easily than developing technology which uses quantum inputs¹. While there have been several protocols which use the nonlocal behavior of entanglement to enhance classical communication [44, 45, 46], one of the oldest and best known is superdense coding [22].

2.1.1 Superdense Coding

Using classical state encoding, a sender (Alice) can communicate at most one bit of information for each qubit she sends to a receiver (Bob) [47]. For example, if Alice encodes her message using photon polarization, she could send a horizontally polarized photon to represent a “0” or a vertically polarized photon to represent a “1”. It is possible to increase the channel capacity (the number of bits Bob can decode per photon transmitted through the channel) using quantum entanglement. If Alice and Bob each possess one qubit of a Bell state², such as $|\Phi^+\rangle \equiv \frac{1}{\sqrt{2}}(|11\rangle + |00\rangle)$, then Alice may encode information on the total quantum state

¹While it is true that quantum-based communication/computing technology is, in principle, much more powerful than classical counterparts, such technology is still being developed.

²The actual distribution of the entangled state is experimentally challenging. Ideally, both parties could store entanglement until such a time as it was needed. Unfortunately, at present photons can only be stored for very short periods of time, and

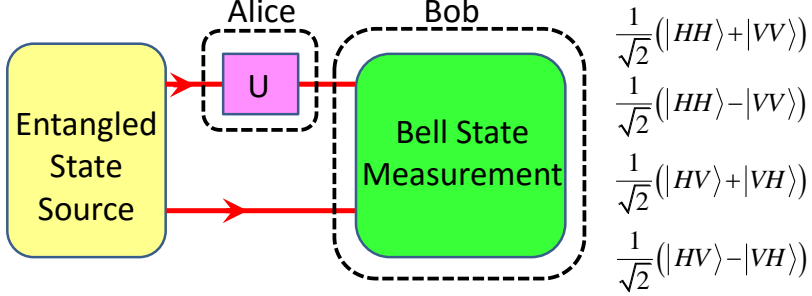


Figure 2.1: Basic layout for superdense coding. Alice and Bob each receive and store one photon from a maximally entangled pair. When Alice wants to send a message to Bob, she performs one of four unitary transformations on her photon to rotate the two-photon state to one of the four Bell states listed on the right. Alice then transmits her photon to Bob, who decodes her message by performing a Bell-state measurement on the two-photon state.

by performing unitary operations (Bloch sphere rotations) on her qubit. Because Alice’s rotations influence the joint state that she and Bob share, she can use one of four transformations (identity, bit flip, phase flip, and bit flip + phase flip), to rotate the input state to one of four³ mutually orthogonal Bell states:

$$|\Phi^\pm\rangle \equiv \frac{1}{\sqrt{2}} (|11\rangle \pm |00\rangle) \quad |\Psi^\pm\rangle \equiv \frac{1}{\sqrt{2}} (|01\rangle \pm |10\rangle). \quad (2.1)$$

Thus, assuming Bob can distinguish all four of these Bell states, Alice is effectively able to transmit four distinct messages (or two bits) to Bob by transmitting a single qubit, doubling the classical channel capacity limit. This type of message encoding is known as quantum dense coding or superdense coding [22]. Unfortunately, decoding all four of Alice’s messages is experimentally challenging. One decoding method uses a two-qubit gate known as a controlled-NOT (CNOT) gate; under the operation of this gate, a “target” qubit is flipped only when the “control” qubit is a “1”. This gate can be represented by the following unitary transformation:

$$U_{CNOT} = \begin{array}{c|cccc} & |00\rangle & |01\rangle & |10\rangle & |11\rangle \\ \hline |00\rangle & 1 & 0 & 0 & 0 \\ |01\rangle & 0 & 1 & 0 & 0 \\ |10\rangle & 0 & 0 & 0 & 1 \\ |11\rangle & 0 & 0 & 1 & 0 \end{array} \quad (2.2)$$

even matter-based quantum memories are relatively short-lived. Until storage times drastically increase, only proof-of-concept quantum dense coding is possible.

³If Alice and Bob share a *separable* state (e.g., $\lambda_A \lambda_B$), then local transformations on Alice’s photon can only access two orthogonal states, (e.g., $\lambda_A \lambda_B$ and $\lambda_{\bar{A}} \lambda_B$).

and maps the four Bell states to orthogonal separable states as follows:

$$\begin{aligned}\Phi^+ &\rightarrow \frac{1}{\sqrt{2}} (|0\rangle + |1\rangle) |0\rangle & \Phi^- &\rightarrow \frac{1}{\sqrt{2}} (|0\rangle - |1\rangle) |0\rangle \\ \Psi^+ &\rightarrow \frac{1}{\sqrt{2}} (|0\rangle + |1\rangle) |1\rangle & \Psi^- &\rightarrow \frac{1}{\sqrt{2}} (|0\rangle - |1\rangle) |1\rangle.\end{aligned}\tag{2.3}$$

The four separable states can then be distinguished using separable measurements (i.e., by measuring each photon individually). Since a CNOT gate requires the state of one qubit to change depending on the state of the other, this gate requires the pair of photons to undergo a two-body nonlinear interaction. However, nonlinear interactions between photons (currently the only practical flying⁴ qubit) are weak, making it impossible to perform a deterministic CNOT gate (or any other controlled gate) between the two photons. This, in turn, prevents deterministic Bell-state measurements using linear optics in a restricted Hilbert space (i.e., photons that are maximally entangled in only one qubit, such as polarization) [48, 49]. Despite this limitation, it is still possible to exceed classical channel capacity limits using linear optical Bell-state measurements.

2.1.2 Linear Optical Bell-State Measurements

Performing optimal Bell-state measurements with linear optics relies on Hong-Ou-Mandel (HOM) interference. In this two-photon interference effect, a photon is directed to each input of a 50-50 beamsplitter; output photon pairs are either bunched (always exiting the beamsplitter in the same output port) or anti-bunched (always exiting the beamsplitter in different output ports), depending on the parity of the two-photon spatial quantum state (see Fig. 2.2a). Since photons are bosons, the total two-photon wave function must be symmetric, in other words: $\Gamma(A, B) = \Gamma(B, A)$, where $\Gamma(A, B)$ represents the two-photon wavefunction of photons A and B . In general, it is possible to sort *separable* photon pairs incident on a HOM interferometer into two classes. If a pair of photons incident on a beamsplitter are identical and in a separable state $\phi_A \phi_B$, then the spatial wave function of the two-photon state is completely symmetric and they will exit the interferometer in the same port. On the other hand, if the photons are distinguishable from each other (e.g., if the photons do not overlap on the beamsplitter), then they will neither bunch nor anti-bunch at the output, since their spatial wave function will be neither symmetric nor antisymmetric.

Alternately, if the photons are in an entangled state, they can exhibit different behavior. Although photons are bosons, it is still possible for individual photonic degrees of freedom to be in an antisymmetric state, so long as the total two-photon state is symmetric. If, for example, a photon pair is in the Ψ^-

⁴A flying qubit is one that can be easily and quickly transmitted between remote parties.

polarization Bell state, then the polarization is in an antisymmetric state. To compensate, the spatial wave function of the two-photon state must also be antisymmetric, and the photons will anti-bunch when combined on a beamsplitter. On the other hand, all three of the other polarization Bell states are symmetric and will bunch. Thus, using a HOM measurement, Bob can distinguish Ψ^- from the other three Bell states based on symmetry. He can also then distinguish, e.g., Ψ^+ from the remaining two Bell states based on whether or not the two photons are measured in the same state (i.e., $|00\rangle$ or $|11\rangle$) or opposite states (i.e., $|01\rangle$ or $|10\rangle$). However, the final two states cannot be distinguished, so Bob can only reliably distinguish at most three of the four possible Bell states⁵ (and thus unitary transformations that Alice can make). This limitation lowers the achievable channel capacity of linear quantum dense coding from $\log_2 4 = 2$ to $\log_2 3$, or about 1.58 bits.

Further channel capacity limitations can arise when using many common types of single-photon detectors, such as avalanche photodiodes, since they cannot distinguish single- and multi-photon detection events. This will result in imperfect identification of Φ^+ , since both photons are always sorted into the same detector. To help identify two-photon events, multiple single-photon detectors and beamsplitters can be used to reduce the chance of both photons arriving at the same detector (see Fig. 2.2b). Alternately, true photon-number-resolving detectors, e.g., visible light photon counters [50] or transition-edge sensor detectors [51], can be used to distinguish single- and multi-photon events.

The first quantum dense coding experiment was performed by Mattel et al. using photons entangled in polarization [52]. By distinguishing three of the four possible polarization-Bell states, they transmitted messages with a higher channel capacity than is classically possible. Unfortunately, a lack of photon-number-resolving detectors limited their channel capacity to 75% of what is theoretically possible. This limitation as well as other experimental errors limited their channel capacity to 1.13 bits. Experiments have also been performed using probabilistic full Bell-state measurements (i.e., probabilistically distinguishing all 4 Bell states) on polarization-entangled photons [53, 54]; however, because the Bell-state measurements only work probabilistically, there is no theoretical increase in channel capacity by using this technique over three-state dense coding experiments. While it is not possible to deterministically distinguish all four Bell states using linear optics in a restricted Hilbert space, deterministic Bell measurements can be achieved using systems with physical qubits that can experience strong nonlinear interactions. An experimental implementation of full Bell-state measurement using nonlinear interactions has been achieved by Schaetz et al. using ions with entangled spin states [55]. However, poor state discrimination arising from technological limitations reduced their channel capacity from the theoretical limit of 2 bits to 1.16 bits, well below what is achievable even

⁵Although I have given here one specific setup, it can be proved more generally that at most 2 of the other 4 Bell states can be reliably distinguished using a single copy and only linear optical transformations [48, 49]. Obviously if there are many identical copies one can simply perform quantum state tomography to identify the state. Similarly, all four Bell states could be readily distinguished if one could deterministically implement a CNOT gate on single photons.

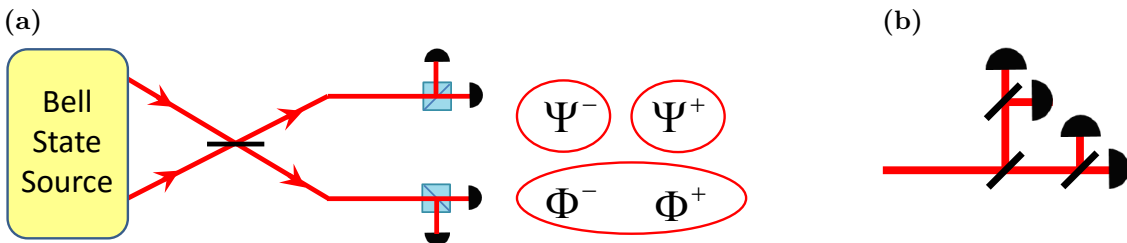


Figure 2.2: (a) An optimal linear optical polarization Bell state analyzer. Hong-Ou-Mandel interference is used to sort the four Bell states by parity of the polarization state. A polarization measurement in the horizontal and vertical basis is made on the output, sorting the four input polarization Bell states into three detection classes. (b) A tree of single-photon counters to measure multiple-photon inputs. Since most conventional single-photon counters can only measure one photon at a time, multiple detectors are needed to measure multi-photon states. A tree of four 100% efficient detectors, as shown, has a 75% chance of correctly identifying an input 2-photon state. The remaining 25% of the time, the two-photon state is misidentified as a single-photon input. This misidentification probability scales with n detectors as $\frac{1}{n}$.

using only linear optics. Additionally, it is unclear how this technique might be adapted for practical use, since an ion cannot be easily transmitted between remote parties.

2.2 Hyperentanglement-Enhanced Classical Communication

2.2.1 Hyperentanglement-Enabled Bell-State Measurement

As mentioned in the previous section, experimental optical dense coding implementations are severely limited by imperfect Bell-state measurements resulting from weak nonlinear interactions. One possible solution to this challenge is to couple the photons to a different quantum system, such as an ion [55], in which two-body interactions are not so weak. However, coupling between these quantum systems is very challenging to perform deterministically and requires extremely precise control of both physical systems. An alternate solution to increase the capacity of a quantum channel is to encode messages on multiple photonic degrees of freedom using hyperentangled states. Such states have several advantages over states entangled in only one degree of freedom and can be used to encode more information since they are elements of a larger Hilbert space⁶. Other methods for increasing Hilbert space size, such as encoding information on a single degree of freedom of multiple photon pairs, can be extremely difficult, often requiring many downconversion paths and very long counting times [56]. Finally, even though controlled quantum gates are impossible to deterministically implement between qubits contained on different photons using linear optics, it *is* possible to perform controlled quantum gates between qubits contained on the same photon using linear optics.

Such single-photon, two-qubit CNOT gates are crucial to designing techniques which use hyperentanglement-

⁶Larger Hilbert spaces have more orthogonal state vectors and can, therefore, be used to encode and distinguish more bits per photon.

enhanced superdense coding, and have been implemented them for photons that were simultaneously entangled in polarization and orbital angular momentum [57]. In this implementation, Alice encoded her message by manipulating the polarization of her photon (without modifying her photon's spatial mode) before sending it to Bob. Bob then used the fact that each hyperentangled Bell state which Alice prepares can be written as a unique superposition of single-photon Bell states [58]:

$$\begin{aligned}\Phi_{\text{spin}}^{\pm} \otimes \Psi_{\text{orbit}}^{+} &= \frac{1}{2}(H_1 H_2 \pm V_1 V_2) \otimes (r_1 l_2 + l_1 r_2) = \frac{1}{2} (\pm \phi_1^+ \otimes \phi_2^{\pm} \mp \phi_1^- \otimes \phi_2^{\mp} \pm \psi_1^+ \otimes \psi_2^{\pm} \mp \psi_1^- \otimes \psi_2^{\mp}) \\ \Psi_{\text{spin}}^{\pm} \otimes \Psi_{\text{orbit}}^{+} &= \frac{1}{2}(H_1 V_2 \pm V_1 H_2) \otimes (r_1 l_2 + l_1 r_2) = \frac{1}{2} (\phi_1^+ \otimes \psi_2^{\pm} + \phi_1^- \otimes \psi_2^{\mp} + \psi_1^+ \otimes \phi_2^{\pm} + \psi_1^- \otimes \phi_2^{\mp}),\end{aligned}\tag{2.4}$$

where $\phi^{\pm} \equiv \frac{1}{\sqrt{2}}(|Hl\rangle \pm |Vr\rangle)$, $\psi^{\pm} \equiv \frac{1}{\sqrt{2}}(|Hl\rangle \pm |Vr\rangle)$, and r and l represent +1 and -1 orbital angular momentum states, respectively. Because each term in this expansion is unique to one particular polarization Bell state (e.g., $\psi_1^+ \psi_2^-$ only appears in the $\Phi_{\text{spin}}^- \Psi_{\text{orbit}}^+$ expansion), it is possible to discriminate between all two-photon polarization Bell states by making single-photon Bell-state measurements on each photon of the pair. These single-photon Bell states can be measured deterministically without nonlinear interactions since the required CNOT gate is performed between two qubits on the same photon rather than between qubits encoded on two different photons (see Fig. 2.3). By detecting single-photon Bell states in coincidence, Alice is able to distinguish all four Bell states and fully decode the information Bob transmitted. Using such techniques, Barriero et al. achieved an effective channel capacity of 1.63 bits/photon, exceeding the $\log_2 3$ limit for superdense coding using linear optics and qubit-entangled states. A similar experiment was performed using photons that were hyperentangled in polarization and temporal mode and achieved a channel capacity of 1.18 bits/photon (less than the $\log_2 3$ limit for qubit superdense coding using linear optics) [59]. Nevertheless, these protocols do *not* actually exceed the classical coding limit. The photons used in these experiments contained information on multiple degrees of freedom—even though Alice manipulates only one qubit on her photon, she still must send two qubits to Bob instead of just one. In fact, it can be shown that there is a much easier, classical scheme to transmit two bits of information from Alice to Bob using single-photon two-qubit states; see Appendix A. However, it is still possible to beat the classical channel capacity limit if Alice manipulates *both* qubits encoded on her photon. Using this strategy, we implement hyperdense coding, a technique that can encode up to $\log_2 7 \approx 2.81$ bits per two-qubit photon transmitted from Alice to Bob.

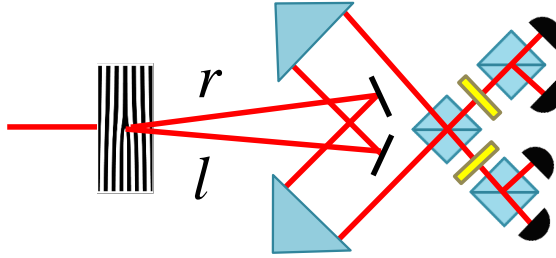


Figure 2.3: A controlled-NOT gate between the polarization and orbital angular momentum. The hologram converts input l and r orbital-angular-momentum states into Gaussian beams traveling to the left or right, respectively. A polarizing beamsplitter (PBS) is used to control the spatial mode, leaving it unchanged for horizontally polarized photons or flipping it if input photons are vertically polarized. By then measuring in the diagonal/anti-diagonal basis using half-waveplates (HWP) and PBSs, input single-photon Bell states (hybrid-entangled between polarization and orbital angular momentum) can be distinguished.

2.2.2 Hyperdense Coding

The reason previously implemented hyperentanglement-enabled dense coding schemes were limited to a maximum theoretical channel capacity of 2 bits/photon (equal to the 2-bit classical limit) is because Alice's message was encoded on only the polarization state of her photon (instead of both qubits of her photon), so she did not make full use of the two-qubit quantum channel required to transmit her photon to Bob. To surpass the 2-bit classical channel capacity limit (when two degrees of freedom are used), Alice's message must be encoded on *both* of her photon's entangled degrees of freedom, by rotating her state to one of the 16 orthogonal hyper-Bell states:

$$\Phi_{\alpha}^{\pm} \otimes \Phi_{\beta}^{\pm}, \quad \Phi_{\alpha}^{\pm} \otimes \Psi_{\beta}^{\pm}, \quad \Psi_{\alpha}^{\pm} \otimes \Phi_{\beta}^{\pm}, \quad \Psi_{\alpha}^{\pm} \otimes \Psi_{\beta}^{\pm} \quad (2.5)$$

where α and β denote qubits stored in both photonic degrees of freedom. However, just as in traditional dense coding protocols, not all of these states can be deterministically discriminated using linear optics, so Bob must use implement an optimal hyper-Bell state-measurement to discriminate as many as possible, as we now discuss.

Optimal Hyper-Bell State Analyzer

Hyper-Bell states are distinguished using many of the same techniques that are required to distinguish single-qubit-entangled Bell states. For example, hyper-Bell states can be sorted by parity using HOM interference. Since HOM interference will bunch or anti-bunch states based on the parity of the *total* two-photon quantum state, the output of the interferometer will depend on the parity of the Bell states encoded on both photonic

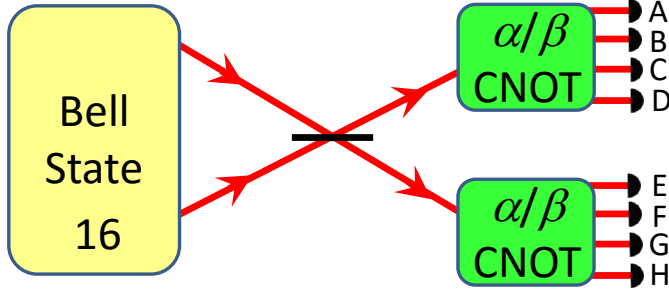


Figure 2.4: A linear two-qubit (α and β) hyper-Bell state analyzer. One of 16 possible hyper-Bell states is first sorted by parity using a Hong-Ou-Mandel interferometer. A controlled-NOT gate (CNOT) is then performed between α and β on both interferometer outputs, sorting input states into four outputs. By detecting all eight outputs in coincidence, input 2-qubit Bell states are sorted into seven distinct detection classes (see Table 2.2).

\otimes	Φ_{α}^{+}	Φ_{α}^{-}	Ψ_{α}^{+}	Ψ_{α}^{-}
Φ_{β}^{+}	+	+	+	-
Φ_{β}^{-}	+	+	+	-
Ψ_{β}^{+}	+	+	+	-
Ψ_{β}^{-}	-	-	-	+

Table 2.1: This table displays the parity of α/β hyperentangled states, depending on what Bell state each of the two degrees of freedom is in.

degrees of freedom (see Table 2.1). By measuring both outputs of the interferometer in the following basis:

$$|\phi^{\pm}\rangle \equiv |0\rangle_{\alpha} \otimes |0\rangle_{\beta} \pm |1\rangle_{\alpha} \otimes |1\rangle_{\beta} \quad |\psi^{\pm}\rangle \equiv |0\rangle_{\alpha} \otimes |1\rangle_{\beta} \pm |1\rangle_{\alpha} \otimes |0\rangle_{\beta} \quad (2.6)$$

the 16 hyper-Bell states can be sorted into seven distinct detection classes (see Table 2.2 and Fig. 2.4). Many other basis selections will also sort the hyper-Bell states into seven classes (e.g., even measuring in some bases which are separable in α and β will work). The optimal measurement configuration will depend greatly on the details of the experimental implementation, but it has been shown that seven is the largest number of two-qubit hyper-Bell state classes that can be reliably distinguished, for a maximum channel capacity of $\log_2 7 \approx 2.81$ bits/photon [60, 61]. More generally, it has been shown that n -qubit linear-optical Bell-state measurements can distinguish up to $(2^{n+1} - 1)$ classes of 2^{2n} possible hyper-Bell states [60, 61].

Like optimal single-qubit dense coding, hyperdense also coding requires photon-number-resolving detectors to distinguish all 7 classes of hyper-Bell states. Using traditional avalanche photodiodes, only 6 of 16 hyper-Bell state classes can be distinguished (since photons in detection class 1 always yield the same measurement outcome, see Table 2.2), limiting the channel capacity to $\log_2 6 \approx 2.58$. However, similar techniques as discussed earlier can be used to mitigate this limitation, e.g., using a beamsplitter-tree of detectors.

Class	States	Detector Signature
1	$\Phi_{\alpha}^{+} \otimes \Phi_{\beta}^{+}, \Phi_{\alpha}^{-} \otimes \Phi_{\beta}^{-}$	AA, BB, CC, DD
	$\Psi_{\alpha}^{+} \otimes \Psi_{\beta}^{+}, \Psi_{\alpha}^{-} \otimes \Psi_{\beta}^{-}$	EE, FF, GG, HH
2	$\Phi_{\alpha}^{+} \otimes \Phi_{\beta}^{-}, \Phi_{\alpha}^{-} \otimes \Phi_{\beta}^{+}$	AB, CD, EF, GH
	$\Phi_{\alpha}^{+} \otimes \Psi_{\beta}^{+}, \Psi_{\alpha}^{+} \otimes \Phi_{\beta}^{+}$	AC, BD, EG, FH
4	$\Phi_{\alpha}^{-} \otimes \Psi_{\beta}^{+}, \Psi_{\alpha}^{+} \otimes \Phi_{\beta}^{-}$	AD, BC, EH, FG
	$\Phi_{\alpha}^{+} \otimes \Psi_{\beta}^{-}, \Psi_{\alpha}^{-} \otimes \Phi_{\beta}^{+}$	AF, BE, CH, DG
6	$\Phi_{\alpha}^{-} \otimes \Psi_{\beta}^{-}, \Psi_{\alpha}^{-} \otimes \Phi_{\beta}^{-}$	AE, BF, CG, DH
	$\Psi_{\alpha}^{+} \otimes \Psi_{\beta}^{-}, \Psi_{\alpha}^{-} \otimes \Psi_{\beta}^{+}$	AH, BG, CF, DE
7		

Table 2.2: This table sorts the 16 possible hyper-Bell states into seven different classes, each with its own unique detection signature. The detector signature of each class is given when analyzed with the hyper-Bell state analyzer in Figure 2.4.

2.2.3 Turbulence-Resistant Hyperentanglement

To implement a useful hyperdense coding protocol, it is necessary to use hyperentangled states that can propagate over long distances without being disrupted. The orbital angular momentum of a photon is carried by its spatial mode, and as mentioned in the previous chapter, this can be disrupted by optical aberrations caused by propagation through atmospheric turbulence. While it is possible to compensate for such aberrations using adaptive optics [62], such techniques require expensive equipment such as wavefront sensors and adaptive optic mirrors. In addition, such devices are typically optimized for astronomical applications in which light has only passed through a few kilometers of thinning atmosphere. Aberrations introduced from traveling through many kilometers near ground level would be much larger in magnitude and oscillate on faster time scales [62], likely requiring custom adaptive optical elements to correct. A far less complicated solution for dense and hyperdense coding experiments is to choose a more robust degree of freedom. Using photons entangled in both polarization and arrival time avoids most of the problems introduced by atmospheric turbulence.

It might be speculated that using photons entangled in arrival time could reduce the bit rate of the information channel because the time each photon occupies is spread over a longer time interval than might be achieved by encoding information in a different degree of freedom. However, limitations in state-of-the-art technology already impose much stricter limits on the rate at which photons may be detected. For example, current single-photon counting modules require tens of nanoseconds to recover after detecting a photon. Because of these technological limitations, it is possible to use photons entangled in arrival time without reducing the amount of information sent in a given time interval.

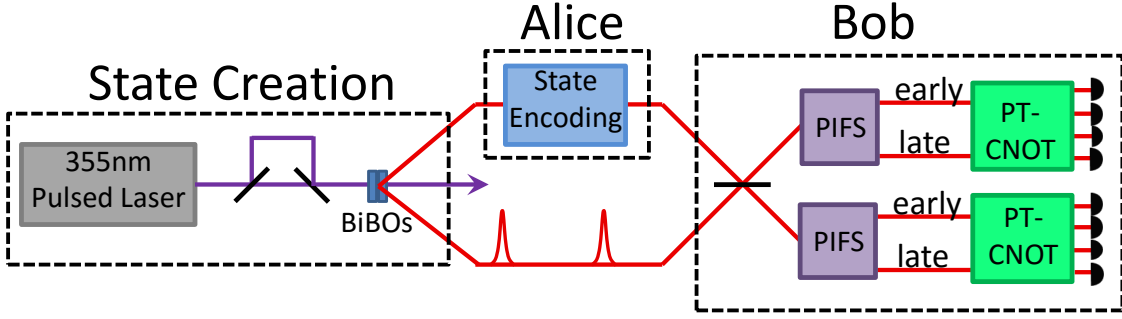


Figure 2.5: Experimental layout for performing hyperdense coding. A 2-qubit hyperentangled state is created by pumping two orthogonally oriented bismuth-borate (BiBO) crystals with a superposition of polarization- and temporal-modes; half of the state is sent to Alice and half to Bob. Alice encodes her message by performing polarization- and temporal-mode transformations and transmits her photon to Bob. Bob then performs a hyper-Bell-state measurement on the state, using Hong-Ou-Mandel interference, polarization-independent fast switches (PIFS) and polarization-temporal mode controlled-NOT gates (PT-CNOT). By identifying which of the seven hyper-Bell state classes the two-photon state is in, Bob can discover what transformation Alice made and decipher her message.

2.3 Experimental Implementation

While the theoretical ideas behind hyperdense coding are straightforward, there are several experimental challenges to implementing this technique using polarization- and temporal-mode hyperentangled photons. These challenges can be subdivided into the following three categories (see Fig. 2.5): hyperentangled state creation, Alice’s state encoding, and Bob’s hyper-Bell measurement. Our strategies for overcoming each of these three challenges are detailed below.

2.3.1 State Creation

To create the two-photon polarization- and temporal-mode entangled state required for this protocol, we combined the concepts of the twin-crystal polarization entanglement source and the two-mode temporal entanglement source discussed in Chapter 1 (see Sections 1.3.1 and 1.3.2, respectively). Specifically, 355-nm laser pulses (~ 13 ps in length, with a repetition rate of 80 MHz)⁷ were prepared in the following state:

$$\frac{1}{2} (|Ht_1\rangle + |Ht_2\rangle + |Vt_1\rangle + |Vt_2\rangle) \quad (2.7)$$

using waveplates and an unbalanced Mach-Zehnder interferometer. These pulses were then used to pump two orthogonally oriented type-I phase-matched BiBO crystals. With small probability, a 355-nm photon

⁷Laser pulses were created by a frequency tripled Nd:YVO₄ laser produced by Spectra Physics (Vanguard-355).

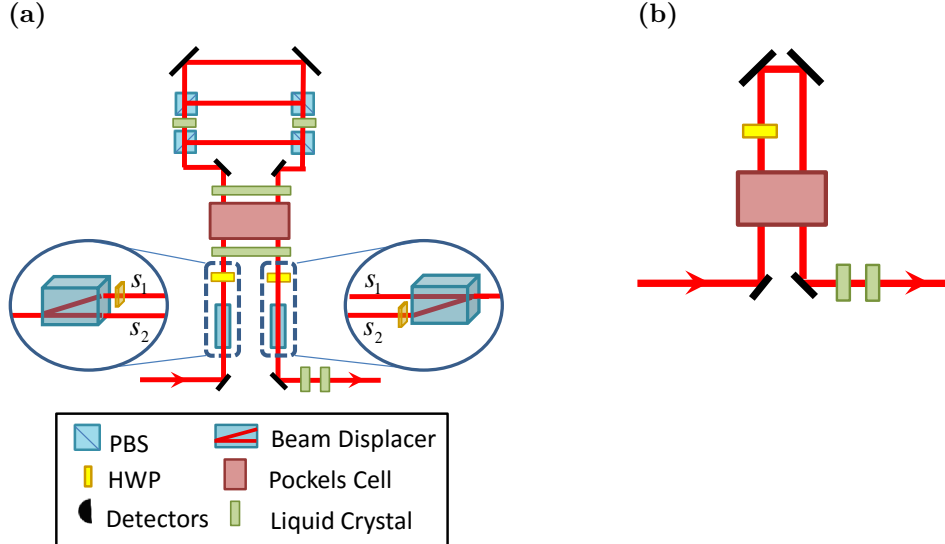


Figure 2.6: (a) Alice’s experimental layout to access all seven hyper-Bell state classes. Using Pockels Cells, half-waveplates (HWP), beam displacers, polarizing beamsplitters (PBS), and liquid crystals, Alice can deterministically control which interferometer path both of the two time bins take through the interferometer. This allows her to switch the time bin order or add a phase between them without affecting the polarization of the input photons. The liquid crystals after the interferometer output are sufficient to perform all four required polarization transformations. (b) If a 6-state hyperdense coding protocol is used (instead of a 7-state protocol), then Alice does not need to perform the time-bin switch required for accessing states in detection class 7 (see Table 2.2). This simplification greatly reduces the complexity of the experimental setup.

downconverts into two 710-nm photons creating the following hyperentangled state:

$$\frac{1}{2} (|HH\rangle + |VV\rangle) \otimes (|t_1 t_1\rangle + |t_2 t_2\rangle). \quad (2.8)$$

Once created, one photon of the pair is sent to Alice and the other to Bob.

Ideally, both Alice and Bob would store their photon pairs until they wished to send a message. The hyperentangled photons could then be used as an on-demand resource for high-speed communication. However, there are currently no ways to store photons indefinitely. In our proof of principal experiment, Alice encodes the state of her photon immediately and sends the photon to Bob, who receives both photons simultaneously.

2.3.2 Hyper-Bell-State Manipulation

To send a message to Bob, Alice must encode information on her half of the hyperentangled state. To do this, she must perform unitary operations on the polarization and temporal modes of her photon to transform the two-photon state that she and Bob share. However, as discussed in the previous section, Bob can only distinguish seven distinct classes of Bell states, so Alice must encode her message by rotating the

polarization and temporal mode of her photon, transforming the initial state to one in the seven target hyper-Bell classes. Polarization rotations can be accomplished easily using birefringent elements such as waveplates or liquid crystals. However, as discussed in the previous chapter, it is much more difficult to change the temporal state of a photon. Temporal transformations require active elements, such as Pockels cells, to operate deterministically.

When a voltage is applied to a Pockels cell, the ellipsoid parameterizing its indices of refraction is deformed, causing the crystal to become birefringent. The specific deformation of the index ellipsoid depends on the type of crystal and the direction that voltage is applied across the crystal (see Appendix C) [63]. When voltage is applied to the X-cut, two-crystal Rubidium Titanyl Phosphate (RTP) Pockels cells used in this experiment, the two eigen-polarizations experience equal and opposite phase shifts. By aligning a Pockels cell in the H/V basis and applying its half-wave voltage (the voltage required to induce a π -phase shift between the eigen-polarizations), the following polarization rotation can be performed:

$$\begin{array}{c|cc} & |H\rangle & |V\rangle \\ \hline |H\rangle & \left[\begin{array}{cc} e^{-\frac{\pi}{2}} & 0 \\ 0 & e^{\frac{\pi}{2}} \end{array} \right] \\ |V\rangle & \end{array}. \quad (2.9)$$

By quickly switching the Pockels cell voltage on or off as the two temporal modes of the photon travel through the Pockels cell, it is possible to induce a temporal-mode dependent polarization rotation.

Even using Pockels cells, the rotations required for hyperdense coding are challenging, since Alice must be able to manipulate the polarization and temporal modes of her photon independently. Switching the position of the two temporal modes of her photon (as is required for class 7) is particularly challenging since it must be accomplished without delaying the arrival time of Alice's photon with respect to the other hyper-Bell-state transformations. If the time-bin switch takes more time than Alice's other transformations, then it will be distinguishable from the other transformations, and Bob will not be able to decode the message with HOM interference. Because of this difficulty, Alice must transform her photon with nested interferometers composed of polarizing beamsplitters, beam displacers, birefringent elements, and a Pockels cell (see Fig. 2.6a). Alice uses a beam displacer and a half-waveplate to transfer the information stored on the polarization of her photon to the spatial modes s_1 and s_2 . She can then perform temporal mode rotations (without affecting the information stored on s_1 and s_2) by using the Pockels cell, liquid crystals, and polarizing beamsplitters to control which interferometer arm t_1 and t_2 are directed to. The path length differences in this compound interferometer must be kept stable with respect to the pump interferometer in order to keep states in classes 2 and 7 from transforming into states from class 1 (and vice versa). Alice

then transfers the information stored on s_1 and s_2 back onto the polarization of her photon, again using a half-waveplate and a beam displacer. She can then perform the polarization transformations required for the hyperdense coding protocol using liquid crystals (without affecting the information stored on t_1 and t_2).

The complicated transformations described above are needed to access all 7 possible classes of states that can be distinguished with an optimal hyper-Bell state analyzer. However, it is possible for Alice to encode slightly less information on the two-photon state using a much simpler setup that does not require any interferometers (see Fig. 2.6b). This setup cannot be used to switch time bins as required for Alice to produce states in class 7 (see Table 2.2), but can perform the transformations required to access the other 6 hyper-Bell classes for a total channel capacity of $\log_2 6 \approx 2.58$ bits/photon. Depending on imperfections and system stability of the experimental implementation, this simpler encoding scheme might actually achieve a higher channel capacity than the more complicated 7-state protocol.

2.3.3 Hyper-Bell-State Measurement

After encoding her message, Alice transmits her photon to Bob, who then has the task of decoding the message using hyper-Bell-state measurement. Regardless of whether Alice uses 6- or 7-state encoding, Bob can use the same hyper-Bell state analyzer to decode her measurement. As mentioned above, the first step in decoding Alice's measurement is to use HOM interference to sort received hyper-Bell states by parity. This can be accomplished by combining Alice's and Bob's photons on a beamsplitter. It is important for both photons to arrive at the beamsplitter within the coherence time⁸ of downconversion ($\tau \approx 150\text{fs}$, corresponding to a path-length difference of $50\mu\text{m}$), or the photons will appear distinguishable from each other and will neither bunch nor anti-bunch.

Bob must then measure the outputs of the HOM interferometer in the single-photon 2-qubit Bell state basis listed in Equation 2.6, where α and β represent the polarization and temporal photonic degrees of freedom, respectively. However, this measurement requires the two time bins to be sorted into two different spatial modes using a polarization-independent fast switch. This switch can be performed probabilistically using a single beamsplitter, but will result in a 75% message loss⁹, significantly lowering the channel capacity. To implement a deterministic polarization-independent fast switch, we use a combination of passive optical elements in combination with a Pockels cell (see Fig. 2.7a). In this switch, a beam displacer and a waveplate are used to transfer the information stored on an input photon's polarization state to the spatial modes s_1

⁸The downconversion coherence time is set by the bandwidth (10 nm) of filters in the downconversion arms.

⁹A beamsplitter used as a passive switch will only correctly sort photons in the t_1 (t_2) time bin into the long (short) interferometer arms 50% of the time. Time bins that are sorted into the incorrect interferometer arm will not arrive at the detectors at the correct time and will be discarded in post-processing. Bob operates on two photons, so if he uses passive switches, both photons will only be sorted correctly $(50\%)^2 = 25\%$ of the time.

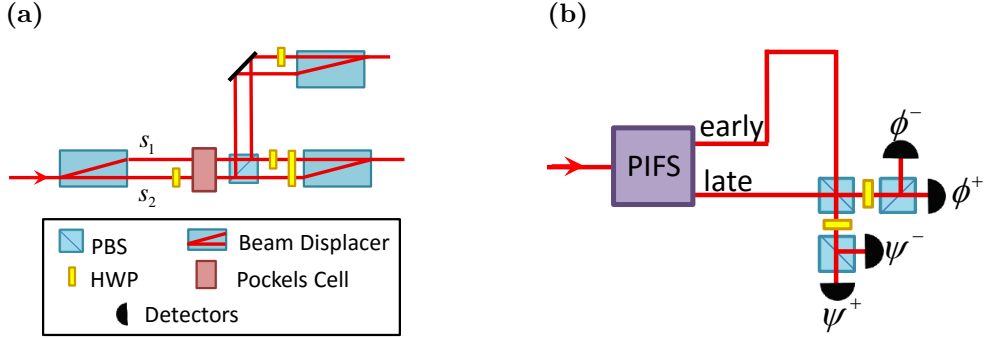


Figure 2.7: (a) An example of a deterministic, polarization-independent fast switch. The polarization state of the photon is changed to a spatial-mode qubit in s_1 and s_2 using a beam displacer and half-waveplate (HWP). A Pockels cell then flips the polarization between the two time bins, reflecting the first time bin with a polarizing beamsplitter (PBS) and transmitting the second. The qubit encoded on s_1 and s_2 is then transformed back into a polarization qubit with beam displacers and HWPs. (b) A controlled-NOT gate between the polarization and time qubits. A polarization-independent fast switch (PIFS) (as shown in a) separates the two temporal modes into two paths without affecting polarization. These two paths are then combined on a polarizing beamsplitter, which switches the beam path for vertically polarized inputs or leaves them unchanged for horizontally polarized inputs.

and s_2 . The two temporal modes can then be sorted into different output paths by performing a polarization rotation on one of the temporal modes using the Pockels cell, and then separating the two time bins using a polarizing beamsplitter. The information stored on s_1 and s_2 can then be transferred back to the polarization state using waveplates and beam displacers.

After the temporal modes of the photons are separated, Bob implements a CNOT gate between the polarization and temporal mode degrees of freedom (see Fig. 2.7b) by inputting two spatial modes (output from the time switch) into an unbalanced Mach-Zehnder interferometer with the same path-length difference as the pump interferometer. Finally, Bob projects the interferometer outputs into the D/A polarization basis and counts the number of photons in each of the resulting modes using single-mode-fiber-coupled avalanche photodiodes. Each of the states that Alice sends will have a different detector signature when measured with this set of interferometers (see Table 2.2).

Both photons of hyper-Bell states in detection class 1 will always appear at the same single-photon counter, so only six of these seven state classes can be distinguished when using a single avalanche photodiode at each output. To mitigate this problem, we can use multiple avalanche photodiodes at each output to allow probabilistic detection of states in hyper-Bell class 1. The probability of detection of class 1 states will depend on how many detectors are used at each output. In this implementation, four avalanche photodiodes are used at each output (sequentially¹⁰) to identify states in detection class 1 (as in Fig. 2.2b). The efficiency

¹⁰Because detector number is limited, only four detectors are used in one output port at a time for our proof-of-principle experiment.

of detecting these states is thereby reduced, since both photons still arrive at the same detector 25% of the time, reducing the maximum channel capacity to 2.71 bits/photon.

2.3.4 Experimental Results

The capacity of Alice and Bob’s communication channel depends greatly on how efficiently and reliably each step of the experimental procedure is implemented. We used quantum state tomography to characterize the quantum state created by the downconversion source described above. A full reconstruction of the polarization state yielded 99.5% fidelity¹¹ with the target state, and a partial reconstruction of the temporal-mode state yielded a 95% fidelity (more complete measurements are currently underway). The fidelity of the polarization state is currently limited by dephasing in the downconversion crystals, which causes photons created in the two downconversion crystals to be partially distinguishable; however, the small error present in the polarization state will only cause a 0.02 bit/photon decrease in channel capacity. The more sizable error in the temporal-mode fidelity is caused by imperfect matching of the downconversion interferometer path-lengths, causing dephasing between the $t_1 t_1$ and $t_2 t_2$ terms of the downconversion. We are currently working to reduce dephasing by more carefully balancing the downconversion interferometers; however, it is currently the limiting source of experimental error and reduces the channel capacity by 0.17 bits/photon.

Another source of experimental error that can limit the channel capacity of this protocol arises in the HOM interference of Bob’s measurement. If the photons appear distinguishable (e.g., due to the photons arriving at the beamsplitter at different times), the visibility of the HOM interference is reduced, and the symmetric and anti-symmetric hyper-Bell states cannot be perfectly distinguished from each other. By scanning the path length of Alice’s photon with respect to Bob’s, the visibility of Bob’s HOM interferometer was measured to be 99.3%, reducing the channel capacity by 0.025 bits/photon. The small residual error in the HOM interference is hypothesized to arise from imperfect spatial mode-overlap of spatial modes of the two photons on the beamsplitter. This will in turn result in uneven coupling into of the two HOM interferometer paths into the fiber coupled detectors, thereby reducing the visibility. Figure 2.8 illustrates how small amounts of polarization dephasing, temporal dephasing, and imperfect HOM interference reduce the capacity of the communication channel.

An estimate of the system channel capacity can be determined using the following formula [57]:

$$H(X : Y) = \sum_{y \in Y} \sum_{x \in X} p(x)p(y|x) \log_2 \frac{p(y|x)}{\sum_{x \in X} p(y|x)p(x)}, \quad (2.10)$$

¹¹The fidelity is a distance measure of how close the measured state is to the target and is defined as $F(\rho_m, \rho_t) \equiv \text{Tr}[\sqrt{\sqrt{\rho_t}\rho_m\sqrt{\rho_t}}]^2$, where ρ_m and ρ_t are the density matrices representing measured and target quantum states.

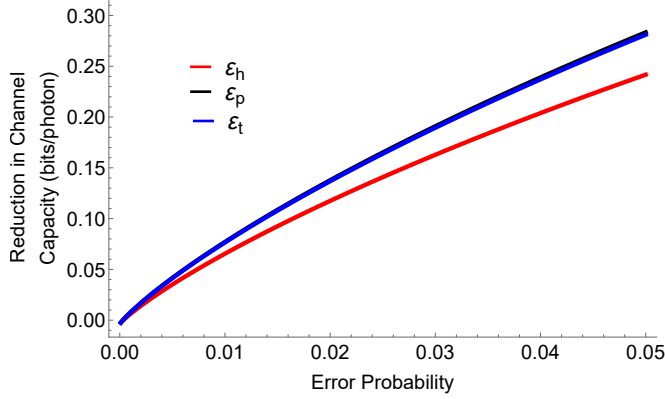


Figure 2.8: A plot illustrating how small amounts of polarization dephasing (ϵ_p), temporal dephasing (ϵ_t), and Hong-Ou-Mandel (HOM) interference error (ϵ_h) reduce the capacity of hyperdense coding. Small imperfections in the HOM interference result in a smaller change in the channel capacity than similar amounts of polarization and temporal dephasing, because it results in less ambiguity in the detection classes (see Table 2.2). As these errors become more likely ($\sim 10\%$), the channel capacity calculation can no longer be linearized accurately, and the influence of the different errors on the channel capacity can no longer be decoupled.

where X and Y represent the space of signals transmitted and received respectively, $p(x)$ and $p(y)$ represent the probabilities that a given signal is transmitted or received, respectively, and $p(y|x)$ represents the conditional probability that message y was received given x was transmitted. Incorporating all currently measured error sources, an estimated channel capacity of 2.49 bits/photon is possible with this setup¹². However, to obtain accurate channel capacity estimates, complete characterizations of Alice’s rotations and Bob’s polarization/temporal-mode CNOT gate are required. These measurements as well as the full demonstration of the hyperdense coding protocol are currently underway.

2.4 Outlook

In conclusion, we have described an experimental setup which uses hyperentanglement to maximize the amount of classical information that can be transmitted over a two-qubit channel using linear optics. Furthermore, because the two photonic degrees of freedom that we use to transmit messages are resistant to the influences of atmospheric turbulence, this technique might be used to communicate classical information over a long-distance free-space channel.

As a final note, the techniques described in the previous section may be extended to even higher-dimensional encoding schemes using photons that are hyperentangled in more than two degrees of freedom. The utility of these higher-dimensional versions of superdense coding can be examined by comparing them

¹²This channel capacity assumes that a tree of four detectors are used to measure states in detection class 1. If true photon-number-resolving detectors are used, the channel capacity might be increased to 2.59 bits/photon.

	Capacity of classical encoding (bits/photon)	Linear hyperdense coding (bits/photon)	Nonlinear hyperdense coding (bits/photon)
$n = 1$	1	1.58	2
2	2	2.81	4
3	3	3.91	6
10	10	10.99	20
n	n	$\log_2 2^{n+1} - 1$	$2n$

Table 2.3: A comparison of channel capacity achievable using various encoding and decoding techniques for different numbers of qubits (n). Asymptotically in n , linear hyperdense coding can only transmit one additional bit/photon more than classical encoding techniques, whereas nonlinear hyperdense coding can transmit twice the number of bits/photon.

with classical encoding techniques of the same dimensionality. Specifically, an n -qubit quantum state can be used to transmit $\log_2 n^2 = n$ -bits using classical coding techniques (i.e., techniques which do not require entanglement). An n -qubit state, however, can be used to send at most $\log_2(2^{n+1} - 1)$ bits per photon [60, 61]. This implies that, as n becomes large, hyperdense coding (and linear optics) can be used to send at most one additional bit of information as compared to classical encoding (see Table 2.3). Additionally, the complexity of hyperdense coding greatly increases with increasing dimensionality, quickly making high-dimensional implementations prohibitively challenging. This, coupled with technological limitations of high-speed single-photon detection, makes it unlikely that linear optical hyperdense coding will be used practically to increase the capacity of communication channels. However, if nonlinear techniques allow for complete hyper-Bell-state measurements, the factor of 2 increase in channel capacity could have practical significance.

Alternately, linear hyperdense coding may potentially be useful as a quantum cryptography technique. Assuming Alice and Bob's photons are initially securely created and distributed (e.g., via teleportation), then it is impossible for an eavesdropper (Eve) to gain access to any part of Alice's state rotation. This is because Alice and Bob's photons are in a maximally entangled state, so any measurement that Eve can make on Alice's photon alone will have a completely random output. Eve needs access to both photons to learn anything about Alice's message. Similarly, Eve cannot sabotage Alice's message without detection because hyperdense coding requires two-photon interference, and any state modification that Eve can make would distort the messages of Alice and Bob's communication, allowing Eve to be detected. Unlike other quantum cryptography techniques, such as BB84 [24], this scheme has the benefit of not requiring any security checks or randomness amplification, in addition to having an increased channel capacity. If Eve has access to both photons before state distribution and Alice's photon after the message is encoded, then Alice and Bob do need to perform routine security checks to ensure that their photons are still maximally entangled (such as a Bell test), but the technique still retains the enhanced channel capacity. However, further investigation of

the security of hyperdense coding is required to assess its usefulness for quantum cryptography.

Chapter 3

Spatial Superdense Teleportation

Reproduced in part with permission from T.M. Graham, H.J. Bernstein, T.-C. Wei, M. Junge, and P.G. Kwiat. Superdense Teleportation using Hyperentangled Photons. *Nature Communications*, 6 (2015).

3.1 Introduction

3.1.1 Quantum Teleportation and Remote State Preparation

The transfer of quantum information over long distances has long been a goal of quantum information science. Loss is particularly devastating to quantum communication channels as quantum states cannot be amplified [4]. Moreover, random fluctuations in the communication channel can reduce the coherence of a quantum state, and error correction protocols for quantum states are presently very difficult to implement in practice [64]. However, if the sender (Alice) and the receiver (Bob) already share an entangled pair of qubits, then they may use a number of techniques to transfer quantum states using only classical information channels. In single-qubit quantum teleportation (QT, Fig. 3.1a) [5], Alice performs a measurement in the Bell state basis on the unknown state provided by a state chooser (Charles) and her half of the entangled state that she shares with Bob. The state of all three photons can be written in terms of Alice's measurement:

$$\begin{aligned} |\chi\rangle_C|\Phi^+\rangle_{A,B} &= (\cos\theta|0\rangle + e^{i\phi}\sin\theta|1\rangle)_C(|0\rangle_A|0\rangle_B + |1\rangle_A|1\rangle_B) \\ &= |\Phi^+\rangle_{A,C}(\cos\theta|0\rangle + e^{i\phi}\sin\theta|1\rangle)_B + |\Phi^-\rangle_{A,C}(\cos\theta|0\rangle - e^{i\phi}\sin\theta|1\rangle)_B \quad (3.1) \\ &\quad + |\Psi^+\rangle_{A,C}(\cos\theta|1\rangle + e^{i\phi}\sin\theta|0\rangle)_B + |\Psi^-\rangle_{A,C}(\cos\theta|1\rangle - e^{i\phi}\sin\theta|0\rangle)_B, \end{aligned}$$

where $|\chi\rangle$, is the state of the photon that Alice is trying to transmit to Bob, is parameterized by angles θ and ϕ . States Φ^+ , Φ^- , Ψ^+ , and Ψ^- represent four maximally entangled Bell states as defined by Equation 2.1. Alice then sends the two-bit outcome of her measurement to Bob over a classical communication channel. By inspection of Equation 3.1, it can be observed that the state of Bob's photon will be related to $|\chi\rangle$, but the exact relation between the two states will depend on Alice's measurement. Hence, based on the outcome

of Alice's measurement, Bob performs one of four unitary transformations on his photon, transforming it into the exact state that Charles chose.

Qubit teleportation has been successfully demonstrated with probabilistic protocols for photons¹ [65, 66, 67] and with deterministic protocols using nonlinear interactions for ions [68, 69], superconducting qubits [70], nitrogen vacancy centers in diamond [71], and hybrid systems between photons and ions [72]. More recently, QT has also been performed using photons entangled in spatial mode, where Charles' quantum state is encoded on the polarization degree of freedom of Alice's photon [73]. Since Bell measurements between photonic degrees of freedom do not require nonlinear interactions, this protocol could theoretically be implemented with 100% efficiency; however, since both Alice's and Charles' qubits are encoded on the same photon, this procedure is more accurately classified as deterministic remote state preparation (described below).

In teleportation, Charles provides a quantum state that he wishes to be sent to Bob. However, the state parameters Charles wishes to send can instead be encoded directly on Alice's half of the entangled state by making the rotation

$$U_C = \begin{matrix} & |0\rangle & |1\rangle \\ \begin{array}{c} |0\rangle \\ |1\rangle \end{array} & \left[\begin{array}{cc} \cos\theta & e^{i\phi}\sin\theta \\ -e^{-i\phi}\sin\theta & \cos\theta \end{array} \right] \end{matrix}, \quad (3.2)$$

thus transforming Alice and Bob's total state into the following:

$$|\Phi^+\rangle_{A,B} \xrightarrow{U_C} (\cos\theta|0\rangle - e^{-i\phi}\sin\theta|1\rangle)_A|0\rangle_B + (\cos\theta|1\rangle + e^{i\phi}\sin\theta|0\rangle)_A|1\rangle_B. \quad (3.3)$$

Alice can then transmit the unknown qubit state to Bob with a much simpler procedure. In this technique, known as remote state preparation (RSP, Fig. 3.1b), Alice need only perform measurements on her single qubit in the 0/1 basis and transmit the outcome to Bob [74]. Again rewriting the total quantum state in terms of Alice's measurement:

$$|0\rangle_A(\cos\theta|0\rangle + e^{i\phi}\sin\theta|1\rangle)_B + |1\rangle_A(\cos\theta|1\rangle - e^{-i\phi}\sin\theta|0\rangle)_B = |0\rangle_A|\chi\rangle_B + |1\rangle_A|\chi^\perp\rangle_B, \quad (3.4)$$

where again $|\chi\rangle$ represents the target state to be sent to Bob and $|\chi^\perp\rangle$ is the state orthogonal to $|\chi\rangle$. Then, as in teleportation, Bob's state will be related to $|\chi\rangle$ in some way that depends on the outcome of Alice's measurement. Bob can then attempt to perform a corrective transformation on his qubit, based on the

¹Deterministic quantum teleportation has been implemented using continuous variable entanglement [10]; however, such measurements are inevitably noisy due to finite squeezing, greatly lowering the teleported state fidelity.

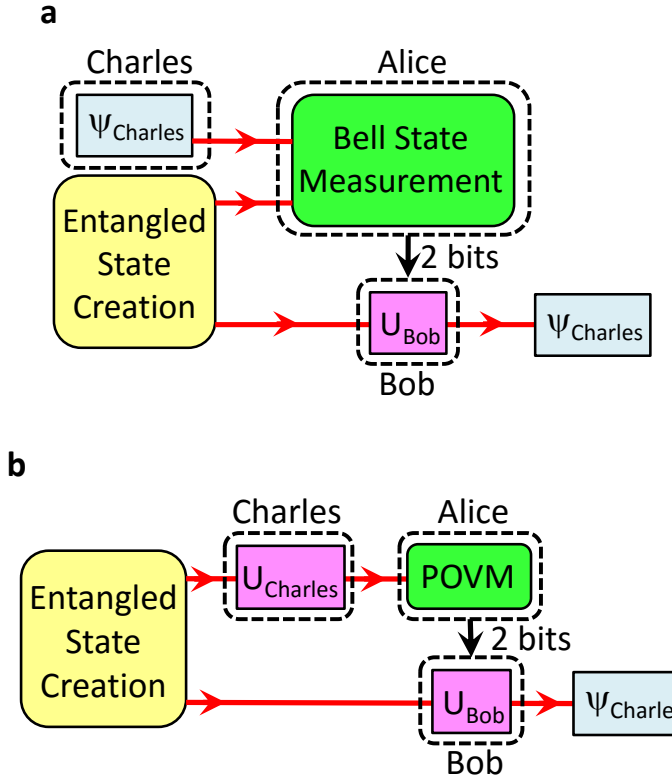


Figure 3.1: Schemes to transfer one qubit. **(a)** Quantum teleportation layout. Charles prepares a state for Alice, who performs a Bell measurement between her state and Charles'. She then transmits the results of the measurement to Bob, who is able to transform his photon into the state Charles had chosen. **(b)** Remote state preparation (RSP) layout. Charles performs a unitary transformation on one photon and sends it to Alice, who uses a positive-operator valued measure (POVM) on her photon. She then sends the outcome to Bob, who transforms his state into the state Charles chose.

message he received. It might be speculated, since Alice’s measurement has only two possible outcomes, that she would only have to send a single-bit message to Bob. However, because Bob cannot perform a universal NOT gate (a mapping of the input state to its orthogonal)² [74], he cannot in general transform $|\chi^-\rangle$ to $|\chi\rangle$, so a one-bit message from Alice is not sufficient for him to correct his state. In fact, because of the impossibility of a universal NOT gate for general qubits, all RSP implementations using simple projective measurements as described above are inherently probabilistic [75, 76]; moreover, as the dimension of the remotely prepared state increases, the probability of success becomes smaller (see Figure 3.2).

A more complicated scheme is needed to remotely prepare quantum states deterministically and requires Charles and Alice to jointly perform a type of generalized measurement known as a “positive-operator valued measure” (POVM)³ [77]. One way of implementing such a scheme is for Charles to encode his state

²Every unitary transformation or series of unitary rotations has an axis (or eigenbasis) which is unaffected by the transformation and hence not mapped to its orthogonal. A universal NOT gate requires anti-unitary transformations, which are unphysical.

³Unlike a set of orthogonal projective measurements, POVMs need not be orthogonal and can have more elements (or

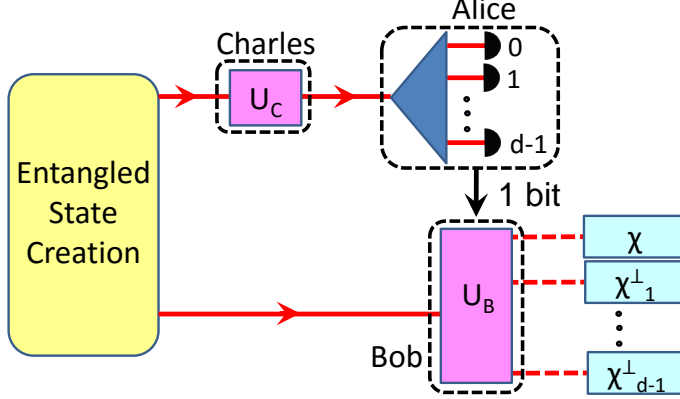


Figure 3.2: A schematic of d -dimensional remote state preparation. Charles and Bob are each given one photon of a two-photon state maximally entangled in d dimensions. Charles performs a $d \times d$ unitary operation on his photon before transmitting it to Alice. Alice performs a projective measurement on her photon with d possible outcomes and transmits the result to Bob. However, Alice’s measurement only heralds the target state χ on Bob’s photon $1/d$ times; the rest of Alice’s $d - 1$ outcomes project Bob’s photon into a state that is orthogonal to the target state. For general quantum states, Bob cannot correct any of these orthogonal states, so the protocol only succeeds $1/d$ times and Alice only needs to send Bob a one-bit message (either her measurement heralded the correct state on Bob’s photon or it did not).

information in a larger-dimensional space:

$$\begin{aligned} |\Phi^+\rangle_{A,B} &\longrightarrow (U_{C_1}|0\rangle_A)|0\rangle_B + (U_{C_2}|0\rangle_A)|1\rangle_B \\ &= (\cos\theta|0\rangle + e^{i\phi}\sin\theta|1\rangle)_A|0\rangle_B + (\cos\theta|2\rangle + e^{i\phi}\sin\theta|3\rangle)_A|1\rangle_B. \end{aligned} \tag{3.5}$$

Alice then performs a measurement on her photon in the extended basis:

$$\lambda^\pm \equiv \frac{1}{\sqrt{2}}(|0\rangle \pm |3\rangle), \quad \mu^\pm \equiv \frac{1}{\sqrt{2}}(\pm|1\rangle + |2\rangle) \tag{3.6}$$

and sends the outcome to Bob. The total state in terms of Alice’s measurement can then be written as:

$$\begin{aligned} &\frac{1}{2}[\lambda^+(\cos\theta|0\rangle + e^{i\phi}\sin\theta|1\rangle) + \lambda^-(\cos\theta|0\rangle - e^{i\phi}\sin\theta|1\rangle) \\ &+ \mu^+(\cos\theta|1\rangle + e^{i\phi}\sin\theta|0\rangle) + \mu^-(\cos\theta|1\rangle - e^{i\phi}\sin\theta|0\rangle)] \end{aligned} \tag{3.7}$$

With this larger message from Alice (2 bits for qubit RSP), Bob can transform his state into the state Charles chose using the same unitary operations as were required for QT. Such deterministic RSP protocols have been implemented for photon and ion qubit states [78, 79, 80]. However, these techniques are difficult to extend to remotely preparing larger dimensional states because the complexity of the required POVM outputs) then the dimension of the space on which they are defined. Alice needs a POVM with d^2 outcomes to implement remote state preparation for a d -dimensional state.

scales poorly. Specifically, RSP of a d -dimensional state requires a POVM with d^2 outputs, which would require nested interferometers and a single-photon counter at each output.

While both QT and RSP allow Alice to communicate quantum information to Bob using shared entanglement and a two-bit classical message, each technique has advantages and disadvantages. QT requires a full Bell-state measurement, which, as discussed in the previous chapter, is impossible to implement deterministically without nonlinear interactions [48, 49]. Furthermore, even *probabilistic*, linear QT requires an unambiguous Bell-state measurement outcome, but, as can be seen in Table 2.2, there are no detection classes which can uniquely determine any Bell state for 2-qubit linear Bell-state measurements, making it impossible to perform error-free, linear QT of ququarts without ancillas⁴. More generally, such limitations prevent error-free linear QT (without ancilla photons) of *any* states larger than qubits. In contrast, RSP only requires Alice to make measurements (which can be made deterministically) using linear optics. On the other hand, QT does not require even Charles to know what state he is sending to Alice, enabling him to implement entanglement swapping [82], which cannot be accomplished using RSP. For both higher-dimensional, deterministic QT and RSP⁵, the classical communication cost can be shown to scale as $\log_2 d^2$ with the dimension d of a quantum state that has $2d - 2$ continuous state-defining parameters (e.g., θ and ϕ in $\cos \theta |0\rangle + e^{i\phi} \sin \theta |1\rangle$) [23].

In this chapter, I describe our implementation of a new quantum communication protocol, known as superdense Teleportation (SDT), which has reduced classical information resource requirements compared to QT, simplified measurements for Alice, easier transformations for Bob, and can be implemented deterministically in (linear) optical implementations [83]. I first describe the SDT protocol and compare its resource requirements with QT and RSP. Next, I describe how we use spontaneous parametric downconversion to create photon pairs hyperentangled in polarization and orbital angular momentum. I then outline our experimental procedure for implementing SDT using hyperentangled photons, confirming that quantum information was transmitted using two-qubit single-photon tomography. Finally, I discuss the information content of the specific class of inputs states used in SDT and compare with general states with the same number of state parameters.

⁴With ancillary photons, it is possible to perform error-free QT [81]; however, practical implementations of such protocols are very challenging, requiring long counting times to produce the required photon numbers, and suffering large errors, since it is difficult to produce spectrally identical photons.

⁵Higher-dimensional QT can be accomplished with many-body interactions, and higher-dimensional RSP requires large POVMs.

3.2 Superdense Teleportation

The state transfer techniques described in the previous section are used to send completely general quantum states. However, if we remotely prepare only qubit states that are constrained to lie on a great circle of the Poincaré sphere, this requires only a single bit transferred from Alice to Bob [84, 85]. Furthermore, this idea of transmitting a state from a constrained portion of Hilbert space may be extended to higher dimensional states [86, 87, 88]; the resulting technique, superdense teleportation (SDT), can be used to send states at a reduced classical information cost per state parameter [83]. SDT is somewhat similar to the standard RSP protocol in that Charles encodes the state parameters that he wishes to communicate to Bob directly onto Alice's half of the entangled state. However, unlike traditional RSP, instead of attempting to send a general qudit (d -dimensional quantum state), requiring all $2d - 2$ state-defining parameters, Charles only attempts to send a state with $d - 1$ state-defining parameters. These parameters correspond to the relative phases of an equimodular state (also known as an equatorial qudit [89]):

$$(|0\rangle + e^{i\phi_1}|1\rangle + e^{i\phi_2}|2\rangle + \dots + e^{i\phi_{d-1}}|d-1\rangle)/\sqrt{d}. \quad (3.8)$$

To transmit this state, one photon of a d -dimensional entangled state is distributed to Charles and the other is distributed to Bob. Charles then applies phases to his photon, rotating the two-photon state to the following:

$$\begin{aligned} \frac{1}{\sqrt{d}}(|00\rangle + |11\rangle + |22\rangle + \dots + |(d-1)(d-1)\rangle) &\xrightarrow{U_C} \\ \frac{1}{\sqrt{d}}(|00\rangle + e^{i\phi_1}|11\rangle + e^{i\phi_2}|22\rangle + \dots + e^{i\phi_{d-1}}|(d-1)(d-1)\rangle), \end{aligned} \quad (3.9)$$

and sends his modified half of the entangled state to Alice. She then measures her qudit in a basis which is mutually unbiased to the one Charles used to apply the phases, and sends the measurement outcome, only $\log_2 d$ bits, to Bob, who then performs one of d relative-phase-shifting unitary transformations on his particle to recover the intended state in Equation 3.8.

The reduction in classical information required by SDT is not only interesting from a theoretical point of view but is also accompanied by significant experimental simplifications. Chief among these is the reduced complexity of the measurements (e.g., number of interferometers and detectors) that Alice must make on her half of the entangled state. As mentioned above, measurements required for QT are either probabilistic (for qubit teleportation) or are impossible to do without nonlinear interactions. Furthermore, although RSP can be performed deterministically using linear interactions for states of any dimension by using POVMs, the

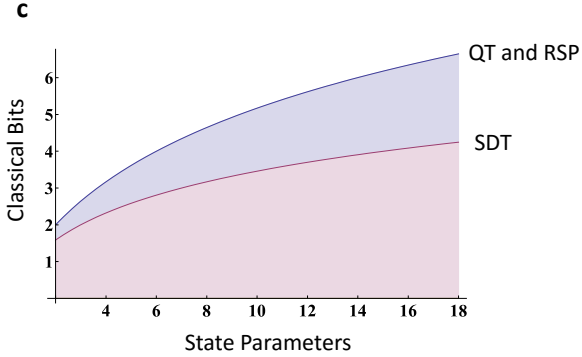


Figure 3.3: The required number of transmitted classical bits for quantum teleportation (QT), RSP and superdense teleportation (SDT) as a function of the number of parameters teleported; for a large number of parameters, the ratio of classical bits needed for QT and RSP to bits needed for SDT approaches 2.

	State dimension	Success prob.	Classical bits	Alice's Detector #	Bob's Correction #	State known to Charles
QT	2^*	$1/2$	2	4	4	optional
RSP (probabilistic)	$\frac{N+2}{2}$	$\frac{2}{N+2}$	1	1	1	required
RSP (deterministic)	$\frac{N+2}{2}$	1	$2 \log_2(\frac{N+2}{2})$	$(\frac{N+2}{2})^2$	$(\frac{N+2}{2})^2$	required
SDT	$N + 1$	1	$\log_2(N + 1)$	$N + 1$	$N + 1$	required

Table 3.1: Resources required to send N state parameters with 100% fidelity for each technique using linear optics. Superdense Teleportation (SDT) uses a high-dimensional input state to transmit quantum state parameters with less classical communication and fewer detectors and transformations than both standard quantum teleportation (QT) and deterministic remote state preparation (RSP). While probabilistic RSP can transmit state information with very few experimental resources, the probability of successful state transmission is inversely proportional to the number of parameters being transmitted. Note that QT of dimension $d > 2$ requires nonlinear optics or the addition of entangled ancilla qubits [81]. QT is also the only technique that does not require the transmitted state to be known to a state chooser (Charles), as would be required, e.g., to implement entanglement swapping [82].

complexity of the measurement increases quadratically with the state dimension: a d -dimensional state with $2d - 2$ state parameters requires a POVM with d^2 outputs and detectors. SDT, in contrast, requires only a comparatively simple d -dimensional mutually unbiased basis measurement to teleport a d -dimensional state with $d - 1$ state parameters (see Fig. 3.1c). While SDT sends only half the number of state parameters associated with a d -dimensional state, the complexity of the experiment is greatly reduced. For example, the number of detectors scales linearly with the state dimension for SDT instead of quadratically as in RSP. Moreover, the number of different transformations Bob needs to implement are thus also reduced to linear scaling with the dimension—much easier than the quadratic scaling for deterministic RSP (and QT). Table 3.1 summarizes the resource requirements of each protocol.

3.3 Experimental Implementation

3.3.1 Hyperentangled State Creation

To experimentally demonstrate SDT's advantages over QT and RSP (e.g., reduced classical communication cost and experimental measurement simplification), states with at least two quantum parameters must be transferred (see Fig. 3.1c). We experimentally demonstrate SDT by transmitting equimodular ququart states (4-dimensional quantum states with three independent state parameters). This may be accomplished by preparing entangled states in four modes of one degree of freedom, such as spatial or temporal mode. Instead, however, we used states that are hyperentangled in polarization and orbital angular momentum to produce four-mode entangled states [90].

To create the required hyperentangled states we combined the twin-crystal polarization entanglement source with the orbital angular momentum entanglement source (see Sections 1.3.1 and 1.3.3), by pumping a pair of orthogonally-oriented nonlinear type-I phase-matched BBO crystals with a 351-nm Ar⁺ laser (see Fig. 3.4). With small probability, a high-energy photon may be split by the nonlinear crystals into two lower energy photons that are entangled in polarization. Then, by selecting only the ± 1 orbital angular momentum modes using holograms and single-mode fibers, we create a state that is maximally entangled in both polarization and spatial mode:

$$\frac{1}{2}(|HH\rangle + |VV\rangle) \otimes (|rl\rangle + |lr\rangle), \quad (3.10)$$

where r and l are eigenfunctions of the orbital angular momentum operator with $\pm\hbar$ orbital angular momentum. One photon of the resulting state was sent to both Charles and Bob.

3.3.2 Quantum Message Encoding and Measurement

To encode the three state parameters that Alice must teleport to Bob, Charles applied phases using liquid crystals and by varying the phase between the two spatial modes, which were processed using a binary forked hologram. As discussed in Section 1.3.3 these silver-halide holograms were used in conjunction with single-mode fibers to transform the states into two Gaussian modes in the ± 1 diffraction orders, respectively (with $\sim 30\%$ efficiency). After these transformations the total 2-photon entangled state was:

$$\frac{1}{2}(|00\rangle + e^{i\phi_1}|11\rangle + e^{i\phi_2}|22\rangle + e^{i\phi_3}|33\rangle), \quad (3.11)$$

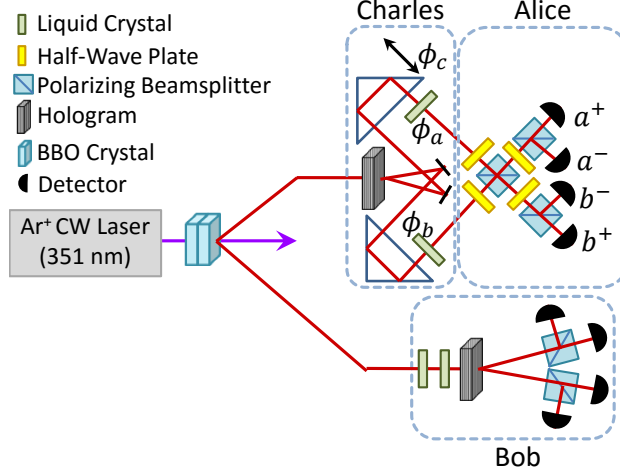


Figure 3.4: Experimental setup for SDT implementation. Charles applies phases to Alice’s photon using liquid crystals and by adjusting an interferometer path length. These phases are linear combinations of the phases given in Equation 3.13 ($\phi_a = \phi_1 - \phi_3 + \pi/2$, $\phi_b = \phi_2 - \pi/2$, and $\phi_c = \phi_3 - \pi/2$), but still span the space of equimodular states that Charles can prepare. Alice then makes a single-photon two-qubit Bell-state measurement on the polarization and spatial mode of her photon [57]. By measuring in coincidence with Alice, Bob can determine the state heralded by each of Alice’s measurements.

where $|0\rangle \equiv |Hr\rangle$, $|1\rangle \equiv |Hl\rangle$, $|2\rangle \equiv |Vr\rangle$, and $|3\rangle \equiv |Vl\rangle$ (in reality the labels are reversed for Alice and Bob, but this does not qualitatively affect the results). Charles then sent the photon on to Alice, who combined the two spatial modes on a polarizing beamsplitter to form a “spin-orbit” CNOT gate [57] (See Section 2.2.1). By making polarization measurements on the output spatial modes, Alice effectively made measurements in the following basis (which is mutually unbiased to the basis in which Charles applied the phases):

$$|a^\pm\rangle \equiv (|Dr\rangle \pm |Al\rangle)/\sqrt{2}, \quad |b^\pm\rangle \equiv (|Dl\rangle \pm |Ar\rangle)/\sqrt{2}. \quad (3.12)$$

The two-photon four-qubit state can then be written as

$$\begin{aligned} & \frac{1}{4} [|a^+\rangle(|0\rangle + e^{i\phi_1}|1\rangle + e^{i\phi_2}|2\rangle - e^{i\phi_3}|3\rangle) + |a^-\rangle(|0\rangle - e^{i\phi_1}|1\rangle + e^{i\phi_2}|2\rangle + e^{i\phi_3}|3\rangle) \\ & + |b^+\rangle(|0\rangle + e^{i\phi_1}|1\rangle - e^{i\phi_2}|2\rangle + e^{i\phi_3}|3\rangle) + |b^-\rangle(-|0\rangle + e^{i\phi_1}|1\rangle + e^{i\phi_2}|2\rangle + e^{i\phi_3}|3\rangle)]. \end{aligned} \quad (3.13)$$

Where states $|a^\pm\rangle$, $|b^\pm\rangle$ refer to Alice’s photon, while $|0\rangle$, $|1\rangle$, $|2\rangle$, and $|3\rangle$ refer to Bob’s. Therefore, Alice’s measurement projects Bob’s photon into a state that can be corrected by making a π phase shift on the relevant term.

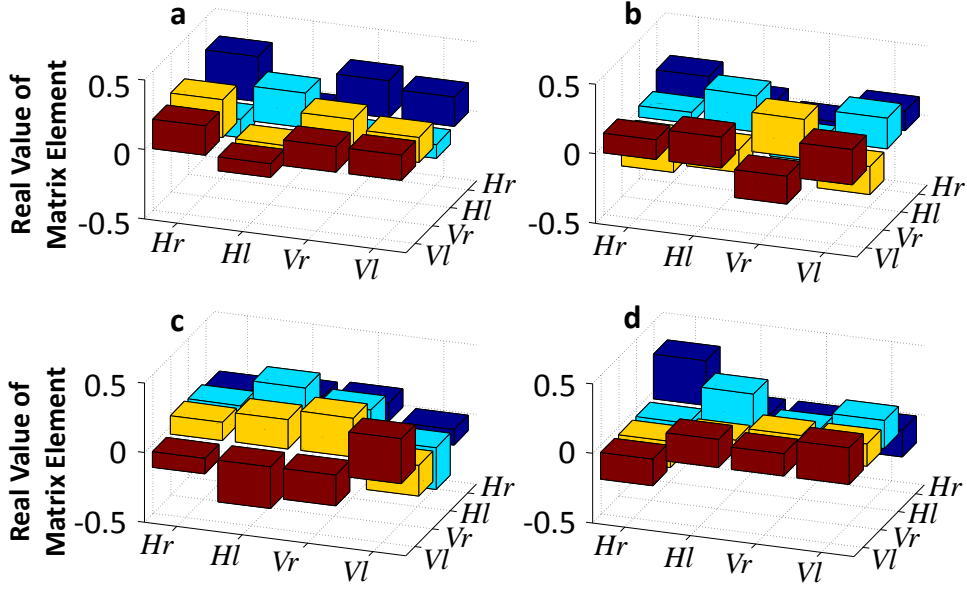


Figure 3.5: Reconstructed density matrices (real parts) without Bob’s corrections. Each of the four panels shown above corresponds to the state that Bob receives for each of Alice’s four measurement outcomes. For each state that Charles prepared, Alice measured in a basis that is mutually unbiased in the basis in which Charles applied phases. Each of Alice’s measurement outcomes projected Bob’s photon into one of four orthogonal states. By performing a two-qubit polarization and orbital angular momentum tomography in coincidence with Alice’s measurement, Bob reconstructed the density matrix of each of these states. **(a-d)** Each of these four density matrices are in the horizontal and vertical polarization basis (H and V) and the right and left orbital angular momentum basis (r and l). The major limiting factor of fidelity in these reconstructions is the crosstalk between orbital angular momentum modes indicated by the differing values of the diagonal elements (which should be equal for equimodular states). After these matrices were reconstructed, Bob numerically performed the corrective transformations to obtain the final reconstructed states shown in Fig. 3.7.

3.4 State verification through tomographic reconstruction

In our proof-of-principle experiment, we did *not* apply these phases for each photon as its partner was detected, which would have required photon storage and feed-forward state correction (see Section 3.5.1). Instead, Bob performed a full 2-qubit single-photon tomography on his photon using liquid crystals and a scanning hologram [90]. Bob’s hologram, like Charles’, was used in conjunction with single-mode fibers to convert a particular spatial mode into a Gaussian mode in the ± 1 diffraction orders; using this technique, it was possible to make spatial-mode measurements on the photons in different bases. Since different regions of the hologram (used in conjunction with single-mode fibers) converted different spatial-modes to Gaussians, taking a complete polarization tomography at each hologram region enabled a tomographically over-complete set of polarization and spatial-mode measurements on Bob’s photon ($\{H, V, D, A, R, L\} \otimes \{h, v, d, a, r, l\}$), where $h \equiv (r + l)/\sqrt{2}$, $v \equiv (r - l)/\sqrt{2}$, $d \equiv (r + il)/\sqrt{2}$, and $a \equiv (r - il)/\sqrt{2}$ are the set of spatial-mode

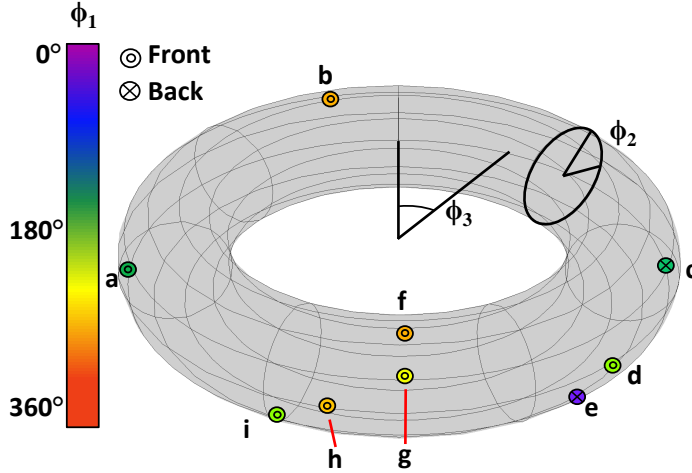


Figure 3.6: A visual representation of the distributions of the states communicated from Alice to Bob using SDT. The states that were measured can be represented as lying on a three-dimensional hypertorus (one dimension for each state parameter) embedded in a six-dimensional Euclidean space for general ququart states. The average fidelity of all teleported states was 87.0(1)%. ‘Front’ in the legend refers to point locations on the side towards the viewer in this perspective, while ‘back’ refers to those obscured by the front surface. The ϕ_1 parameter can be read from the fill-color of the circle surrounding the point locator on the surface of the torus parameterized by ϕ_2 and ϕ_3 .

projections. Correlating Bob’s measurement outcomes with Alice’s, we used maximum likelihood state reconstruction (see Appendix E) [91] to determine what state Bob received for each of Alice’s measurement outcomes (see Fig. 3.5). Finally, we then numerically applied the transformation indicated by Alice’s measurement outcome to the reconstructed states, to compare with the original state intended to be transmitted.

The average fidelity over all the measured teleported states (see Fig. 3.6 and 3.7) was 87.0(1)%, approximately twice the 44% average fidelity limit for sending pure equimodular ququart states over a classical channel without entanglement (see Appendix B). For comparison, perfect QT of a qubit exceeds the classical limit by $\Delta F_{\text{qubit}} \equiv F_{\text{average}}^{\text{quantum}} - F_{\text{average}}^{\text{classical}} = 1 - 2/3 = 33\%$ [92], and actual achieved results are lower, often much lower. In addition, recent improvements in spatial-mode sorting could increase the fidelity of SDT even further [93].

As seen in Fig. 3.5, the diagonal elements of our reconstructed density matrices are not all equal, in contrast to the theoretical expectation for equimodular states. This inequality appears to arise from spatial-mode crosstalk in both Alice and Bob’s measurements; such crosstalk is the main limitation in the fidelity of the reconstructed states. We also examined how well each of the phases that Charles sent was transferred from Alice to Bob. From our state reconstructions, we estimate that the systematic error in the phases of Bob’s reconstructed states was $\pm 4.0^\circ$ for each ϕ_a , ϕ_b , and ϕ_c (see Fig. 3.4 for definitions of these phases in terms of ϕ_1 , ϕ_2 , and ϕ_3). This deviation suggests that Charles and Alice can reliably communicate nearly

Figure	Target Phases (°)	Measured Phases (°)	Ave. Fidelity (%) with Target State
a	112, 180, 278	109.7(5), 176.0(6), 283.7(5)	86.2(3)
b	270, 90, 324	266.4(6), 80.7(7), 309.5(7)	85.7(3)
c	112, 277, 119	113.0(5), 272.4(6), 122.9(6)	87.8(3)
d	180, 180, 137	175.6(5), 176.8(5), 141.2(6)	86.9(3)
e	26, 202, 145	23.7(4), 204.4(5), 154.9(4)	86.4(2)
f	270, 90, 184	262.0(7), 80.8(6), 193.7(7)	86.8(3)
g	211, 158, 185	208.5(4), 162.9(4), 191.0(4)	88.4(3)
h	268, 148, 209	273.2(5), 141.4(5), 208.9(6)	86.2(3)
i	180, 277, 223	176.4(5), 272.6(5), 222.6(6)	89.2(2)

Table 3.2: Summary of experimental results. Bob’s measurement results for each set of target phases chosen by Charles. For every teleported state Bob received, a density matrix was reconstructed which was used to calculate the measured phases and the fidelity of the teleported state with the target state.

$10^5 (= (\frac{360^\circ}{2 \cdot 4.0^\circ}))$ distinguishable states to Bob.

In addition to the full state tomographies, we also made partial reconstructions over a much larger number of input phases, in order to verify that Charles and Alice could teleport a wide range of phase settings to Bob. For these measurements, Charles varied one of the three phases while keeping the other two constant. Then, instead of making all 36 measurement configurations for a full two-qubit tomography for each of Charles’s phase settings, Bob only made specific measurements to find the values of the three interferometric functions which varied with phase ($\langle Hh|\rho|Hh\rangle$, $\langle Dr|\rho|Dr\rangle$, and $\langle Dl|\rho|Dl\rangle$, where ρ is the density matrix describing the state of Bob’s photon). Each of these measurements varied uniquely with each of the phases Charles applied, resulting in phase-dependent fringe curves (see Fig. 3.8). Some measurements displayed unexpected phase dependence, varying with phases of which they were supposedly theoretically independent. This deviation from the expected measurement/phase relationship is further evidence that spatial-mode crosstalk is a limiting factor in this proof-of-principle experiment.

3.5 Discussion

All improvements in both classical communication cost and experimental simplification can be associated with the topology of the constrained space in which the equimodular states reside, specifically, a type of hypertorus, which is topologically different from the space associated with general quantum states of the same number of parameters. Because of this topological difference, it is possible to perform universal NOT (within the restricted portion of the space) gates, which are impossible to implement for general quantum states [74]. As was previously mentioned for qubit RSP, it is the impossibility of this operation over general quantum states that requires Alice to use a POVM and *two* classical bits in RSP in order to send Bob enough

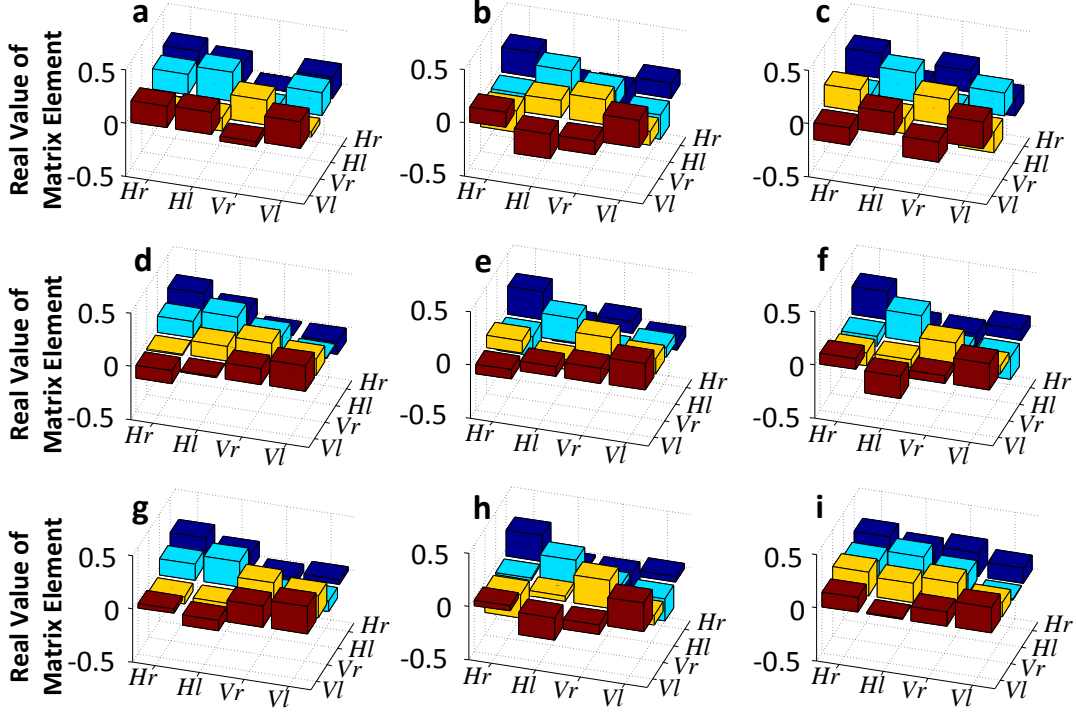


Figure 3.7: Reconstructed density matrices of transmitted states. Each of the panels above corresponds to a quantum state transmitted from Alice to Bob using superdense teleportation. For each of these states, Bob performed a full two-qubit quantum state tomography in polarization and orbital angular momentum. By correlating his measurements with Alice’s measurement results and numerically performing corrective transformations, Bob reconstructed the density matrix of the state that Alice transmitted. Each panel shows the reconstructed density matrices (for clarity we display only the real parts of these matrices; however, the full complex matrix elements are needed to calculate the fidelity and other relevant parameters) in the horizontal and vertical polarization basis (H and V) and the right and left orbital angular momentum basis (r and l). The panel labels (a–i) correspond to the letters in Fig. 3.4 and Table 3.2, which list the target states and state fidelities.

information to transform his state to the target state. In one-parameter SDT, the “universal” NOT gate (mapping all one-dimensional equimodular states to their orthogonal) required for Bob to recover the target state is just a simple π -phase shift between two basis states. When moving to higher dimensional spaces, Bob must be able to perform an entire set of universal NOT gates that transform an input state to each of the orthogonal states which Alice’s measurements herald. Again, these transformations are impossible to implement for general qudit states, but are simple relative phase shifts for inputs restricted to the set equimodular states used in SDT.

The topological structure of equimodular states also influences their information content. In particular, the parameters of an equimodular state sweep out a more significant portion of Hilbert space than an equivalent number of parameters in a lower dimensional general quantum state (e.g., $\frac{4\pi^2}{3} = 13.2$ versus $4\pi =$

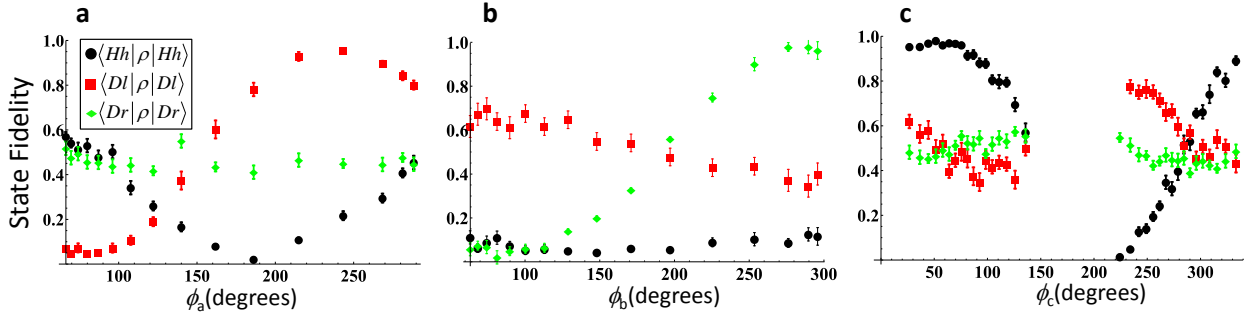


Figure 3.8: Measurement fringes as a function of Charles' phases. For each panel only one phase is varied while the others are fixed. (a) The theoretical fidelity range ($\Delta f \equiv \text{maximum} - \text{minimum}$) for the black, red and green data points are $\Delta f = 0.5, 1$ and 0 , respectively; (b) the theoretical fidelity range values are $\Delta f = 0, 0$ and 1 , respectively; (c) theoretical fidelity range values are $\Delta f = 1, 0$ and 0 , respectively. Error bars represent standard deviation and are calculated through Monte Carlo simulation assuming Poissonian statistics. The larger-than-predicted fidelity range of some of these curves arises from crosstalk in the polarization/ spatial-mode measurements. The missing strip of data around 180° in the final figure was due to instability in the active feedback system used to stabilize our interferometer at angles near this value of ϕ_c .

12.6 for two-parameter state communication using SDT or QT, respectively)(see Appendix B). In fact, the ratio of the volume of the space of equimodular states to the corresponding space of general quantum states grows exponentially with the number of state parameters (see Appendix B). This volume ratio is related to the ratio of the number of states that can be “packed” into the two volumes: as the dimension increases, an exponentially larger number of statistically distinguishable states (for a small minimum statistical distance between states) can be packed into the class of equimodular states (hypertorus) than into the class of general states (hypersphere) with the same number of state parameters. A second perspective of why equimodular states have greater information content can be understood by examining the amount of information that can be inferred about general and equimodular states from a single-shot measurement. We define “classical teleportation” as the optimal strategy for guessing a quantum state given a single-shot measurement [92], which is equivalent to the optimal strategy for Alice to communicate an unknown state to Bob by sending the result of a single measurement without shared entanglement. With this definition, the average fidelity of classical teleportation is lower for the equimodular states used in SDT ($\langle F_{\text{classical teleportation}} \rangle = \frac{2N+1}{(N+1)^2}$) than for general quantum states ($\langle F_{\text{classical teleportation}} \rangle = \frac{4}{N+4}$) of the same number of quantum parameters (N) used in quantum teleportation and RSP (see Appendix B) [94]. This is an indication that SDT not only requires transmitting fewer classical bits to teleport the quantum parameters, but that these parameters in some sense contain more information on average than the parameters of general states used in RSP and QT.

	PC1	PC2	PC2
a^+	on	on	on
a^-	off	off	off
b^+	off	on	on
b^-	on	off	off

Table 3.3: A list of which Pockels cells (PC) Bob activates in order to correct his state based on the outcome of Alice’s measurement. This table assumes the experimental configuration shown in Figure 3.9.

3.5.1 Extending to Feed-Forward Correction

While we did not perform feed-forward state correction in this experiment, we can outline one possible way to extend our implementation to allow Bob to perform corrective transformations on his photons based on Alice’s measurement outcomes. For this extension, two main modifications must be made to our implementation (see Fig. 3.9). First, Bob must have a way of storing his photon to allow Alice time to measure her photon and transmit the outcome to Bob. Perhaps the easiest way to store a photon for sufficient time (~ 25 ns) is to use an optical delay line. Secondly, Bob must possess a way of quickly applying the corrective unitary transformations on his photon to convert it to the target state based on Alice’s message (see Equation 3.13). Bob might make these transformations quickly using Pockels cells placed before and after his hologram and thus perform full feed-forward correction of his state. However, depending on the type of Pockels cells that Bob is using, he might not be able to apply a phase shift to one polarization state without affecting the other polarization. For example, if an X-cut two-crystal RTP Pockels cell aligned at 0° is used, then only rotations of this form can be applied (see Appendix C):

$$\begin{array}{cc} |H\rangle & |V\rangle \\ |H\rangle & \left[\begin{array}{cc} e^{-\frac{i\pi}{2}} & 0 \\ 0 & e^{\frac{i\pi}{2}} \end{array} \right], \\ |V\rangle & \end{array} \quad (3.14)$$

which will always induce phase shifts on both polarizations. Therefore, Bob needs to use an additional birefringent element, such as a quarter-waveplate, in one of the hologram orders to perform the required corrective transformations (see Equation 3.11)⁶ (see Fig. 3.9). Then, depending on Alice’s measurement, Bob applies voltages on different combinations of the three Pockels cells to recover the state that Charles chose (see Table 3.3).

⁶Alternately, Charles could modify the phases that he applies to the different terms of Equation 3.11. If Charles redefined $\phi_1 \rightarrow \phi_1 + \pi$, then Bob could correct his state using the same corrective transformations described in Figure 3.9 and Table 3.3, except without the additional quarter-waveplate in the r hologram order.

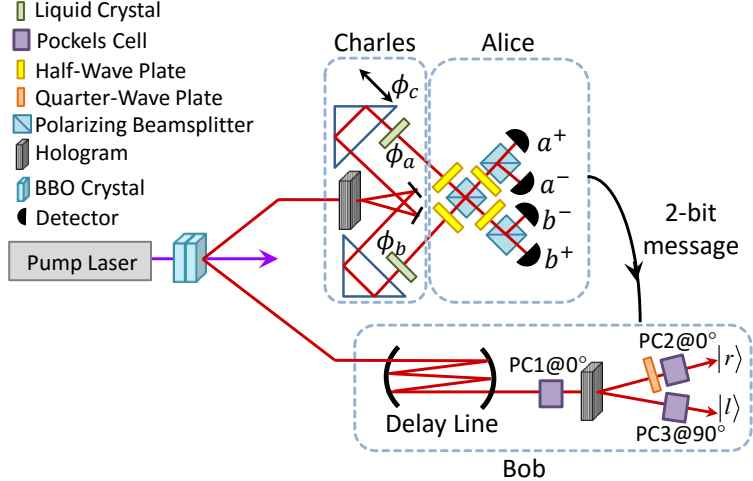


Figure 3.9: An experimental configuration for implementing SDT with feed-forward correction. The addition of a delay line and Pockels cells allows Bob to store his photon until he receives the result of Alice’s measurement and quickly make the corrective unitary transformation based on her message. Bob can then verify that he received the correct quantum state through tomography (not shown).

3.6 Conclusion and Outlook

We have implemented an entanglement-enhanced quantum state communication protocol which can communicate quantum state parameters with less classical information transfer and simpler measurements than standard quantum teleportation or remote state preparation. Using superdense teleportation we were able to transfer a wide variety of states from Alice to Bob with much better fidelity than classical teleportation would allow. In addition to the pure target states that were teleported in this experiment, these techniques might also be extended to transfer partially mixed equimodular states as well. We also speculate that SDT might be used to exchange quantum state inputs between a client and quantum server in blind quantum computing [95]. It should be noted that both SDT and RSP are closely related to quantum steering⁷ [96]. We are currently investigating the application of recent advances in quantum steering and semidefinite programming to the quantum states reconstructed in this experiment [97, 98]. Because universal NOT operations can be performed on equimodular states, they might also have interesting applications in ideal quantum cloning [89] and in dynamical decoupling noise-reduction techniques [99]. Finally, this research shows that equimodular states have topological features that might make them superior to general states for quantum state communication (i.e., the power of SDT comes from the fact that equimodular states are topologically different from general quantum states) and motivates further investigations into how such constrained states

⁷Quantum steering is a nonlocality test in which two parties (Alice and Bob) share a bipartite state. Alice attempts to “steer” Bob’s particle to a particular state by making measurements on her particle. If Alice can successfully steer the state of Bob’s particle, then they can violate a set of steering inequalities to prove that the bipartite state that they share exhibits nonlocal correlations.

might be used to optimize other quantum information techniques. For example, equimodular states are precisely those necessary to implement quantum fingerprinting⁸ [100].

⁸Fingerprinting is a protocol in which two parties wish to confirm that they share an identical string of bits using minimal communication. To accomplish this, they both send a small message or “fingerprint” calculated from their bit string to a trusted referee, who tells them whether or not the fingerprints match. If the two parties do not share a random key, then they can exponentially shrink the required length of the fingerprint by encoding it on a quantum state.

Chapter 4

Designing Quantum Communication Systems for Satellites

Portions reproduced in part with permission from T.M. Graham, C. Zeitler, J. Chapman, P.G. Kwiat. Superdense Teleportation and Quantum Key Distribution for Space Applications. *2014 IEEE International Conference on Space Optical Systems and Applications (ICSOS)*. ©2015 IEEE

4.1 Introduction

While there have been many laboratory demonstrations of quantum communication protocols, field implementations of such techniques are rarer because of complexities including loss and quantum state drift. However, despite such challenges a number of fiber- and free-space-based quantum communication protocols have been implemented over long distances. In particular, fiber implementations of quantum key distribution networks have been implemented in several places, including Boston [101], Vienna [102], and Tokyo [103]. However, optical signal loss when propagating through a fiber grows exponentially with fiber length, so fiber-based quantum communication cannot be implemented over arbitrarily long distances¹. Quantum repeaters can be used to reduce effective channel loss using quantum teleportation. However, the development of practical low-loss, high-bandwidth quantum repeaters is still a very active area of research. Even if such quantum repeater networks can be implemented with high fidelity and low loss, the number of nodes needed to implement a state-wide (let alone a nation- or world-wide) network is daunting. An alternate approach is to use free-space communication channels, where transmission (mostly limited by optical beam truncation) scales as a power of distance ($\propto \frac{1}{L^2}$) rather than as an exponential of distance ($\propto e^{-\alpha L}$), allowing for much longer communication distances. Such free-space quantum communication protocols have been demonstrated over long distances in terrestrial experiments. Notably, quantum teleportation has been performed over a distance of 143 km between La Palma and Tenerife of the Canary Islands [105] and 97 km between the cities of Gangcha and Guanjing, China [106]. However, free-space *terrestrial* quantum communication implemen-

¹Actual distance limitations depend on the particular quantum communication protocol. Quantum cryptography using coherent states has been successfully demonstrated over distances of 250 km (though at secure key rates of only ~ 15 bits/second) [104]. Entanglement-based protocols, such as teleportation, are far more sensitive to loss.

tations are constrained by line-of-sight and turbulence limitations. Developing a satellite-based quantum network is potentially the most practical way of establishing reliable quantum communication between very distant parties on Earth. While the establishment of such a network is beyond current technology, many initial steps are currently feasible. In particular, the distribution of quantum entanglement between a satellite and a terrestrial target would demonstrate a key ingredient for a future world-wide quantum network. Such a demonstration would enable several quantum communication protocols to be implemented.

In this chapter, we discuss strategies to distribute entanglement over a long-distance free-space link. We then describe how they can help implement superdense teleportation (SDT) [83, 86, 87, 88] and a four-dimensional variant of the well-known BB84 quantum key distribution protocol [24]. We will then present a tabletop demonstration of SDT and discuss the future directions for adapting this prototype for an International Space Station (ISS)-to-Earth implementation building on our previous studies [107].

4.1.1 Transmitting Photonic Qubits from a Satellite

The production of high-fidelity quantum states is the first step of any entanglement-based quantum communication protocol. These states can be encoded in different physical degrees of freedom of photons, e.g., polarization, spatial distribution, arrival time, etc. However, care must be taken that the quantum channel does not disrupt these properties. Spatial-mode encoding has been successfully used to greatly increase the capacity of a relatively short classical communication channel [108], but atmospheric turbulence, as discussed in Sections 1.2.2 and 2.2.3, will disrupt the phase coherence of spatial qubits transmitted over long-distance free-space channels [15, 109], and high beam divergence will also prevent high-order spatial-modes from being collected efficiently. For our quantum communication implementation, we have chosen to use polarization and arrival time to encode quantum information.

Photon polarization appears to be an ideal photonic degree of freedom for long-range satellite-to-ground quantum communication. As mentioned in Chapter 1, photon polarization provides a natural qubit structure and is easily manipulated and measured using birefringent elements and polarizers. Additionally, since there are no strongly birefringent elements or polarization-dependent scattering elements in the atmosphere, a quantum channel between an orbiting satellite and a terrestrial telescope will not disrupt a polarization qubit. However, while the atmosphere itself will not be disruptive, geometric effects due to changes in the beam pointing as the satellite passes overhead can cause polarization rotation [107]. Similarly, the mirrors used in beam-pointing systems can induce an angle-dependent birefringent phase as well as polarization-dependent loss. These effects must be characterized and compensated to effectively use polarization qubits in a satellite-to-Earth quantum communication protocol.

Photon arrival time can also be effectively used to transmit quantum information from a satellite to a terrestrial receiver. A qubit can be encoded on the photon arrival time by using two discrete temporal modes, e.g., early and late time bins (see Section 1.2.2). While arrival time can be used as an effective qubit, the relative motion between the satellite and telescope will result in a time-dependent time-bin separation. Details of compensation strategies and the results of our preliminary implementation are provided in Sections 4.4.1.

4.2 Superdense Teleportation

One of the most practical ways to test a quantum channel is to use it to perform a useful quantum protocol; however, several factors must be considered to determine which test protocol is appropriate. Quantum key distribution is the most practically realized type of quantum communication protocol, but it does not *require* entanglement to implement, in contrast to many advanced quantum applications which do require distribution of entangled states, such as a quantum network. For this reason, demonstrating a quantum communication protocol which requires entanglement would be an important step to implementing many more advanced quantum communication protocols beyond quantum cryptography. On the other hand, while quantum superdense coding [22] and quantum teleportation [5] both require entanglement, both of these techniques would be very challenging to implement between a satellite and a terrestrial telescope. Superdense coding requires either an indefinitely long quantum memory (not feasible with current technology) or a double use of the very lossy quantum channel between satellite and ground observer. Quantum teleportation is much more feasible than superdense coding and has already been used in long-range demonstrations; however, it requires more than one photon pair to implement. The additional photon pair required by this technique would drastically reduce the rate of successful teleportation events, thereby greatly reducing the experimental signal-to-noise ratio. These aspects, in addition to the fact that the orbital motion of a satellite will limit collection duration, make a satellite-based implementation of quantum teleportation very challenging.

SDT is much easier to implement over long distances than superdense coding or quantum teleportation. The proof-of-principle demonstration of this technique, described in the previous chapter, used photons that were hyperentangled in polarization and orbital angular momentum [110]. However, as mentioned above, such spatial-mode qubits are not well suited for long-distance quantum communications. By implementing SDT with photons hyperentangled in polarization and arrival time, we will provide a laboratory demonstration to inform an implementation of SDT from a satellite.

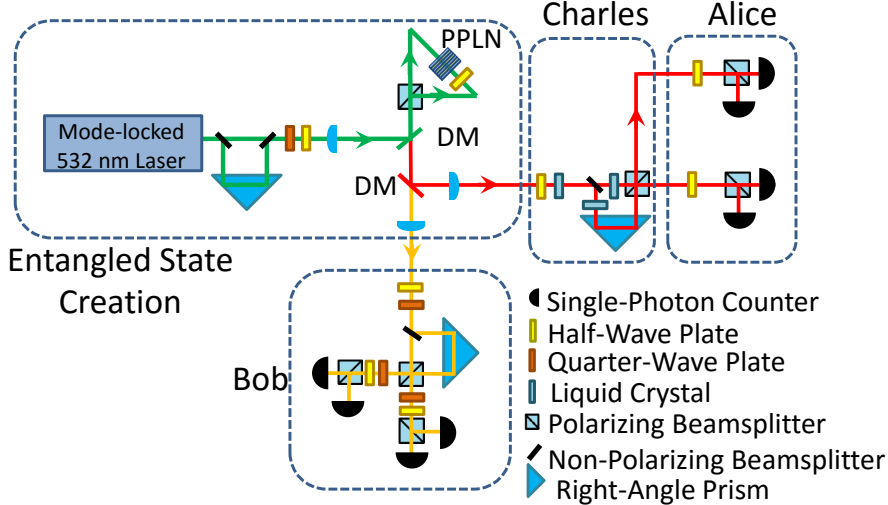


Figure 4.1: Our experimental implementation of SDT using polarization and temporal mode. We use non-degenerate type-0 spontaneous parametric downconversion in periodically-poled lithium niobate crystals (PPLN) to create a state hyperentangled in polarization and temporal mode. The entangled photon pairs are separated using dichroic mirrors (DM). Charles probabilistically separates the two temporal modes and applies phases using liquid crystals. After the output of Charles' interferometer, Alice then performs her measurement using polarizing beamsplitters and single-photon counters. Bob performs an informationally complete set of measurements to characterize the state of his photon. By detecting in coincidence with Alice, Bob can determine how successful Alice's measurement was at heralding the target state.

4.3 Experimental Prototyping

Before attempting to implement quantum communication protocols from a satellite, we have demonstrated the experimental setup in a laboratory tabletop experiment. Information obtained in these preliminary experiments can then be used to inform the development of a compact, robust implementation to be installed on the ISS.

4.3.1 Source Development

Polarization and Temporal Mode Generation

As stated in Section 4.1.1, our experiments require a source of photons that are hyperentangled in polarization and temporal mode. These hyperentangled photon pairs were created by combining the Sagnac polarization source with the temporal-mode entanglement source described in Sections 1.3.1 and 1.3.2. Specifically, photon pairs are created by pumping a 20-mm long magnesium-oxide-doped periodically poled lithium niobate (PPLN) crystal to downconvert a 532-nm horizontally polarized photon into two lower energy, horizontally polarized photons (one at 810 nm and one at 1550 nm). Using an unbalanced Mach-Zehnder interferometer followed by a polarizing Sagnac interferometer, 532-nm pump photons were prepared in the

following superposition (see Fig. 4.1):

$$\frac{1}{2} (|\circlearrowleft\circlearrowleft\rangle + |\circlearrowright\circlearrowright\rangle) \otimes (|t_1 t_1\rangle + |t_1 t_1\rangle), \quad (4.1)$$

where \circlearrowleft and \circlearrowright represent clockwise and counter-clockwise paths in the Sagnac, respectively. The resulting photons created in this process are hyperentangled in spatial and temporal mode. As the downconversion photons exit the polarizing Sagnac, the spatial-mode entanglement is converted into polarization entanglement (i.e., $\circlearrowleft\circlearrowleft \rightarrow VV$ and $\circlearrowright\circlearrowright \rightarrow HH$), resulting in the following state:

$$\frac{1}{2} (|HH\rangle + |VV\rangle) \otimes (|t_1 t_1\rangle + |t_1 t_1\rangle). \quad (4.2)$$

The 810-nm (1550-nm) photons are reflected (transmitted) using a dichroic mirror.

For reliable implementation of quantum protocols, it is important to assess the quality of the entangled states generated. We tomographically reconstructed the state of the output photons by making an informationally complete set of measurements on many state copies, building up a relative probability distribution for outcomes of measurements made on the quantum state. We performed these measurements on the polarization of our photon pairs by using waveplates and polarizers to measure each photon in an over-complete set of measurements $\{(H, V, D, A, R, L)_{Alice}, \otimes (H, V, D, A, R, L)_{Bob}\}$. Maximum-likelihood state reconstruction was then used to determine the quantum state most likely to yield the observed results (see Appendix E). Only a partial tomography was performed on the temporal mode, measuring relative probabilities of the $|t_1 t_1\rangle$ and $|t_2 t_2\rangle$ terms of the quantum state and then measuring the coincidence visibility in the $(\frac{t_1+t_2}{\sqrt{2}}) \otimes (\frac{t_1-t_2}{\sqrt{2}})$ basis². Even though this set of measurements is not informationally complete, we can use it along with the assumption that both photons of each pair are created in the same temporal mode to estimate the temporal mode of our photon pair state. Using these techniques we estimate our polarization state fidelity to be 98% and the temporal-mode state fidelity to be 98%.

Bandwidth Measurement of Bob's Photons

In addition to characterizing the downconversion polarization and temporal-mode state, it is important to understand the bandwidth of the photons that Bob receives. While this knowledge is not expressly required for the laboratory demonstration, it is very important for satellite-to-Earth implementations, since the downconversion bandwidth constrains how much background light can be filtered out of Bob's measurements

²A full tomography was not performed on the temporal mode state because of the difficulty of setting the phase between the two time bins without disrupting the stabilization. A full tomography of the state will be performed in future measurements by using measurements in a polarization and temporal mode hybrid basis (see Equation 4.7).

without reducing the desired signal.

We used stimulated downconversion (also known as difference-frequency generation) to determine the bandwidth of the 1550-nm photons that Bob receives (see Fig. 4.2a) [111]. In this process we use light from a narrowband, tunable distributed Bragg reflector (DBR) 1550-nm laser to stimulate 532-nm pump light to downconvert in the PPLN crystal. This process will have the same phase-matching conditions as the spontaneous parametric downconversion process used to generate the photon pairs in our experiment. However, since both the 532-nm pump and the DBR laser used to stimulate the downconversion are very narrowband, it is possible to stimulate downconversion in a very narrow portion of the phase-matching window. The relative intensity of the downconversion process in this region can be determined by measuring the ~ 810 -nm light created in this process. For perfect phase-matching (i.e., $\Delta k \equiv k_{532} - k_{810} - k_{1550} = 0$, where k_λ represents the wavevector of wavelength λ)³ the intensity of the 810-nm downconversion will be [112]:

$$P_{810} \propto P_{1550} \sinh^2 kL, \quad (4.3)$$

where $k = \sqrt{\frac{4d^2\omega_{532}^2\omega_{1550}^2}{k_{532}k_{1550}} P_{532}}$, P_λ and ω_λ respectively represent the optical power and angular frequency of wavelength λ , d represents the crystal's nonlinear coefficient, and L is the crystal length. However, as the frequency of the DBR laser is tuned, Δk will no longer be zero, and the strength of the process will be attenuated⁴. Therefore, by tuning the DBR laser frequency and measuring the power of the resulting 810-nm light, it is possible to determine the bandwidth over which the 1550-nm light satisfies phase-matching conditions. In this way, we determined the bandwidth of the 1550-nm spontaneous parametric downconversion light to be ~ 1.5 nm (see Fig. 4.2b). While this bandwidth is too large for satellite-based entanglement distribution (see Section 4.4.2), it can be further reduced using narrow band-pass filters, or a modified source⁵.

4.3.2 Quantum Message Encoding and Measurement

Having verified the quality of the two-photon hyperentangled state, we used these photons to implement SDT. In our implementation, the 1550-nm photon was sent to Bob and the 810-nm photon was sent to Charles (see Fig. 4.1). For this proof-of-principle experiment, the two temporal modes of Charles' photons were probabilistically separated using a non-polarizing beamsplitter (alternatively, the time bins can be separated

³Here we neglect effects due to the crystal poling period.

⁴While the (relatively) broadband spontaneous parametric downconversion will still be present in the measurement described here, the stimulated downconversion light can be made several orders of magnitude brighter than the spontaneous background by tuning the ratio of the pump and DBR lasers. This is because the spontaneous process is stimulated by the vacuum field rather than the DBR laser (as in the stimulated process).

⁵The downconversion bandwidth decreases inversely with crystal length (i.e. $\delta\lambda \sim 1/L$, where $\delta\lambda$ is the bandwidth and L is the crystal length) assuming a narrow-band pump.

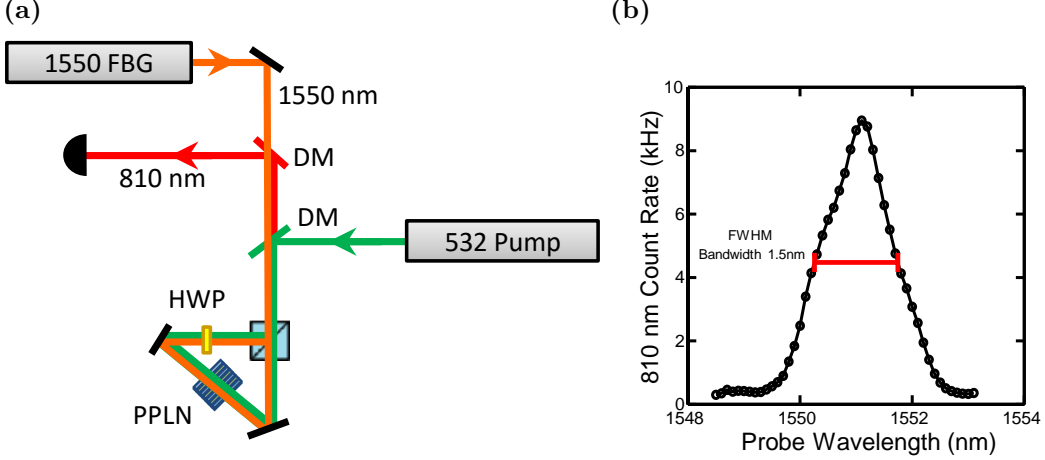


Figure 4.2: (a) Experimental layout used to measure the frequency bandwidth of the Sagnac downconversion source. The periodically poled lithium niobate (PPLN) crystals were simultaneously pumped with a narrowband 532-nm pump laser and a 1550-nm frequency-tunable fiber Bragg grating (FBG) laser (bandwidths of 65 GHz and 150 kHz, respectively). The 810-nm light created via stimulated emission is separated from the pump laser from the other two wavelengths using dichroic mirrors (DM) and detected with a single photon counter. (b) By tuning the frequency of the FBG laser (wavelength is factory calibrated to 0.2 nm of accuracy and 0.01 tuning repeatability) and measuring the resulting 810-nm photons, it was possible to measure the bandwidth of the 1550-nm downconversion.

using active switching as described in Section 2.3.3)⁶. Charles then applied phases to the polarization states of two different temporal modes using liquid crystals (see Appendix C), resulting in the target state:

$$|Ht_1\rangle + e^{i\phi_1}|Vt_1\rangle + e^{i\phi_2}|Ht_2\rangle + e^{i\phi_3}|Vt_2\rangle. \quad (4.4)$$

The photon was sent to Alice, who made measurements in the following basis:

$$\begin{aligned} |a^\pm\rangle &\equiv \frac{1}{\sqrt{2}}(|Dt_1\rangle \pm |At_2\rangle) \\ |b^\pm\rangle &\equiv \frac{1}{\sqrt{2}}(|Dt_2\rangle \pm |At_1\rangle). \end{aligned} \quad (4.5)$$

If we write the total state of Alice and Bob's photon pair in terms of Alice's measurement, we have:

$$\begin{aligned} &\frac{1}{4}[|a^+\rangle (|Ht_1\rangle + e^{i\phi_1}|Vt_1\rangle + e^{i\phi_2}|Ht_2\rangle - e^{i\phi_3}|Vt_2\rangle) \\ &+ |a^-\rangle (|Ht_1\rangle + e^{i\phi_1}|Vt_1\rangle - e^{i\phi_2}|Ht_2\rangle + e^{i\phi_3}|Vt_2\rangle) \\ &+ |b^+\rangle (|Ht_1\rangle - e^{i\phi_1}|Vt_1\rangle + e^{i\phi_2}|Ht_2\rangle + e^{i\phi_3}|Vt_2\rangle) \\ &+ |b^-\rangle (-|Ht_1\rangle + e^{i\phi_1}|Vt_1\rangle + e^{i\phi_2}|Ht_2\rangle + e^{i\phi_3}|Vt_2\rangle)] \end{aligned} \quad (4.6)$$

⁶During the course of the measurement procedure, it is important for signal, idler, and pump Mach-Zehnder interferometers to be phase-locked to each other, as phase drift will cause error in the temporal state measurements (see Appendix G).

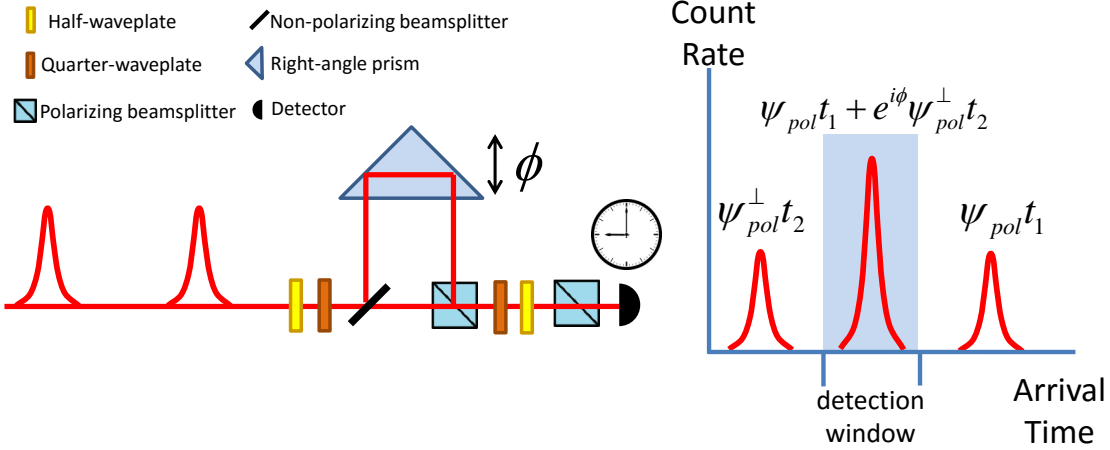


Figure 4.3: A non-polarizing beamsplitter is used as a passive temporal mode switch, but will sort the modes incorrectly 50% of the time. Alice and Bob can filter out counts that were sorted incorrectly by discarding all detection events that arrive outside the indicated detection window.

By inspection of Equation 4.6, we see that it is possible for Bob to correct his state with a unitary transformation based on the outcome of Alice's measurement, essentially telling him which of the 4 terms need a π -phase shift. For our proof-of-principle laboratory demonstration we did not perform feed-forward correction, but instead Bob performed a complete polarization and temporal-mode tomography on his photon by measuring in the following overcomplete measurement set⁷:

$$\begin{aligned}
 & \{H, V, D, A, R, L\} \otimes \{t_1, t_2\}, \\
 & Ht_1 + i^n Vt_2, \quad Ht_2 + i^n Vt_1, \\
 & Dt_1 + i^n At_2, \quad Dt_2 + i^n At_1, \\
 & Rt_1 + i^n Lt_2, \quad Rt_2 + i^n Lt_1,
 \end{aligned} \tag{4.7}$$

where $n = \{1, 2, 3, 4\}$. While the hybrid state (see Section 1.2.4) measurement bases might seem more complicated than bases which are separable in polarization and temporal mode, they have a distinct advantage in this system. First, it is possible to access all of the measurements listed above without adjusting the path length difference of Bob's interferometer or adjusting optical elements in the interferometer. This allows Bob to perform a complete tomography without disrupting his interferometer's phase stabilization.

To correctly measure in the bases listed in Equations 4.5 and 4.7, Alice's and Bob's measurements must be synced with the time basis in which the photons are created. This is because the passive switch (non-polarizing beamsplitter) used in Charles' and Bob's unbalanced interferometers only sorts each photon's

⁷Bob can completely characterize a general 2-qubit state with 16 measurements (or 4 measurements if the states are assumed to be equimodular), but a larger set of measurements will yield a more precise reconstruction with fewer detection events.

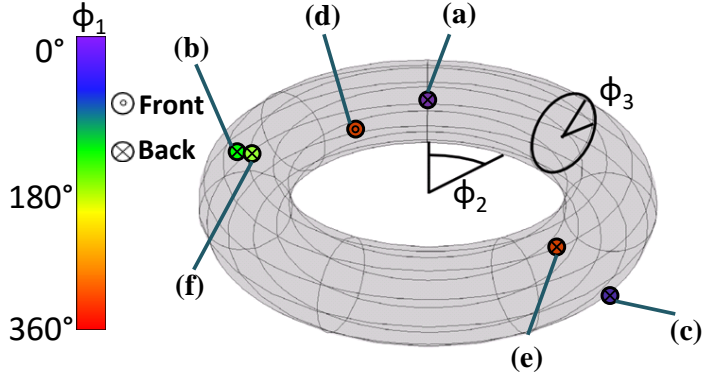


Figure 4.4: The equimodular polarization- and temporal-mode states transmitted using superdense teleportation. The phases ϕ_1 , ϕ_2 , and ϕ_3 parameterize the equimodular states as defined in Equation 4.4. The fidelity of each state with the target state and its density matrix are shown in Figure 4.5.

time modes into the correct interferometer arms half of the time. By using the pump pulses to synchronize their measurements, Alice and Bob could filter out events where the temporal modes were incorrectly sorted (see Fig. 4.3).

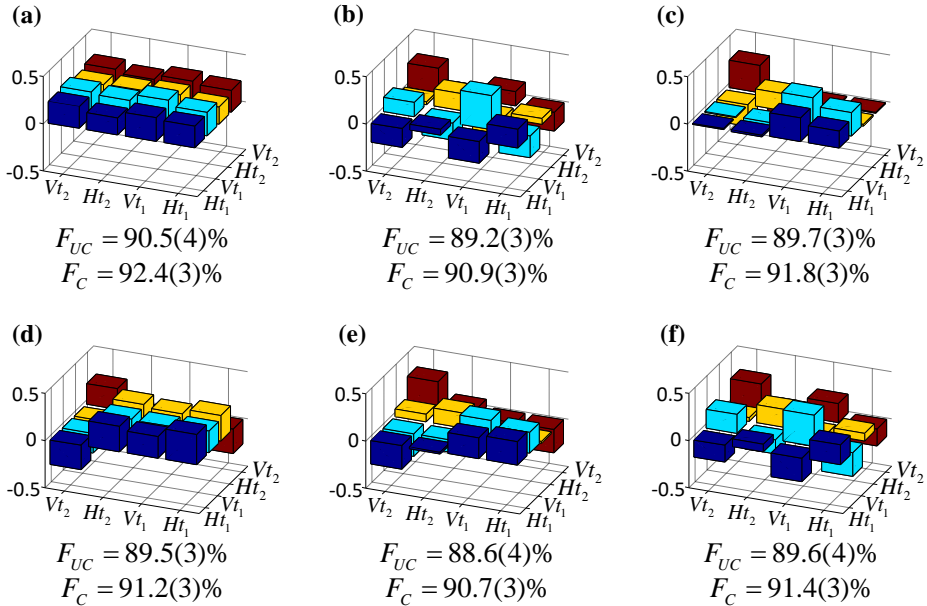


Figure 4.5: Reconstructed density matrices (real parts). For these measurements, Bob performed a tomographic reconstruction of the state that he received in coincidence with each of Alice's four measurement outcomes. The corrective unitary transformation was then numerically applied to each of the four reconstructed states and the density matrices were averaged. The fidelity of each state with the target state chosen by Charles (see Fig. 4.4, the matrix labels correspond to the respective point on the torus) was then calculated without accidental subtraction (F_{UC}) and with accidental subtraction (F_C).

Bob's measurements were then used to perform this quantum state reconstruction (see Appendix E). We were then able to determine which state Alice's measurement heralded on Bob's side (see Figs. 4.4 and 4.5).

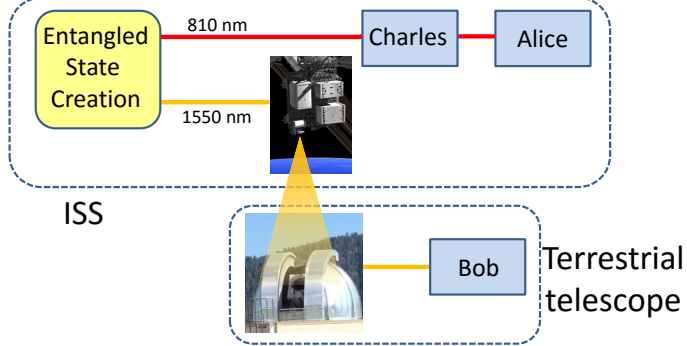


Figure 4.6: A schematic of a satellite-to-ground implementation of SDT. The entangled state creation, Charles’ phase rotations, and Alice’s measurement all take place on the satellite platform. The outcome of Alice’s measurement and the 1550-nm photon are then transmitted to the ground. Bob collects the 1550-nm photon with a terrestrial telescope and then corrects it based on Alice’s measurement outcome.

We see that these initial reconstructions show an average quantum state fidelity of 91%, which is over twice the classical limit of 44% (see Appendix B). We are currently performing quantum state reconstructions on more states and plan to eventually implement feed-forward transformations for Bob, so we can perform a full demonstration of SDT (see Section 4.4.4 for a description of how to implement feed-forward correction).

4.4 Adapting for Space Applications

4.4.1 Satellite Beacon

While our laboratory demonstration can be used to determine many of the fundamental challenges of implementing SDT and quantum key distribution using photons hyperentangled in polarization and temporal mode, many basic features need to be changed/added for adapting these techniques to use from the ISS. To implement the SDT protocol between the ISS and a terrestrial telescope, one (810-nm) photon of a two-photon state hyperentangled in polarization and temporal mode must be measured by Alice on the ISS, while the other (1550-nm) photon is transmitted to Bob on the ground (see Fig. 4.6). However, because the ISS is orbiting the Earth at ~ 7 km/s, several error sources are introduced to the polarization and temporal states of the 1550-nm photon. In addition, SDT requires that the results of the measurements on the 810-nm photons be communicated to the ground receiver. Bright beacon beams⁸ will serve as a feedback signal to correct the different sources of error that arise in transit from the ISS to the ground, and as a classical communication channel required by the SDT protocol. Strategies on how to accomplish these tasks are listed below.

⁸While it is possible to have a *single* beacon beam provide all of the tasks listed in this section, encoding and decoding the optical signals might be simplified if two or more frequency-multiplexed beacons are used.

Time Gating

As discussed in Section 4.3.2, it is necessary to synchronize Alice’s and Bob’s measurements with the time-bin basis in which the downconversion photons are created. Just as in the laboratory demonstration, this may be accomplished by syncing Alice’s and Bob’s measurements with the pump pulses creating the photons. However, syncing with the pump is much more challenging for an ISS-to-Earth implementation, since Bob’s measurements take place far away from the pump laser. One way to accomplish this task is to use a beacon beam with the same temporal characteristics as the pump laser. The beacon pulse arrival can be measured with a fast photodiode and then used as a fiducial time stamp to mark when the 1550-nm photon should arrive.

The ground receiver can also use this time stamp to distinguish the 1550-nm photon transmitted from the ISS from background light. Because Bob knows when the photon will arrive to within the jitter of his detection system (τ), he can discard all photon events outside this window⁹. The amount that windowing can filter out background is $\frac{1}{\tau f_L}$, where f_L is the pump laser repetition rate, e.g., if $f_L = 80$ MHz and $\tau = 500$ ps, then the background can be reduced by a factor of 25.

Interferometer Path-Length Balancing

As discussed in Section 4.3.1, temporal-mode entanglement used in the SDT protocol is created by splitting a single pump pulse into two time bins using an unbalanced Mach-Zehnder interferometer. To measure the temporal mode of the downconversion, there must be a reciprocal interferometer on the ground station that has the same path length difference and is phase stabilized to the pump interferometer on the ISS. However, if the entanglement source is moving relative to Bob, the relative phase between the two modes of the temporal qubit state will vary as a function of the time between the two modes and the “range-rate”, the rate than the distance between Bob and the ISS is changing (see Fig. 4.7). This Doppler-induced phase shift will change as the satellite passes overhead. Path length drift and the Doppler effect acting between the temporal modes of the downconversion will cause phase errors between two arms of the terrestrial interferometer. To compensate for these effects, the beacon can be transmitted through the ISS interferometer, creating pairs of pulses with the same time difference as the pump pulse pairs. After the beacon is transmitted to the ground receiver, the pulse pairs can be transmitted through the terrestrial interferometer and used with a pair of photodiodes (in the output ports of the ground interferometer) as a feedback system to phase stabilize the two interferometers (see Appendix G).

⁹Bob’s detection system jitter will depend on the rise-time of the photodiode used to detect the pump pulses, the jitter of his single-photon counters, and the jitter in the time-tagging hardware that is used to record when the counts arrive.

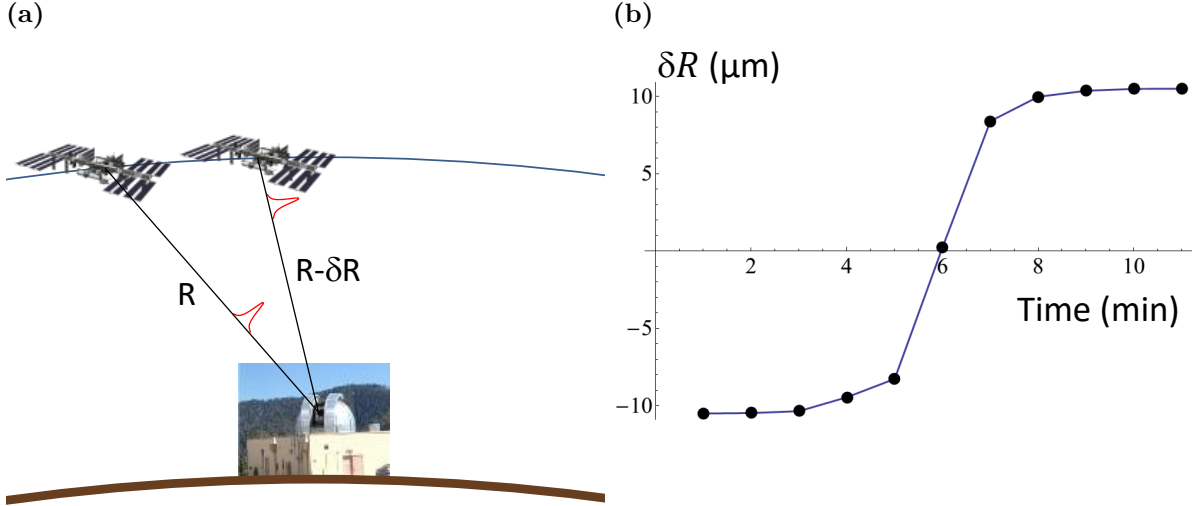


Figure 4.7: (a) The distance between a satellite and a ground receiver changes rapidly as the satellite passes overhead (at $\sim 7\text{ km/s}$). This movement will impart a Doppler shift between the two time bins of Bob’s photon. As the satellite passes overhead, the change in range, or range-rate, will vary and will result in a time-varying phase shift between the two time bins. (b) The interferometer displacement required to correct for the Doppler shift resulting from ISS movement. This plot was calculated from range-rate data for a nearly overhead pass of the ISS, measured by NASA’s Optical Communications Telescope Laboratory on Table Mountain near the Jet Propulsion Laboratory.

To demonstrate this functionality that the beacon must provide, we implemented a tabletop demonstration of interferometer path-length balancing. As discussed above, transmitting temporal-mode qubits between parties in relative motion can introduce changing phase shifts between the two temporal modes used to encode the qubit. To adapt our experimental setup for a satellite-to-Earth quantum communication protocol, this phase shift must be compensated. We have simulated this phase shift on a classical input state (an attenuated 1550-nm pulsed laser source) (see Fig. 4.8a) and demonstrated that it is possible to correct this shift by stabilizing an unbalanced interferometer (used as a temporal-mode analyzer) with respect to the output of a 1064-nm “beacon beam” (see Fig. 4.8b). This technique not only corrects temporal qubit phase changes due to the relative motion of the satellite, but also corrects shifts due to relative drift of the two interferometers to within 1° , allowing for reliable temporal qubit encoding and analysis.

Polarization Compensation

To correctly interpret measurements made on the polarization state of the 1550-nm downconversion photons, it is necessary to have complete knowledge of how the communication channel from the ISS to the terrestrial receiver (including telescopes, fibers, and pointing optics) affects polarization. This is a challenging task,

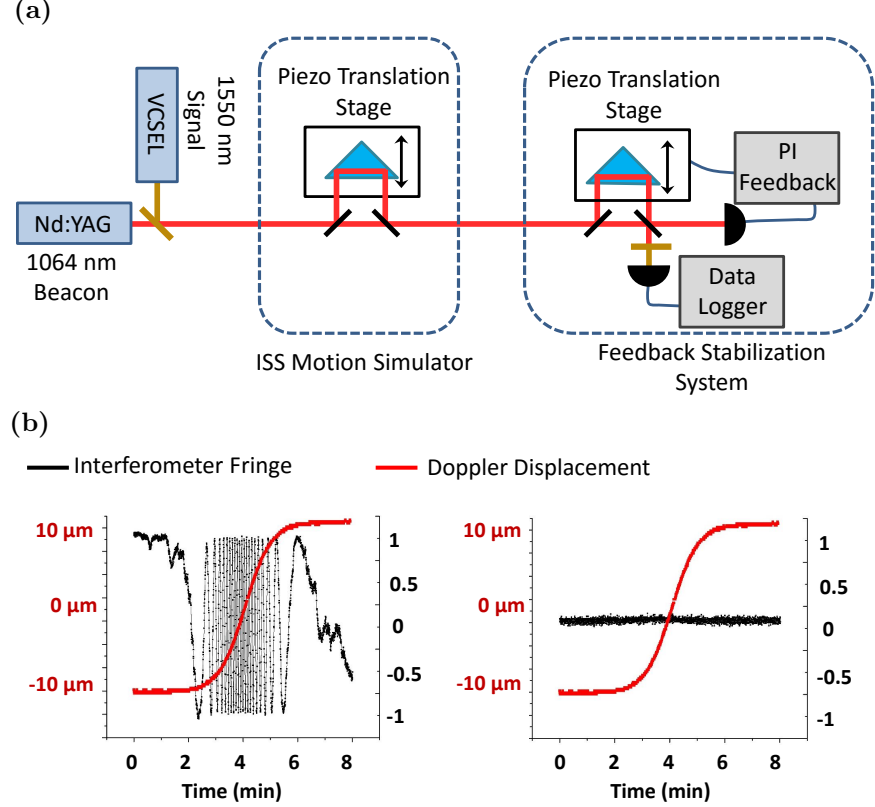


Figure 4.8: (a) An experimental demonstration of a beacon stabilization system. The 1550-nm signal beam is combined with a 1064-nm beacon beam and sent through an unbalanced interferometer. The path-length of this first interferometer was changed using a piezo actuator to simulate the Doppler shift arising from ISS movement (see Fig. 4.7). The two beams were then transmitted through a second interferometer. The power of the beacon beam was then used as feedback to adjust the path-length of the interferometer by adjusting the voltage on a piezo-electric actuator. The 1550-nm light was separated from the 1064-nm beacon using a bandpass filter and measured with a power meter to monitor the phase. (b) The 1550-nm light experiences rapid power fluctuations when the stabilization is deactivated (left) but is held constant (to within 1° of phase) when the stabilization is active (right).

since the channel changes as the ISS passes overhead. Furthermore, the path that the ISS traces as it passes overhead will vary from pass to pass, so the channel might change dramatically from pass to pass as well. One way to monitor these changes is to use the beacon beam to characterize the polarization effects of the channel in real-time. However, characterizing a quantum channel requires more than one polarization input (see Chapter 5.2). If the channel is assumed to be unitary, it will be necessary to transmit at least two different polarization states through the ISS-to-ground communication channel and perform a tomography on the two resulting states. In addition, the beacon must be a different wavelength than the 1550-nm downconversion photon (to keep Bob from confusing the two in his measurements) possibly with a different polarization transformation for each. Therefore, it will be necessary to relate these two transformations for the beacon to be used as a feedback signal to correct the polarization rotations on the 1550-nm downconversion photons,

e.g., by including additional waveplates or liquid crystals after the receiver optics.

Alternately, it might be easier to compensate for polarization rotation error with a detailed look-up table. Because the ISS trajectory must already be tracked very precisely in order for a ground receiver to establish a communication link, the configurations of all the mirrors used for beam steering will also be tracked. Since these mirrors are the only dynamically changing elements in the beam path, the polarization rotation can be monitored by making a look-up table of how the mirrors affect polarization for every possible configuration¹⁰.

Classical Communication Channel

In addition to the three channel-monitoring tasks listed above, the beacon(s) should also convey information regarding the outcomes of measurements made on the 810-nm downconversion measured on the ISS. To perform this task, every time an 810-nm photon is measured on the ISS, a 2-bit message (corresponding to one of the 4 possible measurement outcomes) must be transmitted to the ground receiver. By correlating these measurement outcomes with the measurement results of the 1550-nm photons, it is possible for Bob to either tomographically reconstruct the quantum state that each of Alice's measurements herald (as was done in our laboratory demonstration) or perform feed-forward correction on the quantum state (see Section 4.4.4). In the latter case, the classical information must be sent with minimal latency, as the 1550-nm photon will need to be delayed until the classical message is received and processed, and the appropriate transformation is applied.

4.4.2 Downconversion Link Analysis

In addition to monitoring how the ISS-to-ground channel affects state of Bob's photons, it is important to accurately characterize the efficiency of the data link. This is because Bob needs to receive and measure enough photons to characterize his quantum state, but the number of usable photon pairs created in the downconversion process is severely limited by photon number statistics: if the pump beam is too bright, then multiple downconversion pairs will be created in a single laser pulse, and Alice and Bob will not be able to reliably correlate their measurement results (i.e., Alice and Bob have no way of ensuring the photons that each of them measure originated from the same entangled pair). The maximum rate of photon pair production is thus highly dependent on the pump pulse repetition rate, f_{RR} (e.g., to limit multi-pair noise to $\sim 1\%$, the downconversion pair rate should be limited to $\sim 0.02f_{RR}$, i.e., only ~ 1 in 50 pulses should create a pair). Because of this limitation, either relatively high collection efficiency or a long measurement time is

¹⁰The rotational orientation of the ISS with respect to the ground station can also vary; however, this can be tracked visually and compensated as well.

required to characterize Bob’s state. Since the measurement time is constrained by the orbit of the ISS¹¹, the photon collection must be optimized to ensure a sufficient number of entangled photon pairs are measured. We have identified three main aspects of this implementation which need to be studied to determine the most practical ways to optimize collection efficiency.

Beam Pointing Analysis

For a photon transmitted from the ISS to be measured by a terrestrial receiver, it must first be pointed at the receiver’s collection optics. This is an especially challenging task for two main reasons. First, the ISS is traveling at > 7 km/s as it passes overhead at an elevation of > 300 km. Since the collection optics and single-photon detectors are very small in comparison, precise pointing is required. Second, atmospheric turbulence will influence the pointing of the beam in an unpredictable way. This turbulence will change the pointing on short time scales and will therefore require a fast response in the pointing compensation system [113, 114].

Influence of Turbulence on Spatial Mode

In addition to affecting the pointing of the optical beam, turbulence can change the spatial distribution of photons. While changes in the spatial mode of the optical beam will not affect the quantum state that we are trying to measure (which is stored on the polarization and temporal modes of the photon), these changes can make measurements on this state more difficult. Specifically, because the arms of Bob’s Mach-Zehnder interferometer are different lengths, photons with different momenta (i.e., traveling at different angles) will experience a different phase when traveling through the interferometer. High-order spatial modes (resulting from strong turbulence) are composed of a superposition of many different momentum modes, and will therefore have poor interference visibility, greatly degrading Bob’s measurement quality. An easy way to fix this issue is to filter out all but the lowest-order spatial modes using either a single-mode fiber or a pinhole. However, if the spatial-mode changes are too large, then too many photons will be discarded by this filtering process for Bob to reconstruct the state. Bob could instead correct turbulence using adaptive optics [62], but such systems are very expensive.

Here we pursued an alternative approach, namely, using imaging optics to map the input spatial mode of both arms of Bob’s interferometer onto the output polarizing beamsplitter [115] (see Fig. 4.9). Specifically we use a 4-f imaging system, one in which two identical lenses separated by twice their focal length are used to create an image four focal lengths away from the object, in each arm of the interferometer of the tabletop

¹¹We work under the assumption that the entire state transmission and characterization—including the necessary signal acquisition—should be completed in a single pass of the ISS; otherwise, the long-term stability requirements increase substantially.

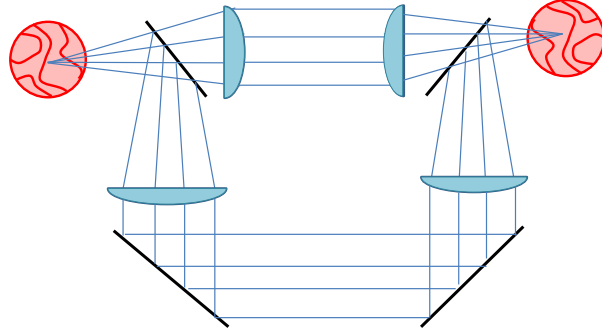


Figure 4.9: High-order spatial modes due to turbulence will disrupt the interference of an unbalanced interferometer, but this issue can be mitigated by putting a 4-f imaging system in both of the two interferometer arms.

demonstration described in Section 4.4.1. The way the imaging system affects incoming light rays can be modeled using the matrix method for optical ray tracing [116]:

$$\begin{array}{ccccccccc} \text{translation} & & \text{lens} & & \text{translation} & & \text{lens} & & \text{translation} \\ \left[\begin{matrix} 1 & f \\ 0 & 1 \end{matrix} \right] & & \left[\begin{matrix} 1 & 0 \\ -1/f & 1 \end{matrix} \right] & & \left[\begin{matrix} 1 & 2f \\ 0 & 1 \end{matrix} \right] & & \left[\begin{matrix} 1 & 0 \\ -1/f & 1 \end{matrix} \right] & & \left[\begin{matrix} 1 & f \\ 0 & 1 \end{matrix} \right] \\ & & & & & & & & \\ & & & & & & & & \\ & & & & & & & & \end{array} \begin{bmatrix} x \\ \theta \end{bmatrix} = \begin{bmatrix} -x \\ -\theta \end{bmatrix}, \quad (4.8)$$

where x and θ are the position and angle of the ray with respect to the central axis and f is the focal length of the two lenses. It can be observed from this equation that the imaging acts as the identity on input rays except for an image inversion¹². We have implemented imaging systems in the long and short arms of our tabletop beacon demonstration to show that multi-mode beams can still interfere with high visibility. A piezo mount was used to simulate turbulence-induced pointing changes in Bob’s interferometer. Without imaging, the interferometer showed significant k-vector-dependent phase shifts; when 4-f imaging was placed in the interferometer, these oscillations were reduced to below the noise level of the measurement. Additionally, we demonstrated interference when the spatial-mode input into Bob’s interferometer was scrambled with a multi-mode fiber. Without imaging no interference could be observed, but when the imaging system was aligned, we obtained a visibility of 93(3)%. The visibility is currently limited by the precision of the alignment of the optical imaging system in the short interferometer arm; future experiments will allow for better control of these lenses.

Spatial-mode turbulence can also affect the coupling efficiency of the downconversion photons into Bob’s detector. The time-dependent measurement collection efficiency caused by this effect, known as scintillation

¹²This inversion is the reason that an imaging system is needed in both interferometer arms. By using an imaging system in both interferometers, both images are inverted, and it is possible to match the optical distribution of both interferometer arms on the beamsplitter.

[117], can add significant error to Bob’s tomography measurements if left uncorrected. For example, if the degree of scintillation changes over the course of his tomography measurements, Bob might underestimate the projection probability of a particular measurement setting. This will in turn lead to an erroneous tomography reconstruction. However, Bob can monitor the coupling efficiency by making a complete set of orthogonal measurements for each setting (i.e., $\sum_i^4 |\psi_{i,j}\rangle\langle\psi_{i,j}| = j\mathbf{I}$, where $\psi_{i,j}$ represents the state that Bob’s i^{th} detector projects into for his j^{th} measurement setting). In this way Bob can monitor and compensate for intensity fluctuations in his measurements [118].

Preliminary Link Efficiency Calculations and Background Measurements

While the effects of turbulence can be partially mitigated with accurate beam pointing and imaging, it is much more difficult to correct for optical beam truncation due to diffraction. As an optical beam propagates from the ISS to a ground receiver, the beam will expand due to diffraction ($w(d) \approx \frac{\lambda d}{\pi w_0}$, where λ is the wavelength of the laser and $w(z)$ is the beam waist at a distance d from the beam waist, w_0)¹³. This expanded beam will be truncated by the aperture of the terrestrial telescope. It is necessary to quantify how truncation will influence the collection efficiency during a typical pass of the ISS over the terrestrial receiver. This effect will be the largest source of loss, setting a baseline of the highest possible collection efficiency, and will be important in any cost/benefit analysis of strategies to compensate other forms of loss. Truncation loss will also help determine the time window over which it is practical to perform measurements, known as the link time. The truncation loss will be lowest when the ISS is directly overhead (i.e., when it is closest) and will increase as it is lower on the horizon (when it is farther away). If the ISS is too far from the ground receiver, then the signal collected by the ground receiver will be comparable to the noise counts due to background events.

Preliminary link efficiency calculations have been performed by Abhijit Biswas at JPL for a 1-m telescope at the Optical Communications Telescope Laboratory collecting 1550-nm light from a (hypothetical) 20-cm telescope located on the ISS during a 50-s link for an ISS pass that is nearly overhead (ranges from 415–500 km). This calculation includes atmospheric transmission, optical truncation losses, transmitter and receiver losses (assumed to be 3 and 5 dB respectively), and beam pointing errors (assumed to be ~ 3 microradians, giving ~ 1.3 dB loss). Seeing conditions are assumed to be good. Given these assumptions, Bob’s downconversion photons can be focused onto a $62.5 - \mu\text{m}$ diameter detector with a collection efficiency of 0.24% to 0.35%. This high loss, combined with the short link time and the fact that the downconversion rate is limited, severely constrains the number of photons available to Bob to perform his tomography

¹³Here we have neglected beam expansion due to turbulence; a full calculation should include this effect.

(required to confirm that he received the correct state).

Noise from background sources (e.g., star light, sunlight reflected off the moon, and artificial light scattered off the atmosphere) are also a problem, and could overwhelm the downconversion photons. To reduce background noise, filtering techniques, such as spectral filtering and time gating, must be used. Currently, we have only very preliminary background count estimations. These estimations come from a background light measurement made by Abhijit Biswas of JPL made on August 27, 2015 at Table Mountain using a New Focus Model 2153 IR Femtowatt PIN detector¹⁴. From this measurement we roughly estimate background photon fluxes of approximately 1300 counts/s/nm for background light in a 100-nm band centered on 1550 nm. More precise measurements will be made in the future, but these estimates allow us to make preliminary assessments of how much background influences tomographic reconstruction.

Background noise can also arise from single-photon detector dark counts. One way to greatly reduce detector dark counts for Bob’s terrestrial measurement is to use WSi superconducting nanowire single-photon counters [119]. These detectors have sub-Hz intrinsic dark count rates, and so will not significantly contribute to noise in the coincidence measurements. While using these detectors will greatly reduce Bob’s background, it is unlikely that Alice will be able to use them for her measurements on the ISS, since nanowire detectors operate at very low temperatures (~ 1 K) and require a large, high-power cooling system. Instead, Alice can use relatively compact avalanche photodiodes for her measurement. While these detectors have a higher dark count rate (typically around 50-500 Hz), Alice’s measurements are much less sensitive to noise since her downconversion collection efficiency will be much higher than Bob’s. Unfortunately, avalanche photodiodes are quite sensitive to radiation [120, 121], and their dark count rate will increase the longer they are exposed to high levels of radiation in orbit. If the dark count rates increase to the point where they begin to become comparable with Alice’s downconversion collection rate, the increase in noise will begin to significantly degrade Alice’s signal. Based on these considerations, the nominal useable lifetime of Alice detectors will be only a few months (depending on shielding and orbit details). However, in collaboration with Professors Thomas Jennewein and Vadim Makarov at the Institute for Quantum Computing in Waterloo, ON, we were able to demonstrate that this lifetime could be extended by as much as a factor of 9, using a process known as optical annealing (see Appendix F). Research on this topic is currently ongoing, but the encouraging preliminary results suggest that mission lifetimes in excess of a year may be possible.

¹⁴These measurements were made at $\sim 90^\circ$ from the (nearly full) Moon and were consistent with MODTRAN models.

Tomography Budget

Given the constraints on downconversion rate, link efficiency, and background, we can begin to calculate how well Bob will be able to tomographically reconstruct the photon state that he receives. If we assume an experimental configuration where a 100-MHz repetition rate laser is used to generate downconversion photon pairs at a rate of 2 MHz, we estimate that we will be able to achieve a final coincidence count rate of around 40 Hz, for a total of 2000 coincidence events during the 50-s link described above. At this downconversion rate, approximately 20 false coincidences, known as accidental coincidences, should be expected over the course of the link due to double downconversion events. Additionally, if the 1550-nm downconversion is collected through a 0.2-nm bandpass filter, then Bob’s background noise will contribute $\sim 5 - 10$ accidentals (assuming a coincidence window of 500 ps, a 50% collection efficiency for Alice’s measurement, and 2-MHz downconversion pair rate).

We have performed initial simulations to estimate how many coincidence counts Alice and Bob need to measure for Bob to reconstruct his state. For these simulations, we assume that Bob can adjust his settings quickly and uses 36-measurement maximum likelihood state estimation for the reconstruction (see Appendix E). From these rough simulation, we estimate that only ~ 250 counts are needed to reconstruct the state accurately enough for Bob to statistically beat the 44% classical teleportation limit (see Appendix B). Therefore, we estimate that Bob will have sufficient photons to accurately reconstruct his state. However, more sophisticated state reconstruction simulations using Bayesian state estimation with accurate noise models are needed to know what level of reconstruction precision can be expected.

4.4.3 Hyperentanglement Source Miniaturization

A key challenge of performing quantum communication protocols from orbit is the design and implementation of a suitable source of entangled photons. While the source used in our tabletop experiment can produce high-quality hyperentangled photon pairs, its large footprint and relatively low stability prevent it from being directly adaptable to satellite based quantum communication. Furthermore, footprint limitations prohibit the use of most types of traditional bulk-crystal entanglement sources. Alternatively, recent advances in waveguide downconversion sources promise compact, high-brightness, narrow-band photon pair sources [122]. However, since such sources have only been designed recently, a comprehensive set of entangled source benchmarks still needs to be established. We have been working with a waveguide manufacturer (AdvR) to design and characterize a custom waveguide entanglement source suitable for our SDT implementation from the ISS.

Waveguide sources use periodic poling (see Section 1.3.1) to tune the properties of the output downcon-

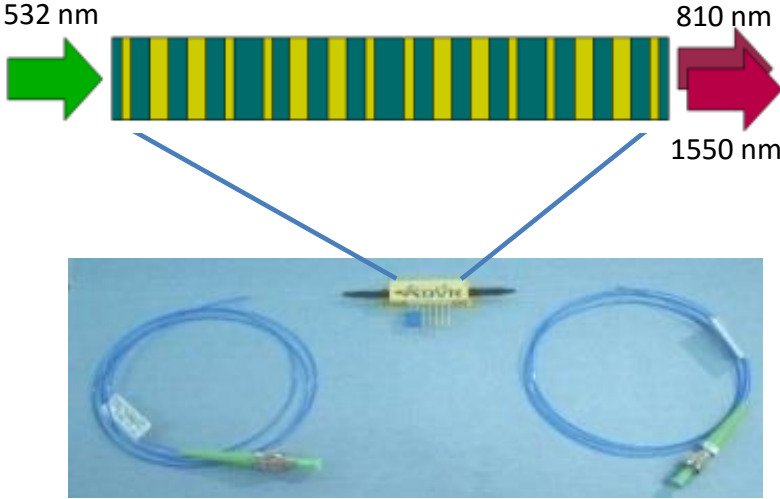


Figure 4.10: A waveguide entanglement source is much more compact than the bulk optics source used in the laboratory demonstration. By incorporating two different poling periods in the nonlinear crystal wave-guide, two different downconversion processes can be phase-matched over the length of the downconversion crystal, allowing entanglement generation with a single crystal waveguide.

version photons. By changing the poling period, it is possible to tune output downconversion wavelengths (subject to energy conservation) as well as the polarization of the output photons. For example, one choice of poling period allows the process ($H_{532} \rightarrow H_{810}V_{1550}$), while a different poling period allows the process ($H_{532} \rightarrow V_{810}H_{1550}$). By combining both of these two poling periods on one crystal, it is possible to produce the entangled state: $\frac{1}{\sqrt{2}}(H_{810}V_{1550} + V_{810}H_{1550})$. Since the entire entangled state generation takes place in a single crystal waveguide (see Fig. 4.10), this source is much more compact than the Sagnac interferometer entanglement source currently used in our laboratory SDT demonstration. Furthermore, the output of the waveguide source is coupled into single-mode optical fibers directly from the crystal, which reduces the space needed for downconversion collection.

While waveguide sources offer many advantages over bulk entanglement sources, the properties of their output entangled state cannot be tuned as freely (once manufactured) as many bulk-crystal sources. For example, the interaction strength for the two poling periods can be slightly different, causing a reduction in the entanglement of the output photons which cannot be easily corrected. Additionally, small variations in the poling period in either of the two regions can affect the frequency and bandwidth of the downconversion photons. If the two poling period regions produce photon pairs with different frequencies and/or bandwidths, the entanglement of the output photons will also be degraded (as the spectral information will label where a given pair originated). However, by adequately controlling the poling period, poling period region length, and crystal temperature, it should be possible to use waveguides to create high-quality entangled photons.

To select optimal waveguide parameters, it is necessary to have a method of measuring the quality of the output entangled photons. This can be accomplished using the tomography system in the current tabletop setup. In fact, because the waveguide's source is fiber coupled, it will be possible to characterize it without disrupting the Sagnac source. Further measurements of the bandwidth and central frequency of the waveguide entanglement source may be performed using difference-frequency generation. This may be accomplished in the same experimental setup, by using a tunable narrow-band 1550-nm laser source to stimulate downconversion (see Section 4.3.1). Information from these measurements will allow AdvR to further optimize the waveguide source for the final SDT implementation on the ISS.

4.4.4 Modifications for Feed-Forward Operation

For Bob to recover the same state that Charles chose, Bob must make a correction on his state based on Alice's measurement. To do this, Bob must store his photon until he learns the outcome of Alice's measurement, and he must also be able to apply the corrective transformation as the photon leaves storage. To practically implement this feed-forward operation, the experiment needs the following: 1. Real-time communication of Alice's measurement results from the ISS to Bob; 2. a quantum memory for Bob's photon (probably an optical delay line); 3. fast, corrective operations for Bob (via Pockels cells) (see Fig. 4.11). To correct his state, Bob stores his photon in the optical delay line until he receives and interprets Alice's message. The message informs Bob which term of his state he needs to apply a π -phase shift to. He can then apply the corrective transformation by applying voltages to his Pockels cells as the target time bin passes through the cell. However, depending on the type of Pockels cell used, Bob may not be able to apply a phase shift to the polarization of a time bin without influencing the orthogonal polarization of the same time bin. For example, a two-crystal, X-cut RTP Pockels cell applies equal and opposite phase shifts to the eigen-polarizations, making it impossible to apply a π -phase shift to just one term of Equation 4.6 (see Appendix C). This is most easily compensated by modifying the phase shifts that Charles applies to the entangled state. In particular, if Charles redefines $\phi_1 \rightarrow \phi_1 + \pi$, then Bob can correct his state by applying voltages to his Pockels cells based on Alice's measurement and transform his photon to the target state (see Table 4.1).

Each of the three items listed above pose experimental difficulties and some have interlinking requirements. For example, the length of time that Bob needs to store his photon depends on both the latency of Alice's measurement and communication link and on how fast Bob can interpret the signal and activate his Pockels cell once the message reaches him. The longer Bob stores his photon, the higher the chance it will be lost. Additionally, the number of photons that Bob can collect in a pass is already strictly limited

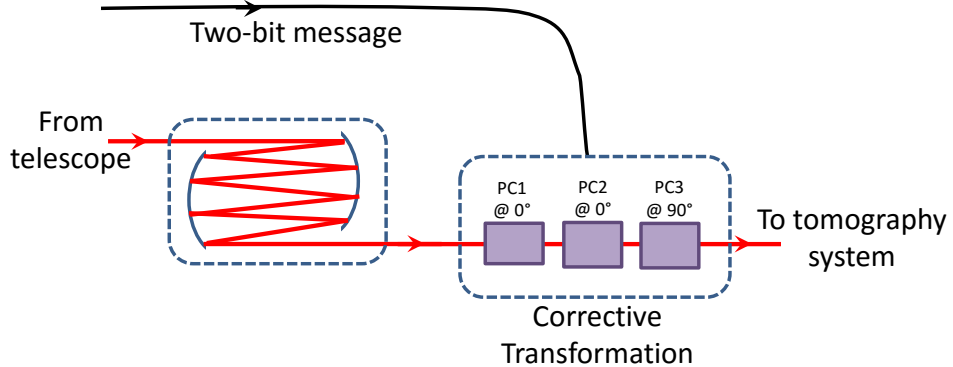


Figure 4.11: An experimental configuration for implementing feed-forward SDT. Bob stores his photon in an optical delay line until he receives Alice’s message. Based on this message, Bob applies voltages to his Pockels cells at specific times to rotate his photon to the target state (see Table 4.1.).

	PC1		PC2		PC3	
	t_1	t_2	t_1	t_2	t_1	t_2
a^+	on	on	on	off	off	on
a^-	off	off	off	off	off	off
b^+	off	off	on	off	off	on
b^-	on	on	off	off	off	off

Table 4.1: A list of which Pockels cells (PC) Bob activates in order to correct his state based on the outcome of Alice’s measurement. This table assumes the experimental configuration shown in Figure 4.11.

by both the number statistics of the source and the low channel link efficiency, so if Bob needs to store his photon for too long, he might not have enough photons to accurately reconstruct the state. To determine if feed-forward operation is experimentally feasible, we need to have detailed information about the temporal characteristics of each of the three elements listed above, as well as a loss estimate of the storage cavity.

4.5 Quantum Key Distribution

One of the primary reasons to demonstrate a quantum communication protocol that requires entanglement is that many other quantum protocols can be implemented using a similar experimental setup. In particular, even though quantum key distribution does not require entanglement, it can be readily demonstrated using almost identical experimental resources to those required for our proposed implementation of SDT. Using the same source of photons hyperentangled in polarization and arrival time, a four-dimensional entangled variant of BB84 can be implemented. In this protocol, two parties (Alice and Bob) want to generate a shared secret key which they can use as a one-time pad for encoding cryptographic messages [123]. However, any communication between Alice and Bob can, in principle, be intercepted by an eavesdropper (Eve). If Eve learns any information about Alice’s and Bob’s secret key, she can then gain some information about the

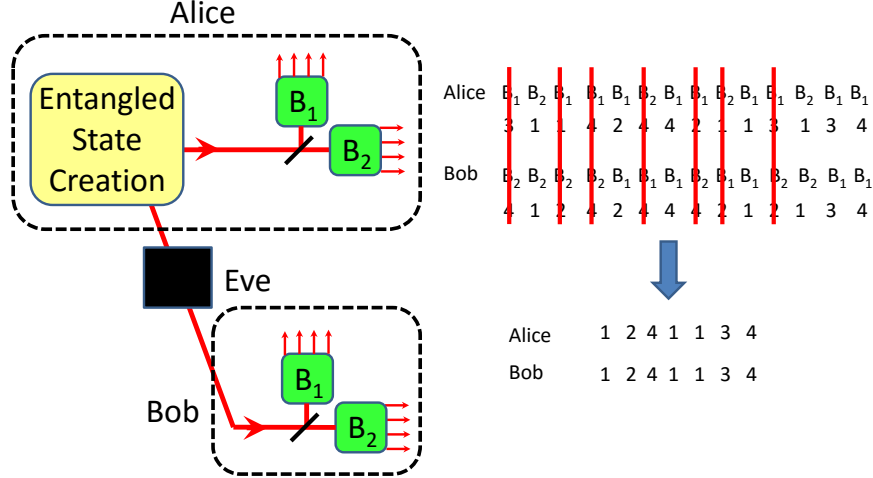


Figure 4.12: Schematic of a basic quantum key distribution setup. By using beamsplitters to randomly select a basis in which to measure their respective photons, Alice and Bob are each able to build up a string of random numbers. They then publically announce which bases they measured in. By keeping only events in which they measured in the same basis, Alice and Bob generate a shared random key. Error correction and privacy amplification must then be used to ensure that Alice’s and Bob’s key strings match and are private.

encrypted message. If Alice can generate entangled states of the form given by Equation 4.2 and send half of each state to Bob, they can use the nonlocal correlations to generate a shared cryptographic key that is provably secret from Eve (see Fig. 4.12). To do this, both Alice and Bob randomly measure their half of an entangled state in either basis B_1 or basis B_2 , where B_1 and B_2 are mutually unbiased to each other. After both Alice and Bob complete their measurement, they announce over a public channel which of the two bases they selected for each measurement, but not the specific measurement results. No matter which basis was selected, the individual outcomes for both Alice and Bob will be random¹⁵. However, if Alice and Bob both chose the same measurement basis (i.e., if they both chose B_1 or they both chose B_2), their random measurement results will also be perfectly correlated. On the other hand, if Alice and Bob chose different bases, their results will be uncorrelated, and they discard this event. By repeating this experiment many times, Alice and Bob build up a shared random key.

Before Alice and Bob can use their key to encode messages, they must ensure that Eve does not have any part of the secret key. In order for Eve to gain information about Alice and Bob’s key, she would need to perform measurements on the photons that Alice transmits to Bob. While there are many strategies that Eve could use to obtain information about Alice and Bob’s secret key [25], all of them will introduce errors into Bob’s measurement outcomes part of the time, since Eve has no way of knowing Alice’s and

¹⁵Each particle of a maximally entangled state will yield a completely random result when measured in any basis. All of the information of a maximally entangled state is encoded in the correlation between the two particles.

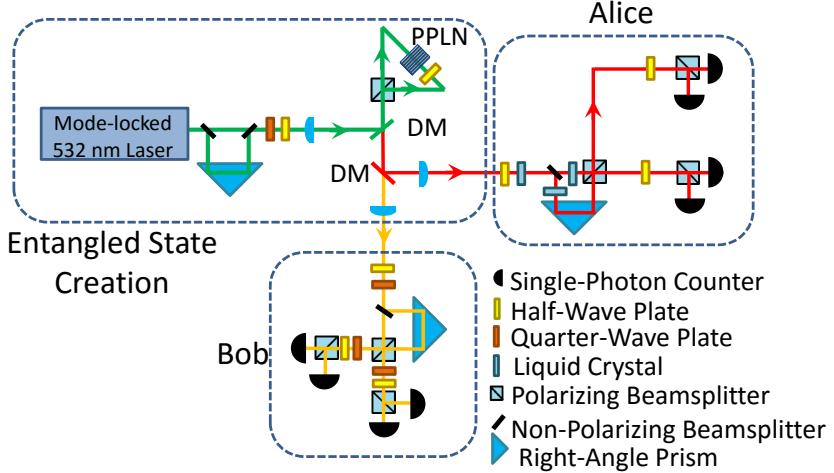


Figure 4.13: An experimental layout for hyperentanglement-based quantum key distribution. Quantum key distribution can be performed with the same optical layout as is used for SDT (see Fig. 4.1). To implement quantum key distribution with this setup, Alice and Bob randomly switch their measurement bases by adjusting liquid crystal and waveplate settings. After making measurements, Alice and Bob announce their measurement bases and use error correction [124] and privacy amplification to obtain a shared random key [125].

Bob’s measurement bases. Thus, Alice and Bob can detect whether Eve was making measurements on Bob’s photons by sacrificing part of their shared secret key to check for errors. In principle, if there is no eavesdropper, Alice and Bob’s secret key will be error-free; however, experimental imperfections will introduce error in the secret key. Because Alice and Bob use key errors to assess whether or not Eve is gaining information, any type of error must be treated as if it were introduced by Eve. After the error-rate of the key is determined, Alice and Bob fix the errors by creating a shorter, secure key using well-established methods for error correction [124] and privacy amplification [125].

While many traditional quantum key distribution techniques employ maximally entangled qubits as the quantum state that Alice and Bob use to generate their shared randomness, there are advantages to using the larger entangled state provided by hyperentangled photons [126]. Most notably, if the photons that Alice and Bob share are hyperentangled in polarization and temporal mode as described in the previous section, Alice and Bob obtain two bits of “raw” secret key every time they measure their photons in the same basis, instead of one bit as obtained using maximally entangled qubits.

4.5.1 Modifications for Quantum Key Distribution

Very little modification needs to be made to the experimental configuration described in the previous section to implement quantum key distribution. In particular, the entangled source and Bob’s measurement capabilities are identical for SDT and 4-dimensional quantum key distribution. However, we need to allow

Alice and Bob have the capability of switching between two mutually unbiased bases for their measurements (the state chooser Charles is combined with Alice's measurement in this protocol) (see Fig. 4.13). Alice can use her liquid crystals to randomly switch between the following two mutually unbiased bases:

$$\begin{aligned} B_1 &\equiv \{Dt_1 \pm At_2, At_1 \pm Dt_2\} \\ B_2 &\equiv \{Rt_1 \pm iLt_2, Lt_1 \pm iRt_2\}. \end{aligned} \tag{4.9}$$

Bob can also switch between these two bases by rotating waveplates; however it might be faster to use liquid crystals to switch between the two bases¹⁶. Alice and Bob can then use the quantum key distribution protocol described above to generate a shared string of secret random bits.

¹⁶Even in a satellite demonstration, Bob can exchange components in his optical setup easily, since his measurements take place on Earth. In contrast, it is unlikely that Alice will be able to make any modifications to her system, since her measurements take place on a satellite.

Chapter 5

Quantum Channel Characterization

Reproduced in part with permission from T.M. Graham, J.T. Barreiro, M. Mohseni, and P.G. Kwiat. Hyperentanglement-enabled Direct Characterization of Quantum Dynamics. *Physical Review Letters* 110(6). ©2013 American Physical Society.

5.1 Introduction

As scientists advance the frontiers of quantum information science and quantum computing by producing ever larger and more complex quantum systems, there has been an increased need for efficient methods of characterizing quantum states and processes. For example, quantum communication protocols often require knowledge of how the communication channel (e.g., free space or fiber) affects quantum states transmitted through it. Often times, the quantum process describing the channel (i.e., the way the channel changes an arbitrary input state) will change over time, so the process must be efficiently monitored in order for the quantum channel to be used effectively. One way to monitor the effect that a quantum channel has on quantum states is to perform measurements on the states after passing through the quantum channel. The information contained in a quantum state may be extracted using quantum state tomography, which is accomplished by making various measurements on multiple copies of the state, and then using these measurement outcomes to reconstruct the density matrix (see Appendix E). The information describing a quantum process is then extracted by probing the process with various quantum states and then making measurements on the output. This characterization, known as quantum process tomography (QPT), is generally more difficult than quantum state tomography because quantum processes are parameterized by quadratically more information than the states on which they operate. We present an experimental realization of an entanglement-enhanced QPT technique devised by Mohseni and Lidar [127], known as direct characterization of quantum dynamics (DCQD). DCQD has advantages over other QPT methods: it requires far fewer experimental settings than techniques which use only local probe states and measurements, and it requires less complicated measurements than techniques requiring a similar number of experimental configurations [128]. The many-body

interactions required by many other entanglement-enhanced process tomography techniques are difficult to implement with any current qubit technology, and physically *impossible* to implement deterministically with linear optics [129, 130, 131].

The biggest challenge in applying DCQD for optical qubits is performing the required full Bell-state measurement on each output state, which, as discussed in Section 2.1.2, is impossible using only linear optics in a restricted Hilbert space [48]. DCQD was implemented with photons using a probabilistic Bell-state measurement [132]; however, the lack of full Bell-state measurement meant that more measurements per experimental configuration were required, losing much of the DCQD advantage. It has been previously shown that it is possible to achieve full Bell-state measurement using quantum systems that are hyperentangled by using controlled-NOT (CNOT) logic gates between different degrees of freedom [133]. DCQD using CNOT gates between different degrees of freedom was demonstrated, but only with single-photon *hybrid*-entangled states (entanglement between different degrees of freedom of a single particle) [134]. Because hyperentangled probe states were not used, this technique is not scalable to multi-qubit processes that require two-photon Bell-state measurements to characterize (specifically single-photon multi-qubit processes)¹. Furthermore, the experiment has a classical interpretation and could have been performed using classical inputs. Deterministic Bell-state measurements may also be performed using many-body interactions [48]; unfortunately, because optical nonlinear effects are weak, it is impossible at this time to employ nonlinear techniques to perform deterministic Bell-state measurements on multi-photon states. This limitation is not present in other physical systems, such as ionic spin states. In fact, DCQD with deterministic Bell-state measurement using many-body interactions has concurrently been demonstrated by Nigg et al. [135].

Here we demonstrate DCQD using hyperentanglement-enabled deterministic Bell-state measurements and techniques that can readily be extended to characterize higher dimensional quantum processes. Specifically, we used photons simultaneously entangled in both polarization and orbital angular momentum to characterize several classes of single-qubit polarization quantum processes using DCQD with one-third the number of experimental configurations that were required using SQPT. After discussing the standard quantum process tomography (SQPT) methods for comparison, we describe the essential elements of DCQD. Next, we describe our experimental implementation of both SQPT and DCQD, before discussing possible extensions of the latter.

¹While single-photon two-qubit Bell-state measurements might still be used to measure two-photon processes acting on one qubit of each photon, the lack of two-photon Bell-state measurements prevents this technique from being scalable to multi-qubit processes acting on different degrees of freedom of a single photon, a desirable application of these techniques given the growing interest in multi-degree-of-freedom encoding.

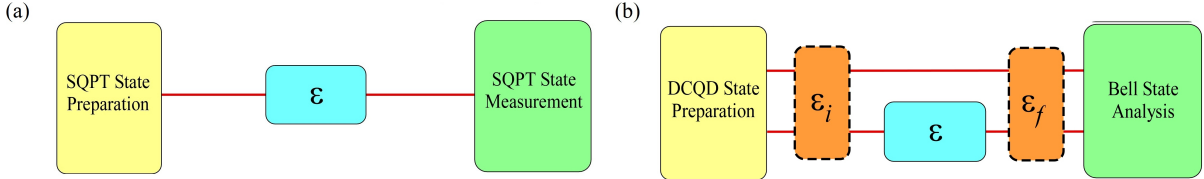


Figure 5.1: The basic measurement schemes for single-qubit processes ϵ using (a) SQPT and (b) DCQD . Though DCQD requires more complex input states and measurement settings than SQPT, it also requires three times fewer experimental configurations. The dotted boxes before and after the process in **b** represent errors in source preparation and analysis, here described by initial and final error processes (ϵ_i and ϵ_f).

5.2 Quantum Process Characterization

The information describing a quantum process may be completely parametrized by the χ -matrix, which is a representation of a super-operator that maps an input quantum state to an output quantum state; for a single qubit [136]:

$$\epsilon(\rho) = \sum_{m,n=0}^3 \chi_{mn} \sigma_m \rho \sigma_n, \quad (5.1)$$

where a quantum process, ϵ , acting on a quantum state, ρ , can be represented as sum of transformations made by Pauli matrices, σ_m , weighted by the elements of χ [136]. In SQPT, a quantum state tomography is performed on a complete set of input states (see Fig. 5.1(a)). SQPT has the advantage of requiring only simple input states and simple measurements. However, this technique requires 12^n experimental configurations to completely characterize a quantum process acting on n qubits [(4^n input states) \times (3^n measurement settings)], which rapidly becomes intractable as n increases².

Another type of QPT—ancilla-assisted process tomography (AAPT)—uses the nonlocal behavior of entangled qubits to decrease the number of necessary inputs to one. Here, the input qubits are entangled with an equal number of ancilla qubits [137]; by performing quantum state tomography on the total quantum state, it is possible to completely reconstruct the quantum process. In fact, by making “mutually unbiased basis measurements” or using “positive operator value measures” instead of simple “joint state measurements”, one can use AAPT to perform quantum state tomography and reconstruct the quantum process with far fewer experimental settings than are required by SQPT, or even DCQD [128, 129, 130, 131]. However, the complexity of the measurements required to perform these process tomography techniques increases as the number of qubits n increases, because they require many-body interactions.

Unlike SQPT and AAPT, DCQD can *directly* characterize a quantum process without quantum state tomography; the process is characterized by performing a full Bell-state measurement on a specific set of

²It is assumed that all outcomes of projective measurements may be detected (i.e., H&V—and D&A and L&R—can both be simultaneously measured).

partially entangled quantum states whose ancilla qubits have interacted with the quantum process (see Fig. 5.1(b)). Not only does the number of experimental settings required by this technique (4^n) scale better than SQPT (12^n), but the most complicated measurement required is a 2-qubit Bell-state measurement, no matter how complicated the process to be measured (i.e., even a 4-qubit process requires only pairwise Bell-state measurement). In fact, a judicious choice of states also allows one to minimize errors in the process estimation [138].

5.3 Experimental Implementation

5.3.1 Input State Creation

We used SQPT and DCQD to measure single-qubit quantum processes acting on polarization. The single- and two-photon polarization states necessary for each respective technique were produced using type I spontaneous parametric downconversion. Specifically, time-correlated 702-nm photon pairs were created by pumping a pair of β -barium borate (BBO) crystals (see Section 1.3.1 and ??). In the SQPT measurements, the idler photon heralded the presence of a horizontally polarized signal photon. Liquid crystals were then used to prepare the single photons into one of an over-complete set of probe states [139]: horizontal (H), vertical (V), diagonal (D), anti-diagonal (A), left circular (L), and right circular (R). After transmitting each input state through the process, an over-complete set of measurements was performed on each output state (in the same bases as above) using adjustable quarter- and half-waveplates before a polarizer. Though single-qubit quantum processes may be characterized using only 12 experimental configurations, we used 18 experimental configurations to minimize error in the SQPT data, since it was used as the reference for the DCQD measurements [140, 141].

Our implementation of deterministic DCQD requires hyperentangled input states. To create these states, we combined the twin-crystal polarization entanglement source with the orbital angular momentum entanglement source (see Sections 1.3.1 and 1.3.3) by pumping a pair of orthogonally oriented BBO crystals with a 351-nm Ar⁺ laser prepared in an equal superposition of horizontally and vertically polarized light, just as described in Section 3.3.1. By selecting ± 1 -order orbital angular momentum with holograms and single-mode fibers, we create the state:

$$\frac{1}{2}(|HH\rangle - |VV\rangle) \otimes (|lr\rangle + |rl\rangle), \quad (5.2)$$

where l and r represent right- and left-orbital angular momentum modes (OAM), respectively. Using a pump beam polarized at $\frac{\pi}{8}$ with respect to H, and manipulating the polarization of both signal and idler photons

using liquid crystals, it was possible to create the three additional input states required for DCQD:

$$\begin{aligned} \frac{1}{\sqrt{2}}(\cos \frac{\pi}{8}|HH\rangle - i \sin \frac{\pi}{8}|VV\rangle) \otimes (|lr\rangle + |rl\rangle) \\ \frac{1}{\sqrt{2}}(\cos \frac{\pi}{8}|DD\rangle - i \sin \frac{\pi}{8}|AA\rangle) \otimes (|r\rangle + |rl\rangle) \\ \frac{1}{\sqrt{2}}(\cos \frac{\pi}{8}|LL\rangle - i \sin \frac{\pi}{8}|RR\rangle) \otimes (|lr\rangle + |rl\rangle). \end{aligned} \quad (5.3)$$

Only the signal photon of each state was then propagated through the quantum process, after which we used hyperentanglement to allow us to perform a full polarization Bell-state measurement on the output states [142] (see Fig. 5.2 (a)).

5.3.2 Bell State Measurement

Hyperentanglement-enhanced Bell-state measurements, as described in Section 2.2.1, use coincidence detection of single-photon, two-qubit “hybrid-entangled” states to find unique signatures of polarization Bell states. To review, the key point to a full polarization Bell-state measurement is the fact that a hyperentangled polarization/spatial-mode Bell state may be written [142]

$$\begin{aligned} \Phi_{Spin}^{\pm} \otimes \Psi_{Orbit}^{+} &= \frac{1}{2}(\phi_1^+ \otimes \psi_2^{\pm} + \phi_1^- \otimes \psi_2^{\mp} \\ &\quad + \psi_1^+ \otimes \phi_2^{\pm} + \psi_1^- \otimes \phi_2^{\mp}) \\ \Psi_{Spin}^{\pm} \otimes \Psi_{Orbit}^{+} &= \frac{1}{2}(\pm \phi_1^+ \otimes \phi_2^{\pm} \mp \phi_1^- \otimes \phi_2^{\mp} \\ &\quad \pm \psi_1^+ \otimes \psi_2^{\pm} \mp \psi_1^- \otimes \psi_2^{\mp}), \end{aligned} \quad (5.4)$$

where Φ^{\pm} and Ψ^{\pm} represent the four two-photon Bell states for polarization (spin) and orbital angular momentum (orbit), and ϕ^{\pm} and ψ^{\pm} are the single-photon hybrid-Bell states for both signal (1) and idler (2) photons:

$$\begin{aligned} \psi^{\pm} &= (|Hl\rangle \pm |Vr\rangle)/\sqrt{2} \\ \phi^{\pm} &= (|Hr\rangle \pm |Vl\rangle)/\sqrt{2}. \end{aligned} \quad (5.5)$$

Thus, determining the single-photon hybrid-entangled state of each individual photon uniquely determines the two-photon hyperentangled state. The requisite operations were implemented by interfering the ± 1 -order diffracted outputs of a forked binary hologram on a polarizing beamsplitter (see Fig. 5.2(b)). These silver-halide emulsion holograms had $\sim 33\%$ diffraction efficiency into the first order and, when used with

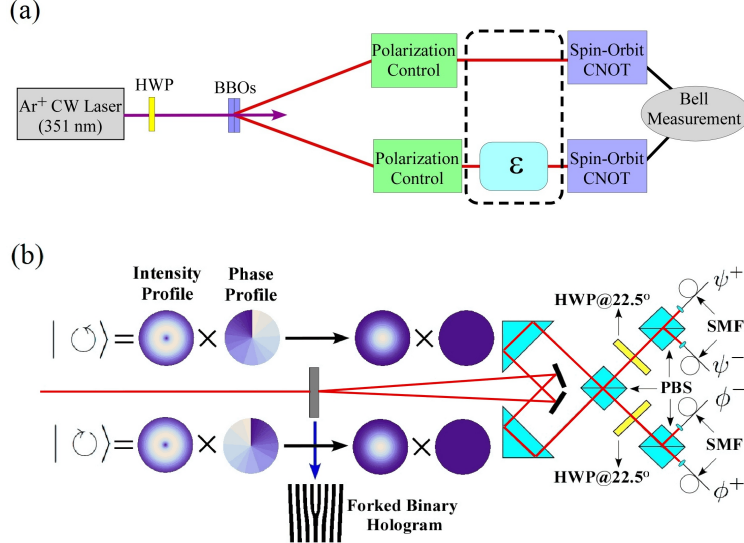


Figure 5.2: (a). Experimental setup used to perform DCQD on various single-photon quantum processes. A half-waveplate (HWP) tunes the pump polarization to generate photon pairs for SQPT or DCQD. The DCQD input states were prepared with liquid crystals (Polarization Control). (b) The spin-orbit CNOT gates, which were used to measure the four single-photon hybrid-entangled Bell states in Eq. 5.5. The outputs of a forked binary hologram are combined on a polarizing beamsplitter (PBS) and then spatially filtered with single-mode fiber (SMF).

single-mode fibers, have the dual property of both converting different orbital angular momentum beams into Gaussian beams travelling in different directions and filtering out all but the Gaussian spatial modes [133, 143]. Combined with polarizers and single-photon counters, the interferometers measure the single-photon Bell states (see Fig. 5.2). Thus, by detecting the outputs of each of these spin-orbit CNOT gates in coincidence, it was possible to perform a full polarization Bell-state measurement.

5.3.3 Experimental Results

We used DCQD to characterize several single-photon polarization processes. Pauli matrix rotation quantum processes were applied using half-waveplates, dephasing and depolarization processes were implemented using thick birefringent quartz plates [144], and the polarization quantum process was implemented with a sheet polarizer (see Fig. 5.3). Lastly, tunable partial polarization/dephasing processes were implemented by placing polarization/dephasing processes in the beam path for a fraction of the count time (and the identity process for the remainder).

The χ -matrices of each of the quantum processes were characterized using SQPT with 18 experimental configurations and DCQD with 4 experimental configurations. The χ -matrices were then reconstructed using maximum likelihood techniques [91] and compared using stabilized Jamiolkowski fidelity F_J , also known as

stabilized entanglement fidelity³. F_J was chosen over the other process fidelities because it is a stable metric which, in contrast to the more commonly used average process fidelity, can be used for all classes of quantum processes (including non-trace preserving processes) [145].

5.3.4 Error Compensation

Initial χ -matrices from the two methods showed less than desired agreement due to errors in the Bell-state measurement. It has been shown that errors introduced by imperfect DCQD state preparation and faulty Bell-state measurement can be decoupled from the quantum process data if both error maps are well characterized [138], but to characterize the relevant two-qubit error map requires two-qubit QPT (which in general requires quadratically more experimental configurations than single-qubit QPT). Fortunately, because single-qubit DCQD only requires four experimental configurations, only partial information of these error maps was required and was characterized using tomography. Preparation and measurement error maps cannot be completely characterized together because it is impossible to decouple the effects of two arbitrary error maps. For this reason, we characterized the two error maps independently from one another by performing a polarization state tomography on the source using high-fidelity separable projective measurements and then using the characterized source to characterize the Bell state measurement (see Section 5.4). After error correction, for identical processes, the overlap between the inferred process with SQPT and the one with DCQD was improved from a mean F_J of 89.2% to 96.0% (see Fig. 5.4). Even after compensating these error processes, the χ -matrices inferred with the two different characterization techniques are not statistically identical. This residual systematic error is due to time-dependent power fluctuations which are not corrected by this error reduction technique. However, simulations of DCQD measurements with the inclusion of these power fluctuations show agreement with experimental results (see Section 5.4).

5.3.5 Partial Process Characterization

It is possible to use DCQD techniques to measure significant process parameters without a complete characterization. For example, it is possible to measure both spin-lattice (T_1) and spin-spin (T_2) relaxation times using a single experimental setting [127, 146]. Though vital in characterizing the coherence of many quantum systems (atoms, ions, quantum dots, etc.), spin-lattice relaxation is not present in most photonic systems because photons do not interact strongly with thermodynamic reservoirs, nor do they decay to lower energy states. However, we simulated these processes by employing a combination of time-varying polarization

³ $F_J = \text{Tr} \left[\sqrt{\sqrt{[I \otimes \epsilon_1](\rho_\Phi)}[I \otimes \epsilon_2](\rho_\Phi)\sqrt{[I \otimes \epsilon_1](\rho_\Phi)}} \right]^2$, where quantum processes ϵ_1 and ϵ_2 act on one qubit of some two-qubit maximally entangled state, ρ_Φ , and the fidelity is taken between the outputs of the two processes.

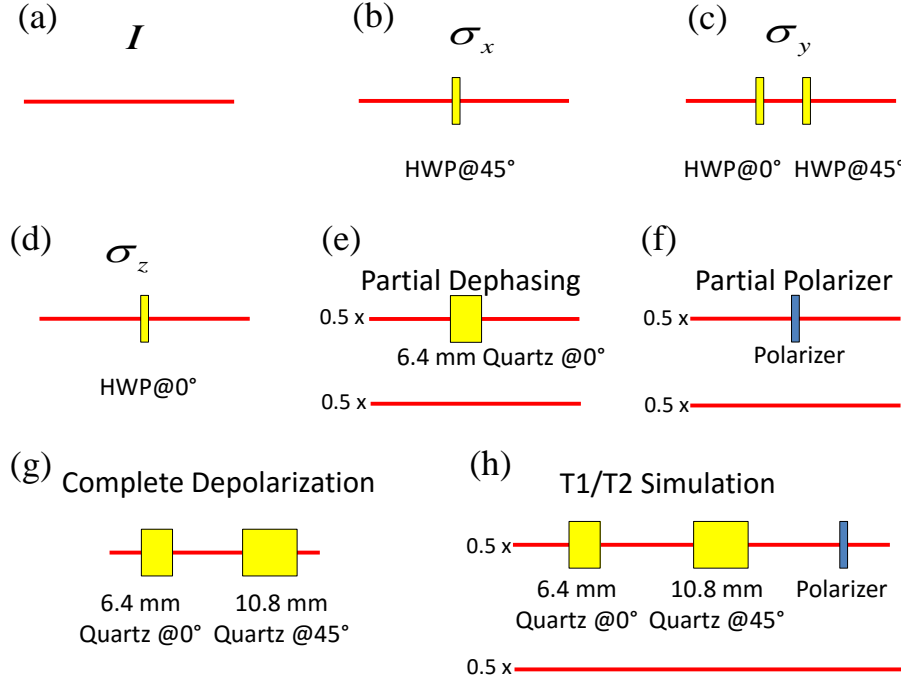


Figure 5.3: Experimental implementation of several quantum processes. (a) The identity quantum process was implemented by simply letting the beam propagate freely and (b-d) Pauli matrices were implemented using waveplates. (e) Partial dephasing was implemented by placing a thick quartz window in the beam half of the time and letting the beam propagate freely the other half. (f) A similar strategy was used to implement a partial polarization process by placing a polarizer in the beam path half the time and letting the beam propagate freely the other half. (g) A complete depolarization process was implemented using two quartz windows of different thickness to dephase in the H/V basis and then in the D/A basis. (h) A simulated T1/T2 process was implemented by combining the complete depolarization and polarization processes in the beam path half of the time and letting the beam propagate freely the other half.

processes. Specifically, photons were transmitted through a thick quartz plate and a polarizer part of the time and through empty space (the identity process) the remainder (see Fig. 5.3h). While the individual values of T_1 and T_2 have little physical significance in our optical simulation, the ratio of $R \equiv T_2 : T_1$ is a measure of how coherently states evolve in this process. This ratio was measured with SQPT (1.01 ± 0.03) using an over-complete set of 18 experimental settings, and with DCQD using a *single* experimental setting (0.99 ± 0.06). This process was also characterized with DCQD using all four experimental configurations that are required for complete process characterization (see Fig. 5.4h).

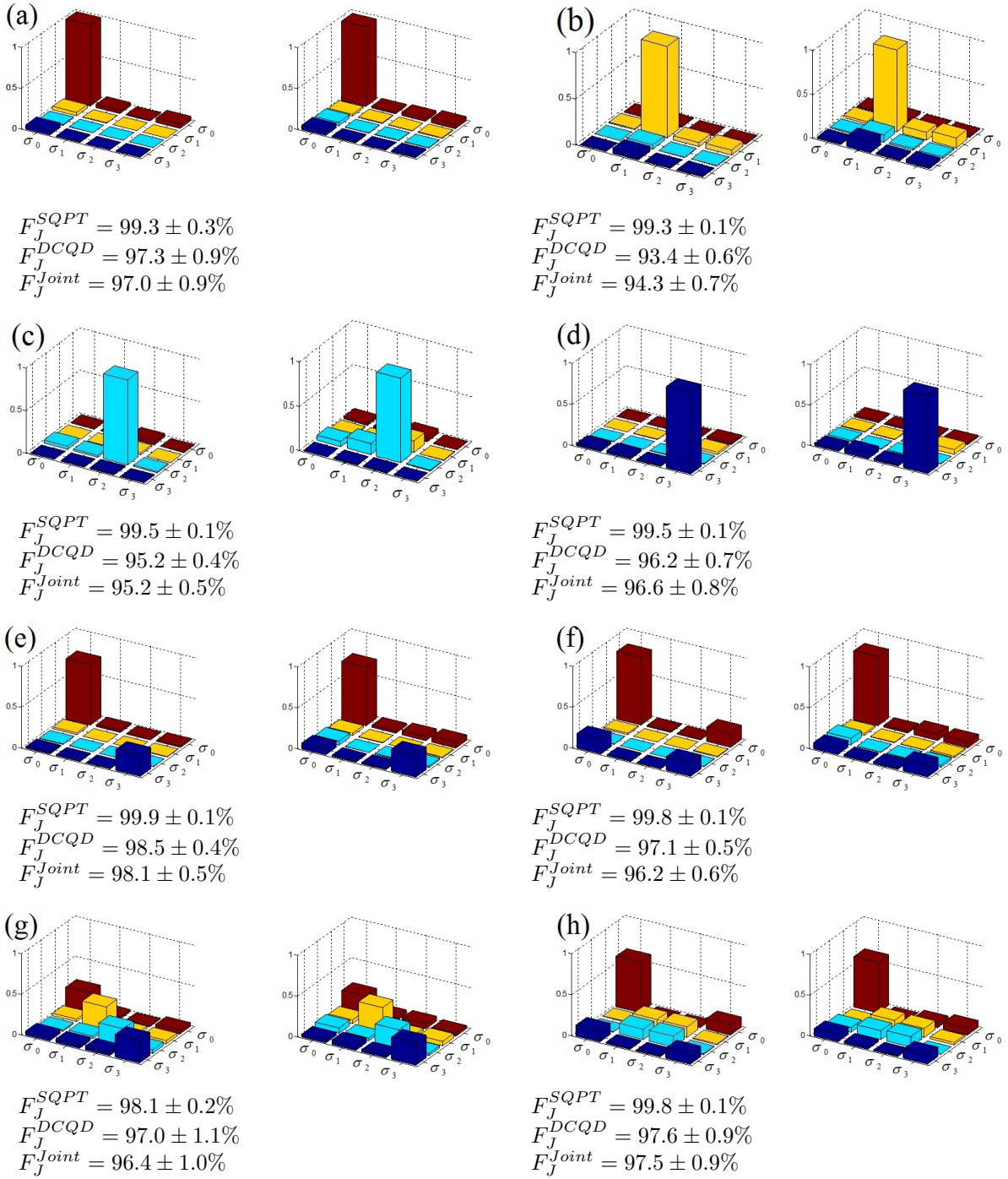


Figure 5.4: Reconstructed χ -matrices (absolute values of elements) from SQPT (left column) and DCQD (right column) measurements for the following: (a) identity, (b) σ_x rotation, (c) σ_y rotation, (d) σ_z rotation, (e) partial dephasing, (f) partial polarizer, (g) depolarization, (h) and simultaneous “spin-lattice” and “spin-spin relaxation”. The fidelities listed under each state compare the target process with the experimentally measured process using SQPT (F_J^{SQPT}), the target process with the experimentally measured processes using DCQD (F_J^{DCQD}), and the fidelity between experimentally measured processes using SQPT and DCQD (F_J^{Joint}). Uncertainties were calculated using Monte Carlo methods applied to Poissonian photon counting statistics.

Process	Tomography	Average Pump Power	Total Count Time	Total Counts
Identity	DCQD	400 mW	480 s	11134
	SQPT	600 mW	720 s	86809
σ_z	DCQD	500 mW	960 s	20991
	SQPT	600 mW	720 s	81481
Partial Dephasing	DCQD	400 mW	960 s	16061
	SQPT	300 mW	2160 s	265019
Partial Polarization	DCQD	400 mW	1440 s	10810
	SQPT	300 mW	1620 s	111589
Complete Depolarization	DCQD	300 mW	960 s	21558
	SQPT	300 mW	2160 s	111244
T1\T2 Relaxation	DCQD	300 mW	1920 s	18501
	SQPT	300 mW	1440 s	86237

Table 5.1: The pump power and count information for each process characterization. The average count rate varied both with pump power and process. SQPT count rates were higher than those for DCQD because the states used for SQPT were produced more efficiently than the states for used for DCQD.

5.4 Experimental Details

5.4.1 Source

Our hyperentangled photon source was implemented by focusing 351-nm light from a continuous wave Ar⁺ laser to a $90 - \mu\text{m}$ beam waist onto two orthogonally oriented 0.6-mm-thick BBO crystals. The 702-nm type-I downconverted photons exited the crystals with a half-opening angle of 3°. The photons were filtered by 10-nm FWHM interference filters and detected by single-photon counting modules with a coincidence window of 10 ns. The pump power and therefore the downconversion count-rate unfortunately varied during our experiment due to deterioration of the pump laser. A full description of the laser power and counting statistics of each process is provided in the table below.

5.4.2 Error Compensation

To compensate for time-independent errors in both the state preparation and Bell state measurement, the two error sources had to be characterized independently of one another. Fortunately, because single-qubit DCQD only requires four experimental configurations, most of the information in these error maps is not required for error compensation. In fact, it is possible to completely compensate systematic errors by characterizing the input and measurement states with quantum state tomography with 45 experimental configurations⁴ ((4 input states)×(9 experimental configurations) + (1 measurement setting)×(9 experimental

⁴Here, the number total number of experimental configurations N_{tot} required to compensate error for a tomography technique as $N_{tot} \equiv (N_{in} \times I_{tomo}) + (N_{meas} \times M_{tomo})$, where N_{in} and N_{meas} are the number of input and measurement settings required for each process tomography technique and I_{tomo} and M_{tomo} are the number of measurement settings required to tomographically reconstruct each input and measurement state used the process tomography technique, respectively.

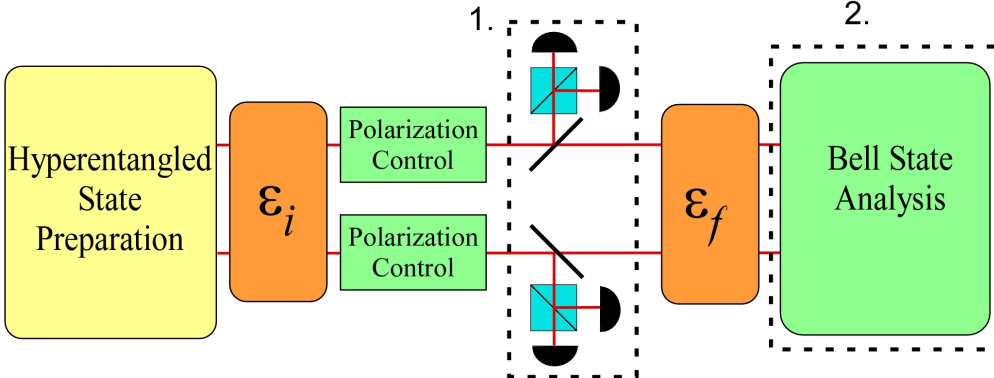


Figure 5.5: The two independent experimental configurations used sequentially to characterize systematic error in the state preparation and Bell state analysis. After the initial states were characterized (dashed box 1), the residual error in the Bell-state analyzer was characterized (dashed box 2). The only initial polarization states that needed to be characterized were the maximally entangled input state and one non-maximally entangled input state. The rest of the inputs required for DCQD and Bell-state analysis error compensation were produced from these two states using liquid crystals to perform polarization transformations.

configurations) = 45). This comparatively small number of required experimental settings is an improvement over the number of settings required to compensate errors in AAPT, between 54 ((1 input states) \times (9 experimental configurations) + (5 measurement settings) \times (9 experimental configurations) = 54) and 288 ((2 two-qubit quantum processes) \times (12² experimental configurations) = 288) experimental configurations depending on measurement strategy, but a disadvantage compared with SQPT which requires only 21 ((4 input states) \times (3 experimental configurations) + (3 measurement settings) \times (3 experimental configurations) = 21) experimental configurations. The figure below shows how the two error maps were independently characterized (see Fig. 5.5). The polarization states of the hyperentangled inputs were first characterized by performing a quantum state tomography when the experimental setup was in configuration 1 shown in Fig. 5.5. Once the input polarization states were characterized, the measurement states could be characterized by inserting a complete set of polarization states into the Bell-state analyzer when the experiment was in configuration 2. Examples of typical measured input and output states are shown below (see Fig. 5.6).

The spatial mode of the initial and final states need not be directly characterized at all because any effect that the initial and final error maps have on the spatial mode of the hyperentangled state is encapsulated in the characterization of the Bell state analyzer. The effect of the initial and final spatial mode errors can be measured together because they will commute with the polarization processes which the system is used to characterize. Once both the input and measurement states have been characterized, the errors in the characterized single-photon quantum processes are accounted for by replacing the ideal states with the measured states in the maximum-likelihood program.

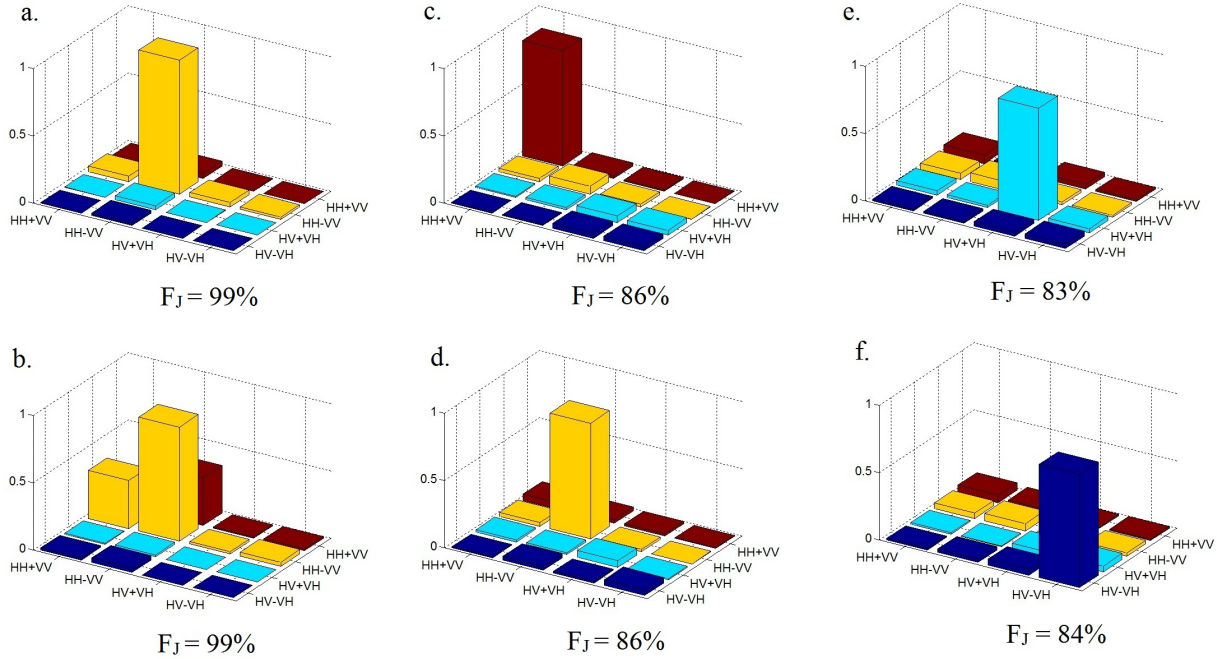


Figure 5.6: Typical measured density matrices of the maximally entangled (a) and non-maximally entangled (b) input states. All four input states required for DCQD can be produced by performing simple polarization transformations on these two initial states. c-f Also shown are the four states measured by the Bell state analyzer with state fidelities with ideal states; once these six states are characterized, any time-independent systematic error in DCQD measurements can be corrected.

5.4.3 Remaining Error Sources

Although time-independent error sources in the preparation and measurement states can be corrected if the errors are well characterized, there are error sources that cannot be compensated for using post-processing techniques. One such error source arises from statistical noise in photon counting statistics. Because photons leaving the pump laser are distributed randomly in time, the number of photons counted for each experimental configuration in DCQD and SQPT techniques will be subject to shot noise. It was possible to simulate the effect of this shot noise on DCQD measurements using the following procedure:

1. Using the experimentally measured error maps, DCQD measurement probabilities were calculated for a perfect process matrix.
2. A simulated set of counts (error compensation measurements + DCQD measurements) was statistically generated, assuming Poissonian statistics with mean value of the probability calculated in Step 1 multiplied by the total number of photons that were experimentally detected. These simulated counts were then used to reconstruct an error-compensated χ -matrix.

- Step 2 was repeated 200 times to build up a statistical distribution of the fidelities (of the simulated χ -matrices with the theoretical χ -matrix) which would be expected when measuring a perfect quantum process with the error sources that were experimentally measured.

This simulation was performed on the identity process, yielding a process fidelity of $98.6 \pm 0.7\%$, whereas the experimentally measured process fidelity was $97.3 \pm 0.9\%$. Both of these numbers agree with each other but are statistically different from 100% fidelity. This difference arises from the way shot noise acts on quantum processes. Because shot noise can only lower the fidelity of a measured quantum process with a target quantum process (theoretical or measured), a distribution of fidelities calculated using Monte Carlo techniques always be will statistically lower than 100%.

While the simulated and experimental fidelities of the identity process show expected statistical agreement, an additional uncompensated noise source was present in the experimental setup. This noise arose from counting fluctuations of the downconversion reaching the single-photon counting modules, due to pump laser power fluctuations and slight drifts in the single-mode fiber coupling. By monitoring these power fluctuations, we were able to characterize their typical influence on the statistical distribution of the number of photons detected. Using this information, we repeated the simulation described above for the identity process and obtained a corrected simulated fidelity of $96.7 \pm 1.7\%$, which shows complete agreement with the experimentally measured fidelity.

5.4.4 Scaling to Higher Dimensions

A major advantage of DCQD over other entanglement-enhanced process tomography techniques is its scalability to higher dimensions without requiring more complex measurements that themselves require many-body interactions. In fact, an n -qubit DCQD implementation requires the exact same type of experimental resources as required for 1-qubit DCQD (just in greater quantities). As an example, we have designed an experimental layout for a 2-qubit hyperentangled DCQD (see Fig. 5.7). This example layout generalizes to n -dimensional DCQD by using n hyperentangled photon pairs instead of two. While difficult, it is possible to scale DCQD to measure multi-dimensional polarization qubit processes, unlike other entanglement-enhanced process tomography techniques; although the latter may have similar or even better scaling in terms of the number of required experimental configurations, they require many-body interactions that are difficult or impossible to implement with linear optics.

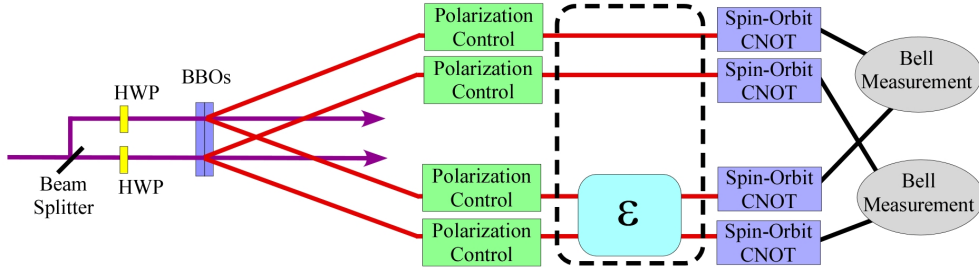


Figure 5.7: An experimental layout for 2-qubit polarization DCQD. The 16 input states required for 2-qubit DCQD are just the 16 possible tensor products of the 4 input states required for 1-qubit DCQD, i.e., the state of the first photon pair is in one of the four required inputs (Eqn. 2 or 3), as is that of the second pair. Similarly a 2-qubit Bell measurement is only performed on each photon pair.

5.5 Outlook

We implemented a powerful technique for reducing the number of experimental configurations required for characterizing quantum processes, through the use of hyperentanglement-assisted Bell-state measurement. Furthermore, we demonstrated how these processes could be characterized even when the measurement system is subject to systematic error. In general, it should be possible to further decrease the number of experimental configurations required to characterize certain classes of quantum processes, by combining DCQD techniques with “compressed sensing” methods that have already been used to characterize sparse quantum states and processes with far fewer experimental configurations than would normally be required [147, 148]. We have also begun studying the number of state copies DCQD needs (compared to other QPT techniques) to statistically constrain the error of process estimation. Our current numerical simulations indicate that DCQD requires fewer state copies than SQPT to constrain the error for some classes of unitary processes; further investigation is required to quantify more generally when DCQD has an advantage over SQPT in terms of the required number of state copies, but in all cases SQPT requires 3^n times more experimental configurations than DCQD.

Chapter 6

Conclusions

In this thesis I have described several examples where hyperentanglement can be used to enable quantum communication protocols that would be impossible using photons entangled in a single degree of freedom. Quantum-enhanced classical communication, quantum state communication, and quantum process characterization have all been demonstrated to benefit from the use of hyperentangled states. We have even shown that such states might be used to implement quantum communication protocols between a satellite and Earth. In addition, several future applications, such as high-dimensional tests of nonlocality [43], production of novel types of quantum entanglement [42], and cluster-state-based quantum computing [149] all might be enabled by the use of hyperentangled states.

However, while such states do provide a boost to the complexity of viable quantum information protocols, it should be emphasized that such states will *not* provide a route to scalable quantum information. Photons only have a few degrees of freedom on which information can be encoded. In addition, while continuous degrees of freedom, such as spatial and temporal mode, can theoretically encode an infinite amount of quantum information, the required number of modes grows exponentially with the number of qubits encoded. The control and measurement of such a large number of modes quickly becomes experimentally infeasible¹. Furthermore, though arbitrary quantum gates can be performed between the different degrees of freedom of the individual photons of a hyperentangled photon pair, the class of available operations and measurements on the full two-photon state is still severely constrained by the lack of nonlinear interactions (see Section 2.2.2). For these reasons, hyperentangled states cannot be used as a replacement for multi-particle quantum information with strong nonlinear interactions. However, despite these limitations, hyperentanglement makes it possible to experimentally explore the properties of high-dimensional quantum states using low-overhead methods that are possible with current technology.

¹In contrast, if multi-photon states are used to encode quantum information, the number of required photons grows linearly with the number of qubits encoded.

Appendix A

Hybrid versus Hyperentangled Superdense Coding

As mentioned in Section 2.2.1, the results of previous experiments using hyperentanglement to increase the channel capacity of linear superdense coding [57] can be replicated by a much simpler single-photon experiment. This single-photon protocol (see Fig. A.1), like the original hyperentanglement implementation, uses a 2-qubit quantum channel and only requires Alice to manipulate the polarization of her photon (rather than both polarization and spatial mode). However, instead of requiring the creation, distribution, and storage of a hyperentangled state, Alice can locally create a single-photon two-qubit state $a^+ \equiv \frac{1}{\sqrt{2}}(|Hl\rangle + |Vr\rangle)$ using a single-photon source and spatially varying birefringent element [150]. She can then encode her message by manipulating the polarization of her photon so that it is in one of the following four single-photon spin-orbit Bell states: $\frac{1}{\sqrt{2}}(|Rr\rangle \pm |Ll\rangle)$ and $\frac{1}{\sqrt{2}}(|Lr\rangle \pm |Rl\rangle)$. She then transmits the photon to Bob who decodes the message using a spin-orbit CNOT gate (see Fig. 2.3), thereby achieving a theoretical channel capacity of 2 bits/photon. This is in agreement with the Holevo bound for a two-qubit quantum channel [47]. In fact, this procedure has recently been experimentally implemented [19]. In contrast, the hyperdense coding technique described in Chapter 2 exceeds this bound, so its enhanced channel capacity cannot be matched by any two-qubit single-photon protocol.

It might be argued that though these two techniques have similar channel capacities, the hyperentanglement-enhanced superdense coding provides a secure information channel between Alice and Bob while the single-photon method described above does not. However, for the former technique to be secure, the original distribution of the two-photon state to Alice and Bob must be secured. If not, then an eavesdropper (Eve) can either measure Alice's or Bob's photon in the spin-orbit Bell state basis and resend the state that she measures to the relevant party. By making her measurement, Eve collapses the state into a known product state of two single-photon Bell states. If Eve again measures and resends Alice's photon after the message is encoded, Eve can learn its contents without being detected or disrupting what Bob receives. Thus for this technique to be secure, there must be a safe channel to distribute the original hyperentangled state to Alice and Bob. However, if such a secure channel indeed exists, one could simply exchange a one-time pad between Alice and Bob which could then be used to secure the two-qubit single-photon protocol described

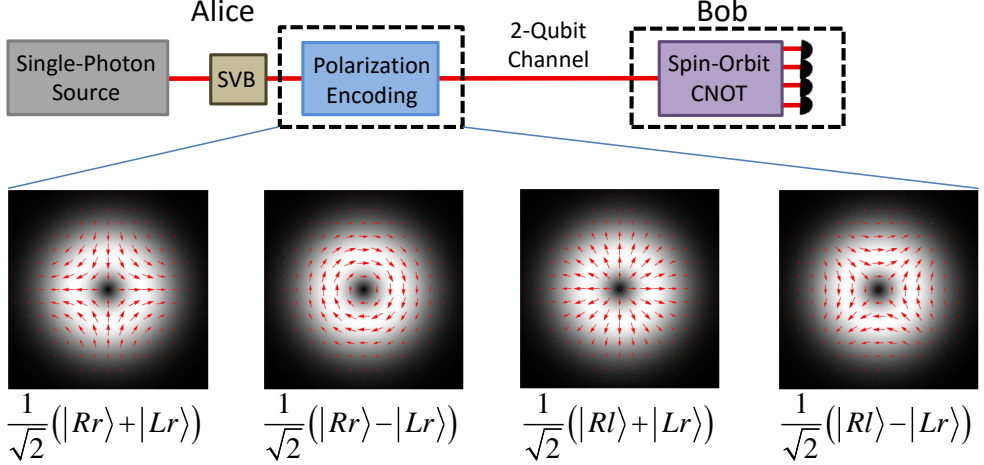


Figure A.1: Experimental setup for single-photon two-qubit coding. Alice creates a single-photon two-qubit Bell state using a single-photon source and a spatially varying birefringent element (SVB). Alice can then encode her message by changing only the polarization state of her photon. The photon is then transmitted through a two-qubit channel (one qubit for both polarization and spatial mode), after which Bob can decode the message using a spin-orbit CNOT gate.

above. Therefore, the hyperentanglement-enhanced technique does not offer any additional message security over the single-photon protocol.

Appendix B

General versus Equimodular State Space Comparisons

B.1 Packing Number and Volume Ratio

One way to measure the complexity of a set of states is to consider the “packing number” with respect to the Bures distance [151]. For states with an angle less than $\pi/2$, the Bures distance coincides with the usual Euclidean distance, which will be used here for simplicity.

Given a subset T in a d -dimensional real Euclidean space \mathbb{R}^d , we define the *packing number* $P(T, \delta) = \max(N)$ as the maximal number of points x_1, \dots, x_N in T such that $\|x_j - x_k\| > \delta$ for all $1 \leq j \neq k \leq N$. For example, in \mathbb{R}^3 , it is the number of ball of radius δ that can be packed into a larger volume T^1 . If T is sufficiently smooth and of dimension n , we have:

$$\lim_{\delta \rightarrow 0} \left(\frac{\delta}{2}\right)^n P(T, \delta) = c(n) \text{vol}_n(T). \quad (\text{B.1})$$

Here $\text{vol}_n(T)$ is the n -dimensional measure [152] and $c(n)$ is the packing density of Euclidean space. It is known that $\frac{\zeta(n)}{2^n} \leq c(n) \leq 1$ holds for the Riemann ζ -function [153]. The estimate $c(1) = 1$ is easy, and $c(2) = \frac{\pi}{\sqrt{18}}$ is due to Gauss. For larger dimensions, only lower and upper estimates are known, see e.g., [154].

For the set of equimodular states $T_n = n^{-1/2} \mathbb{T}^n \subset \mathbb{C}^n$, $d = n - 1$ (because $\mathbb{C}^n = \mathbb{R}^{2n}$) and

$$\text{vol}_d(T_n) = n^{-\frac{n-1}{2}} (2\pi)^{n-1}, \quad (\text{B.2})$$

where we divide by 2π to account for the fact that a global phase does not change the state. Let us compare this with a sphere of dimension d , i.e., the set of vectors $S^d \subset \mathbb{R}^{d+1}$ of points of length 1. Let us denote by B_{d+1} the unit ball in \mathbb{R}^{d+1} , i.e., the set of all points of length less than one. It is well known that

$$\text{vol}_{d+1}(B_{d+1}) = \frac{\pi^{(d+1)/2}}{\Gamma\left(\frac{d+1}{2} + 1\right)}. \quad (\text{B.3})$$

¹to avoid “edge effects”, we implicitly assume a “nice” volume T (e.g., a smooth ball) that is much bigger in volume than the volume of any of the balls we are packing.

Using polar coordinates and Stirlings formula $\Gamma(z) \sim \sqrt{2\pi z} \left(\frac{z}{e}\right)^z$ this implies

$$\begin{aligned} \text{vol}_d(S^d) &= \frac{(d+1)\pi^{\frac{d+1}{2}}}{\Gamma\left(\frac{d+1}{2} + 1\right)} \sim \frac{(d+1)\pi^{\frac{d+1}{2}}}{\sqrt{\pi(d+1)}} \left(\frac{2e}{d+1}\right)^{\frac{d+1}{2}} \\ &\sim \sqrt{2}(2\pi e)^{d/2} d^{-d/2}. \end{aligned} \quad (\text{B.4})$$

Here the \sim symbol denotes that if $a_d \sim b_d$ then $\lim_{d \rightarrow \infty} a_d/b_d = 1$. The error of this approximation can be reduced by including higher-order terms when approximating the Γ -function. For $d = n - 1$ we find

$$\begin{aligned} \text{vol}_d(T_n) &= (2\pi)^{n-1} n^{-\frac{n-1}{2}} > \sqrt{2}(2\pi e)^{\frac{n-1}{2}} (n-1)^{-\frac{n-1}{2}} \\ &\sim \sqrt{2e}(\sqrt{2\pi e})^{n-1} n^{-\frac{n-1}{2}} = \text{vol}_d(S^d), \end{aligned} \quad (\text{B.5})$$

because $2\pi > \sqrt{2\pi e}$. Thus, the packing number for a torus is larger than the corresponding packing number for a sphere of the same dimension, assuming small δ . For these calculations, we have assumed that the general class of states is embedded in a sphere instead of a complex projective space. However, a full calculation in complex projective space still shows that the ratio of the volumes of equimodular versus general states of the same number of parameters grows exponentially with the dimension (see Supplementary Note 2 of [110]). In realistic quantum communication experiments, systematic error and a limited number of state copies will constrain the minimum statistical distance (δ) by which two states can be separated and still be experimentally distinguished. To address this issue, the packing numbers of equimodular versus general quantum states for a fixed threshold δ has been analyzed (see Supplementary Note 3 of [110]). While the relative sizes of the two classes of states could not be directly computed under these conditions, it could still be concluded that the two volumes differed by at most a multiplicative factor (which could not be computed) that is independent of d .

B.2 Classical Teleportation Fidelity

To establish the optimal average fidelity with which a d -dimensional quantum state can be transmitted over a classical channel without entanglement, we must determine how well the state can be estimated with a single optimal measurement. Alice then makes this measurement and sends the result to Bob (who knows Alice's measurement strategy), who makes a state estimation based on this message. The best average fidelity that one can achieve using this classical teleportation strategy has been calculated to be [94]:

$$F_{\text{general}} = \frac{2}{1+d} = \frac{4}{4+N} \sim \frac{4}{N}. \quad (\text{B.6})$$

Because the hyper-area of an equimodular state is larger than that for a general quantum state of the same number of parameters, the former are more difficult to send classically (see Appendix B.1). The average fidelity of an optimal state estimation strategy can be calculated using the well-established methods of Massar and Popescu [92]. It is optimal to measure in a basis which is mutually unbiased to the basis in which Charles applies the phases, for example:

$$|k\rangle \equiv \frac{1}{\sqrt{d}} \sum_{j=0}^{d-1} e^{i\frac{2\pi j k}{d}} |j\rangle, \quad (\text{B.7})$$

where d is the dimension of the space and N is the number of state parameters defining the state. For a general quantum state $N = 2d - 2$. If Alice measures in this basis and sends the result to Bob, it is the optimal strategy for Bob to simply guess the same state that Alice measured. The average fidelity of his state is then:

$$F_{\text{equimodular}} \equiv \sum_{k=0}^{d-1} \int \frac{d\Phi}{(2\pi)^d} F(k, \Phi) P(k, \Phi) = \frac{1}{d^4} \sum_{k=0}^{d-1} \int \frac{d\Phi}{(2\pi)^d} \left| \sum_{j=0}^{d-1} e^{i(\Phi_j - \frac{2\pi j k}{d})} \right|^4, \quad (\text{B.8})$$

where $P(k, \Phi)$ is the probability that Alice detects state k of the measurement basis, $F(k, \Phi)$ is the fidelity of Bob's guess, given that Alice measured state k , and Φ is the set of phases which parameterize the set of equimodular states. After shifting phase angles by $\frac{2\pi j k}{d}$ (by a simple redefinition), we evaluate the sum over k to obtain:

$$F_{\text{equimodular}} = \frac{1}{d^3} \int \frac{d\Phi}{(2\pi)^d} \left| \sum_{j=0}^{d-1} e^{i\Phi_j} \right|^4 = \frac{1}{d^3} \int \frac{d\Phi}{(2\pi)^d} \sum_{i,j,k,l=0}^{d-1} e^{i(\phi_i + \phi_j - \phi_k - \phi_l)}. \quad (\text{B.9})$$

The integral is unity for all phase combinations that add to zero, and zero for all other combinations:

$$F_{\text{equimodular}} = \frac{1}{d^3} \sum_{i+j-k-l} 1. \quad (\text{B.10})$$

These indexes add to zero when $i = k$ and $j = l$ (occurs d^2 times) and when $i = l$ and $j = k$ (occurs d^2 times); however, this double-counts when $i = k = j = l$ (occurs d times). Therefore, the optimal average fidelity for an equimodular state becomes:

$$F_{\text{equimodular}} = \frac{2d^2 - d}{d^3} = \frac{2N + 1}{(N + 1)^2}, \quad (\text{B.11})$$

where the number of state parameters defining a d -dimensional equimodular state is $N = d - 1$.

Thus, we see that the average classical teleportation fidelity for equimodular ququart states is $\frac{2 \cdot 3 + 1}{(3+1)^2} = 44\%$. Examining the asymptotic behavior of the average fidelity for large N ($F_{\text{equimodular}} \sim \frac{2}{N}$) of general states (see Equation B.6) versus equimodular states (see Equation B.11), we see that equimodular states can be transmitted over a classical channel (without entanglement) with on average half the fidelity that general states (with the same number of state parameters) can be transmitted.

Appendix C

Using Pockels Cells and Liquid Crystals

Pockels cells and liquid crystals are active optical elements that can be used to manipulate the polarization state of light transmitted through them. Both elements act as voltage-dependent birefringent elements; however, their operating specifications are very different, so they are often used in very different applications. Liquid crystals, for example, are often used as variable waveplates and can be used as a relatively fast (rise times $\sim 10ms$) alternative to rotating wave plates. These devices are composed of a fluid containing elongated, polar molecules; the fluid is contained between two glass windows with transparent electrodes on their surface. When grounded the elongated molecules tend to align with narrow grooves etched into the glass window, causing the element to become birefringent (see Fig. C.1). As voltage is applied to the electrodes, the molecules begin to align with the field perpendicular to the glass windows, and the elements birefringence is reduced (though never quite reaching zero). All of the change in birefringence comes from changes in the extraordinary index of refraction (i.e., the ordinary index of refraction is unaffected by voltage changes), so a liquid crystal aligned at 0° (i.e., with the glass grooves vertically aligned) can be described by the following unitary operation:

$$U_{LC} = \begin{matrix} & |H\rangle & |V\rangle \\ \begin{matrix} |H\rangle \\ |V\rangle \end{matrix} & \left[\begin{array}{cc} 1 & 0 \\ 0 & e^{i\phi(V)} \end{array} \right] \end{matrix}, \quad (\text{C.1})$$

where the birefringent phase ϕ is a function of the voltage (V) on the liquid crystal. Knowing that the ordinary polarization is unaffected by voltage changes is particularly important when liquid crystals are used in interferometers, where it is not only important to know how polarization in one arm changes but also how the phase of both ordinary and extraordinary polarizations change relative to the polarization terms in the other interferometer arm (see Chapters 2, 3, and 4).

Pockels cells tend to be used very differently than liquid crystals in experiments because they are much more expensive, require kV-level voltages, are larger in size, and more difficult to align. However, the birefringence of Pockels cells can be changed far more quickly (rise times of $\sim 1ns$ are possible) than the birefringence of liquid crystals. These two aspects of Pockels cells result in them being used almost exclusively

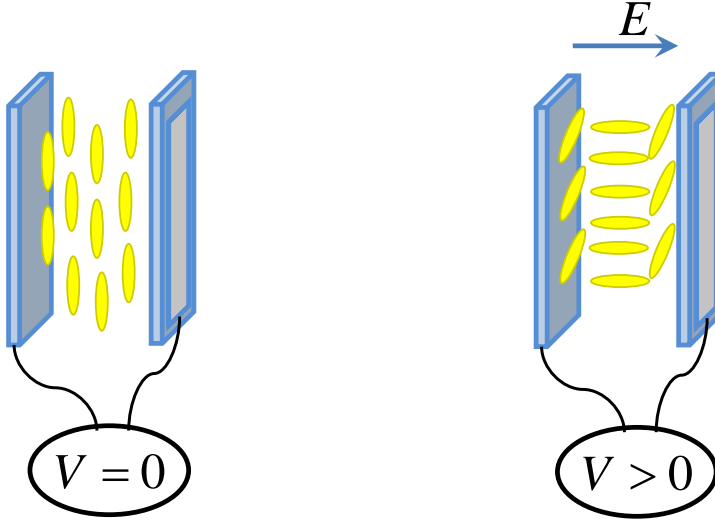


Figure C.1: When a liquid crystal is grounded, molecules tend to align with small grooves etched in the glass windows. When a voltage is applied to the electrodes, them molecules start to align with the electric field.

for fast-switching applications or field modulation. In particular, they are often used in quantum optics experiments for feed-forward correction (e.g., in teleportation experiments) or manipulating temporal modes of photons. In many such applications, no special care is needed to understand exactly how the refractive indices of the Pockels cell change when voltage is applied, and the birefringence of the Pockels cell is the only relevant parameter. However, when used in polarization- and temporal-mode hyperentanglement applications, care must be taken to understand how all refractive indices of the crystals are changed when voltage is applied.

When an electric field is applied to a medium, its refractive indices change through a process known as the electro-optic effect. The Pockels effect is the *linear* electro-optic effect and is only present in non-centrosymmetric crystals. In this effect, the ellipse parameterizing the refractive indices¹:

$$1 = \frac{x^2}{n_x^2} + \frac{y^2}{n_y^2} + \frac{z^2}{n_z^2}, \quad (\text{C.2})$$

is deformed by an applied electric field [63]:

$$1 = \sum_{k=1}^3 \left(\frac{1}{n_x^2} + r_{1,k} E_k \right) x^2 + \left(\frac{1}{n_y^2} + r_{2,k} E_k \right) y^2 + \left(\frac{1}{n_z^2} + r_{3,k} E_k \right) z^2 + 2yzr_{4,k} E_k + 2xzx_{5,k} E_k + 2xyr_{6,k} E_k, \quad (\text{C.3})$$

where E_k is the electric field applied along the k axis (and $x \equiv 1$, $y \equiv 2$, $z \equiv 3$), n_j is the refractive index

¹Here, the principle refractive indices of the crystal are set to align with the x, y, and z axes.

in the j direction, and $r_{i,j}$ are the electro-optic coefficients which are determined by the crystal structure. For example, Rubidium Titanyl Phosphate (RTP) is an orthorhombic crystal and has the following non-zero electro-optic coefficients²: $r_{1,3}, r_{2,3}, r_{3,3}$. Therefore, when the crystal is X-cut (i.e., cut so the X crystal axis is perpendicular to the crystal window) and an electric field is applied along the z-axis (see Fig. C.2), then:

$$\begin{aligned} n_y(E) &\approx n_{y0} - n_{y0}^3 r_{2,3} E_z \\ n_z(E) &\approx n_{z0} - n_{z0}^3 r_{3,3} E_z, \end{aligned} \quad (\text{C.4})$$

where $n_{k0} \equiv n_k(E = 0)$. The crystal becomes birefringent because $r_{2,3} < r_{3,3}$, so a single X-cut RTP crystal Pockels cell at 0° (i.e., the z crystal axis is vertically aligned) will apply phases of the form:

$$U_{LC} = \begin{array}{c|cc} & |H\rangle & |V\rangle \\ \begin{array}{c} |H\rangle \\ |V\rangle \end{array} & \left[\begin{array}{cc} e^{-i\phi_1(V)} & 0 \\ 0 & e^{-i\phi_2(V)} \end{array} \right] \end{array}, \quad (\text{C.5})$$

where $\phi_1 = \frac{2\pi L n_{y0}^3 r_{2,3} E_z}{\lambda}$ and $\phi_2 = \frac{2\pi L n_{z0}^3 r_{3,3} E_z}{\lambda}$. However, RTP Pockels cells are typically composed of identical pairs of RTP crystals that are orthogonally oriented (to cancel out the intrinsic birefringence when no field is applied). In the first crystal, the electric field is applied in the z-direction, and in the second crystal, the electric field is applied in the $-z$ -direction. Together, these two crystals apply the following polarization rotation:

$$U_{LC} = \begin{array}{c|cc} & |H\rangle & |V\rangle \\ \begin{array}{c} |H\rangle \\ |V\rangle \end{array} & \left[\begin{array}{cc} e^{i\phi_2(V)} & 0 \\ 0 & e^{i\phi_1(V)} \end{array} \right] \left[\begin{array}{cc} e^{-i\phi_1(V)} & 0 \\ 0 & e^{-i\phi_2(V)} \end{array} \right] = \begin{array}{c|cc} & |H\rangle & |V\rangle \\ \begin{array}{c} |H\rangle \\ |V\rangle \end{array} & \left[\begin{array}{cc} e^{i(\phi_2(V)-\phi_1(V))} & 0 \\ 0 & e^{i(\phi_1(V)-\phi_2(V))} \end{array} \right] \end{array}. \quad (\text{C.6})$$

When the Pockels cell's half-wave voltage is applied (i.e., the voltage that gives a π -phase shift between the two eigen-polarizations), the two-crystal X-cut RTP Pockels cell will apply rotations of the form:

$$U_{LC} = \begin{array}{c|cc} & |H\rangle & |V\rangle \\ \begin{array}{c} |H\rangle \\ |V\rangle \end{array} & \left[\begin{array}{cc} e^{i\frac{\pi}{2}} & 0 \\ 0 & e^{-i\frac{\pi}{2}} \end{array} \right] \end{array}. \quad (\text{C.7})$$

Therefore, polarization- and temporal-mode hyperentanglement experiments with fast switching must be

²The specific values of these electro-optic coefficients depend on the frequency of the applied E -field and the frequency of the light being transmitted through the crystal.

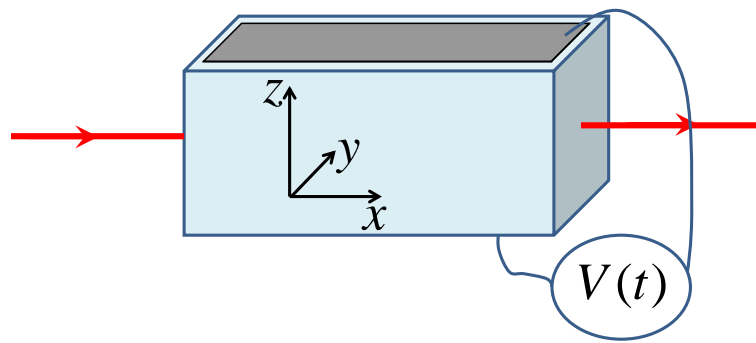


Figure C.2: An X-cut RTP Pockels cell is oriented such that the x-crystal axis is perpendicular to the beam propagation direction. An electric field is applied along the z-crystal axis by applying a voltage across two electrodes on the respective crystal faces.

designed to account for the fact that this Pockels cell applies phase-shifts to both eigen-polarizations when voltage is applied to it.

Appendix D

Designing Holograms

Holograms are important tools for manipulating the spatial mode of photons and can be used to modify the phase and/or the intensity distribution of incident light. To design a hologram that modifies the beam distribution in a particular fashion, it is necessary to have a basic understanding of the effect that holograms have on light fields. Specifically, holograms act as transmission screens for the light field:

$$U_{nf}(x, y, z = 0) = T(x, y)U_0(x, y, z = 0), \quad (\text{D.1})$$

where $U_0(x, y)$ and $U_{nf}(x, y)$ are the amplitude of the light field immediately before and after the hologram transmission screen $T(x, y)$ located at $z = 0$ (see Fig. D.1). As the light field propagates in the z -direction, it will change due to diffraction. At a distance far away from the hologram and near to the beam axis¹, the light field can be approximated as a Fourier transform (also known as the Fraunhofer approximation):

$$U_{ff}(x', y', z) \propto \widetilde{U_{nf}}\left(\frac{x'}{\lambda z}, \frac{y'}{\lambda z}\right), \quad (\text{D.2})$$

where $\widetilde{U_{nf}}$ represents the Fourier transform of U_{nf} and x' and y' are coordinates of the field far away from the hologram (see Fig. D.1).

To design a hologram which yields the desired light amplitude in the far-field, the field can be back-propagated using an inverse Fourier transform from the image space to the plane of the hologram surface ($z = 0$) to find U_{nf} :

$$U_{nf}(x, y, z) \propto \widetilde{U_{ff}}^{-1}\left(\frac{x}{\lambda z}, \frac{y}{\lambda z}\right) \quad (\text{D.3})$$

The ideal hologram transmission screen T can then be calculated by solving Equation D.1 by taking the ratio of the back-propagated field (U_{nf}) to the input field (U_0).

In general, the hologram transmission screen will require both phase and amplitude terms to form a

¹In this context, far away corresponds to $z \gg \frac{r_{max}d_h}{\lambda}$, where d_h is the feature size (e.g., the spacing of a grating hologram) of the field $T(x, y)$, r_{max} is the maximum distance away from the z -axis that the distribution spans, and λ is the wavelength of light incident on the hologram.

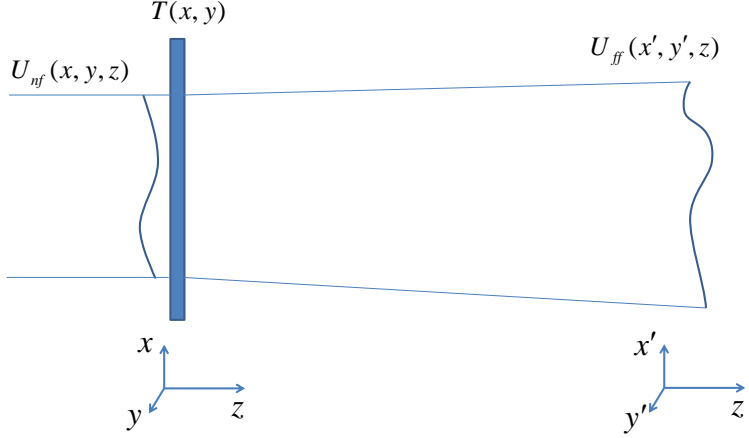


Figure D.1: An incident light field U_{nf} is incident on the hologram transmission screen T . The far-field light field U_{ff} can be approximated by the Fourier transform of the product of the incident field and the transmission screen.

particular far-field distribution. However, most often, holograms modify either the amplitude or intensity distribution of incident light, not both. In addition, for “binary” holograms, $T(x, y)$ can only take on one of two possible values². Such constraints greatly limit the variety of far-field distributions that one can obtain. However, it is still possible to generate an arbitrary field distribution in a *portion* of the image plane, by incorporating a binary diffraction grating in $T(x, y)$. Using this technique, a target field distribution can be created in the +1 diffraction order but at the cost of reduced efficiency, since some of the light is also directed into the other diffraction orders. The maximum diffraction efficiency of light in the +1 diffraction order of binary phase and binary amplitude holograms is 40.5% and 10.1% [155], respectively³.

A grating hologram that produces U_{ff} in the +1 diffraction order can be designed through application of the Fourier shift theorem. To shift $U_{ff}(x', y', z_{im}) \rightarrow U_{ff}(x' - a, y', z_{im})$, where a is the horizontal displacement of the +1 diffraction order in the image plane $z = z_{im}$, the hologram transmission screen is multiplied by a complex phase $T_s(x, y) \equiv e^{\frac{2\pi i x a}{\lambda z_{im}}} T(x, y)$. A binary hologram can then be designed by choosing the binary transmission function that most closely matches the shifted transmission function. For binary *phase* holograms, in-phase components of $T_s(x, y)$ (i.e., $\text{Re}(T_s x, y) > 0$) are rounded to a value of 1 (i.e., a phase of 0) while out-of-phase components (i.e., $\text{Re}(T_s x, y) < 0$) are rounded to a value of -1 (i.e., a phase of π). For binary *amplitude* holograms, in-phase components of $T_s(x, y)$ (i.e., $\text{Re}(T_s x, y) > 0$) are rounded to a value of 1 while out-of-phase components (i.e., $\text{Re}(T_s x, y) < 0$) are rounded to a value of 0. The binary phase holograms used to measure spatial modes in Chapters III and V can be constructed in this fashion (see Fig. D.2). Using these techniques, U_{ff} can be approximately reconstructed in the +1

²For binary phase holograms, $T(x, y)$ usually takes on values of 1 or -1 (i.e., phase of 0 or π); for binary amplitude holograms $T(x, y)$ usually takes on values of 0 or 1.

³Arbitrary phase and amplitude holograms can achieve efficiencies of 50% and 12.5% respectively.

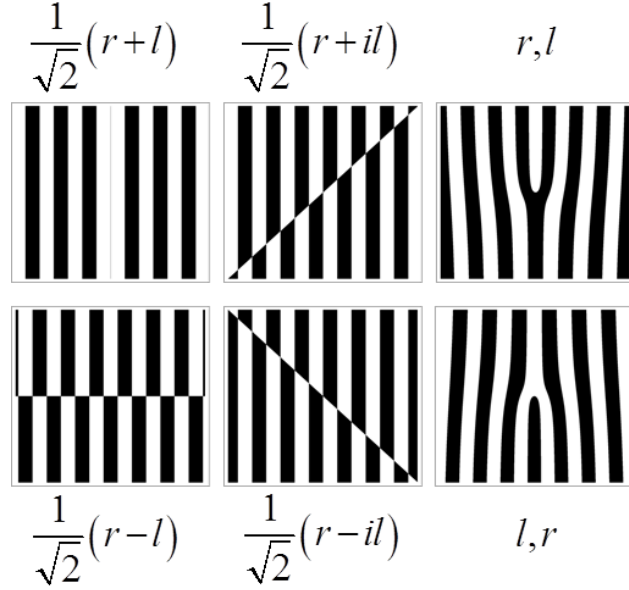


Figure D.2: Binary grating holograms in conjunction with single mode-fibers (used as spatial filters) can be used for qubit spatial-mode tomography. Shown here are a set of holograms to make a complete set of measurement in the ± 1 orbital angular momentum basis (r and l respectively).

diffraction order; however there can be some artifact error from the rounding processes. Such artifact errors can often be significantly reduced using iterated hologram design algorithms, such as Gerchberg-Saxton [156] or mixed-region amplitude freedom [157] algorithms, but a detailed discussion of these is beyond the scope of this manuscript.

Appendix E

Tomographic Reconstruction of Quantum States

E.1 Representation of Quantum states

Quantum state tomography is the procedure of fully characterizing the properties of a state. Such a complete description of a quantum state can then be used to calculate the relative probability of any measurement outcome made on the state, and how the state will change when acted on by known quantum gates. However, such a description is often challenging to determine experimentally, since a single measurement on a particle reveals only a small amount of the information describing it. For example, a d -dimensional pure state (i.e., a state that can be expressed as a state vector $|\psi\rangle$) is described by $2d - 2$ continuous parameters. A projective measurement made on this state will yield one of d possible outcomes sampled from a statistical distribution determined by the state parameters and the measurement basis. Measurements must be made on many copies of the state in many different bases in order to determine the parameters.

Further complicating matters, experimentally generated quantum states are not completely pure. They cannot be expressed as a simple state vectors and must be described as statistical mixtures of pure states, usually represented by density matrices [25]. The density matrix of a pure state (ρ_{pure}) is simply the tensor product of the state with itself:

$$\rho_{pure} \equiv |\psi\rangle\langle\psi|. \quad (\text{E.1})$$

General quantum states can then be described by a weighted sum of pure states:

$$\rho = \sum_i \alpha_i |\psi_i\rangle\langle\psi_i|. \quad (\text{E.2})$$

Thus, any d -dimensional quantum state can be expressed as a $d \times d$ -dimensional density matrix. Density matrices are complex and Hermitian, so they have d^2 free parameters (if left unnormalized)¹. The goal of quantum state tomography is to determine the values of these parameters which best describe the quantum

¹It is useful to leave density matrices unnormalized (a normalized density matrix has $d^2 - 1$ free parameters) for this discussion because the brightness (i.e., number of copies per second) of experimentally created optical quantum states is often unknown. leaving the state unnormalized allows the reconstruction algorithm to determine the brightness along with all the other state parameters that define the quantum state.

state created in the lab, by making projective measurements on many copies of the state.

To achieve this goal, measurement settings must be chosen which can (given infinite state copies) uniquely determine the state. Such an “informationally complete” set of measurements must have at least d^2 outcomes (for an unnormalized density matrix) that are linearly independent when expressed in terms of the density matrix parameters. An “over-complete” set of measurement settings is one in which more settings are used to determine the quantum state than are needed. It is often advantageous to use an over-complete measurement set, since the redundant information can be used to identify measurement errors and drift in the experimental setup, and often provide more precise reconstructions given a limited number of state copies [118].

E.2 Maximum Likelihood State Estimation

Maximum likelihood state estimation is perhaps the most commonly used strategy for determining a quantum state from a list of measurement outcomes [91]. In this technique, measurements ($\rho_m^{(j)}$) are made in an informationally complete set, and the measurement outcomes are used to compute a likelihood function: here j is an index over measurement settings ρ_m . A likelihood function returns the probability that a given test density matrix could have produced the observed measurement outcomes. The quantum state most likely to have produced the observed measurement outcomes is then determined by maximizing this likelihood function.

Before a likelihood function is calculated, it is helpful to parameterize the test matrix in such a way that it is constrained to be a “legal” density matrix (i.e., positive semi-definite and Hermitian). One way to accomplish this is to write the test matrix parameters in terms of the Cholesky decomposition:

$$\rho_{test} = LL^\dagger, \quad (\text{E.3})$$

where L is a $d \times d$, complex, lower triangular matrix with real-valued principal diagonals. The d^2 real parameters required to describe this matrix can be varied freely and ρ_{test} will remain a valid density matrix.

To calculate a likelihood function, the measurement outcomes must be used to calculate a probability distribution. In photon experiments, many state copies are usually measured over a predetermined time interval for each measurement setting (e.g., when measuring photon polarization, waveplates and polarizers are set to angles corresponding to a specific measurement setting, photons are then counted for the measurement time interval and the number is recorded). If there are no systematic noise sources (e.g., laser fluctuation, setting drift, detector efficiency change, etc.), then the number of photons ($N^{(j)}$) detected in the

time interval for measurement setting $\rho_m^{(j)}$ can often be assumed to be an element of a Poisson distribution². If $N^{(j)}$ is large enough ($>\sim 15$ detection events), then the Poisson distribution can be well approximated by the following Gaussian distribution:

$$P(N^{(j)}, \rho_{test}) = A^{(j)} e^{\frac{(N^{(j)} - Tr[\rho_m^{(j)} \rho_{test}])^2}{(\sigma^{(j)})^2}}, \quad (\text{E.4})$$

where $A^{(j)}$ is the normalization constant of the distribution and the standard deviation of the distribution $\sigma^{(j)}$ is approximately equal to $Tr[\rho_m^{(j)} \rho_{test}]$ if systematic noise is negligible³. The likelihood function is the product of the probabilities of every measurement setting:

$$L(\rho_{test}) = \prod_j P(N^{(j)}, \rho_{test}). \quad (\text{E.5})$$

This likelihood function can then be maximized using various numerical methods. It is numerically faster to minimize the log of the likelihood function (i.e., $\log[L(\rho_{test})]$) rather than trying to maximize the likelihood function. The test matrix which minimizes the log of the likelihood function is the density matrix most likely to describe the quantum state of the measured photons⁴.

Error for the quantum state can be calculated through Monte Carlo methods. Specifically, a new count set ($N^{(j)}$) can be numerically generated by selecting random variates of the probability distribution given in Equation E.4. New density matrices can then be generated from the count sets and used to calculate the standard deviations of the density matrix elements and relevant measures, such as fidelity and purity.

E.3 Problems With Maximum Likelihood

While maximum likelihood is an easy technique to implement, there are several situations where it can give erroneous results. The accuracy of maximum likelihood state reconstruction is dependent on the number of states measured. If too few counts are measured, then it will bias the reconstructed quantum state to look “purer” than it actually is [160]. Such biasing can also take place even for large count numbers if the measured quantum states are very close to pure. In such situations, other techniques such as Bayesian mean

²The specific statistical distribution of counts will vary for different sources. However, a Poisson distribution is an accurate description of many commonly used laboratory light sources, such as lasers and downconversion sources with many spectral and/or spatial modes [158]. In addition, imperfect photon collection and detection will cause a non-Poisson light source to more closely resemble a Poisson distribution. If a light source with different photon number statistics is used, then the relevant probability distribution can be substituted into the likelihood function.

³Many times systematic noise is *not* negligible, especially for large $N^{(j)}$. In most cases, it is better practice to experimentally measure $\sigma^{(j)}$.

⁴The techniques described here are a description of basic maximum likelihood techniques. For more complete description of these techniques see [159].

quantum state reconstruction can be used to avoid biased results [160].

Appendix F

Detector Annealing

Avalanche photodiodes are ideal for space-based photon counting experiments since they have a small form factor, low power consumption, and high efficiency. However, they are also susceptible to radiation damage. In particular, the dark count rate of avalanche photodiodes has been shown to increase when they are exposed to radiation [120]. This can present a problem for space use, since detectors will be exposed to much higher levels of radiation without the Earth’s atmosphere shielding them. If left unchecked, then the rising dark-count rate of these detectors will overwhelm the signal, thus rendering them unusable. This issue is exacerbated by the fact that count rates in satellite-to-Earth quantum communication applications will likely be quite small since photons must be transmitted and collected over very large distances (see Section 4.4.2).

One strategy to combat this degradation is to use a recently discovered technique to optically anneal detectors and reduce dark counts [161]. In this technique, a bright laser ($\sim 1W$) is directed onto the silicon wafer of a (deactivated) avalanche photodiode to heat it and anneal out charge traps that might give rise to dark counts. Using this technique, the authors demonstrated that the dark count rate of the detectors initially increased before permanently decreasing by a factor of up to 5.4 (compared to their pre-annealing values), without affecting the detection efficiency. In collaboration with Thomas Jennewein and Vadim Makarov at the Institute for Quantum Computing in Waterloo, we have demonstrated that optical annealing can also be used to reduce the dark counts of avalanche photodiodes that have been exposed to proton radiation.

To demonstrate this effect, as SLIK Si avalanche photodiode was irradiated with ~ 100 MeV proton radiation at a flux of 10^9 protons/cm² at the TRIUMF accelerator in Vancouver, BC. To avoid thermal annealing the photodiode was kept at $\sim 0^\circ$ C as it was transported to Waterloo, ON, and then to Urbana, IL. As predicted, the proton radiation significantly increased the dark count rate from a pre-exposure rate of ~ 400 Hz to $\sim 70,000$ Hz. The detector was then illuminated with 808-nm light of varying power levels for 60 s at each brightness (see Fig. F.1a); after each 60-s illumination period, the dark count rate was measured (see Fig. F.1b). As in previous experiments, the dark count rate initially increased before decreasing. Using

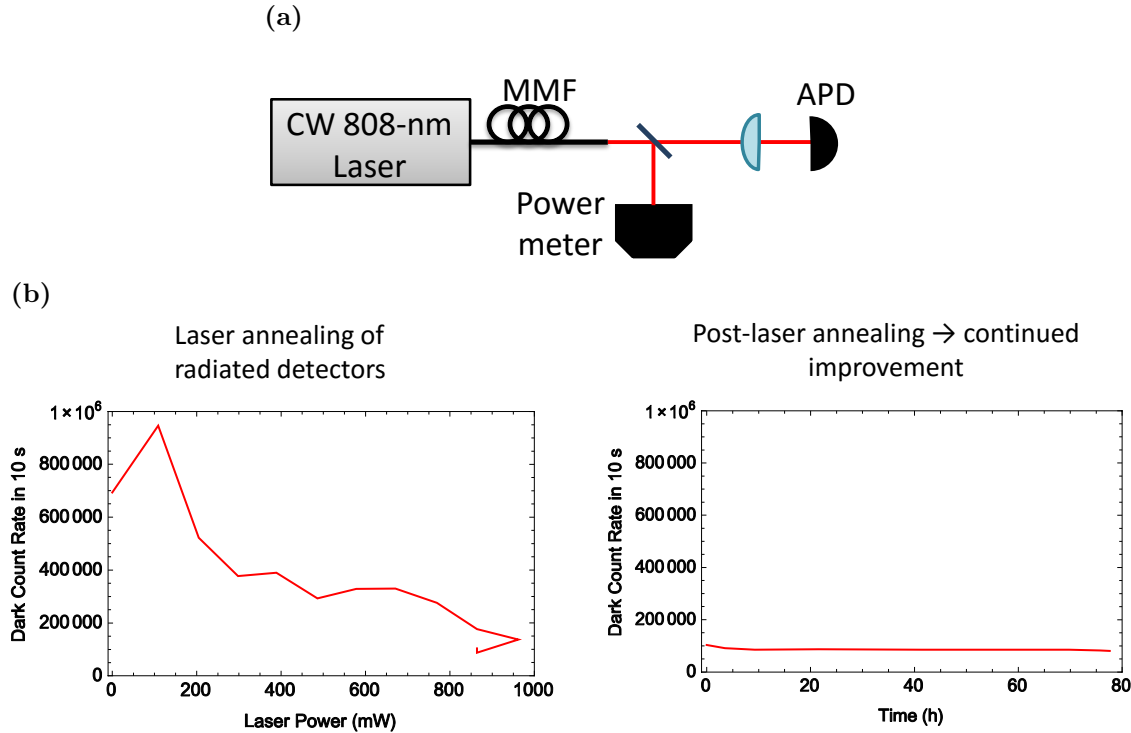


Figure F.1: (a) An 808-nm continuous-wave (CW) laser is used to heat an avalanche photodiode (APD). The power of the laser incident on the photodiode is monitored with a beamsplitter and a power meter. The laser was focused to an $\sim 200\mu\text{m}$ spot on the APD (active area diameter = $50\mu\text{m}$) at varying power levels in 60-s increments. (b) Using this method, the dark-count rate of the APD was permanently reduced from from $\sim 700,000$ counts/ 10s to $10,000$ counts/ 10s .

this technique, we were able to permanently decrease the radiated avalanche photodiode dark counts by a factor of ~ 9 (from $\sim 70,000$ Hz to $\sim 10,000$ Hz), though the rate was still well above the pre-radiated level (400 Hz). Using this technique, a space mission employing avalanche photodiodes might be greatly extended. A much more comprehensive study on several different types of avalanche photodiodes is currently underway at the Institute for Quantum Computing.

Appendix G

Active Stabilization of Interferometers

Interferometers are an important tool for manipulating photonic quantum states. In an interferometer, light in a single beam path is separated into two (or more) beam paths by some variety of beamsplitter (e.g., a non-polarizing beamsplitter, polarizing beam splitter, hologram, etc.). The two beam paths can then be manipulated independently before being recombined with another beam splitter. In the experiments described in the main text, interferometers were used to perform controlled-NOT gates between different photonic degrees of freedom encoded on the same photon. However, the output of an interferometer is very susceptible to small changes in the relative path lengths of the interferometer arms. For example, a relative path length change of just 0.25λ (where λ is the wavelength of the light transmitted through the interferometer) from the target will result in a 50% reduction in the fidelity of the output state. For the wavelength ranges used in most quantum optical experiments (on the scale of 250-1600 nm), small changes in path length due to vibration, air currents, or laboratory temperature changes can be large enough to significantly degrade experimental results.

One strategy to stabilize the path lengths of the interferometers is to isolate the interferometer from all noise sources. Constructing interferometers on floating optical tables in temperature-controlled laboratories can significantly reduce interferometer path length changes. Additional measures, such as using specially designed optics mounts, mounting optical elements on 1"-diameter pedestals (instead of 1/2"-diameter posts), placing a box around the interferometer to reduce air currents, and keeping the interferometer path lengths small, can allow an interferometer to remain stable for hours or days. However, such measures can be costly and time consuming. Additionally, some interferometers, such as unbalanced Mach-Zehnder interferometers (see Sections 2.3 and 4.3), are difficult to stabilize, since their arms can have very different path lengths. Furthermore, the path length difference of some interferometers (such as those described in Section 4.4.1) must be controllably modulated to compensate for other effects in the experimental setup. In such cases, active stabilization is critical.

Actively stabilized interferometers use a feedback system to compensate for any changes in the interferometer path length. In one variety of feedback system, a “stabilization laser” is transmitted through

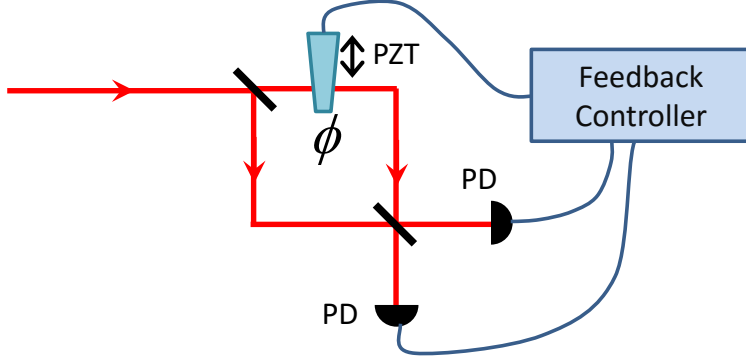


Figure G.1: A basic feedback system for stabilizing an interferometer. The two photodiodes (PD) monitor the output power of the interferometers and are used as inputs into a feedback controller. The feedback controller then drives a piezo-electric actuator (PZT) that changes the phase of the interferometer⁴.

the interferometer system¹ (see Fig. G.1). Any changes in the relative path lengths of the interferometer arms will affect the output state of the stabilization laser; these changes can then be detected using two photodiodes² and then used as an input to a feedback controller. This controller is then used to drive a piezo-electric actuator that modulates the relative path lengths of the interferometer.

To stabilize interferometers in our experiments, we implemented a digital feedback controller a through LabVIEW interterface⁵. The outputs of the two amplified photodiodes⁶ read into the LabVIEW computer interface using a National Instruments NI USB 6211 data acquisition card. The photodiodes were then used to calculate a normalized, time-varying signal:

$$n(I_1, I_2, t) \equiv \frac{I_1(t) - I_2(t)}{I_1(t) + I_2(t)} - \delta, \quad (\text{G.1})$$

where I_1 and I_2 are the two output voltages of the amplified photodiodes and δ is an offset parameter which is used to tune the stabilization set-point (i.e., the phase that the interferometer is stabilized to). This function was then used as a signal for a proportional-integral controller, which sets the voltage on the piezo (V_p) through the following formula:

$$V_p(t) = K_p n(t) + K_i \int_0^t n(t) dt, \quad (\text{G.2})$$

¹The stabilization laser can be kept from influencing the signal by using a different wavelength and/or offsetting the interferometer path. The signal and stabilization light can then be separated using dichroic mirrors or pickoff mirrors.

²Two amplified photodiodes are used to compensate for power drift in the stabilization laser; the feedback signal is the difference of the two divided by the sum.

⁵Feedback controllers can also be implemented using analogue circuits or digitally with FPGAs or microcontrollers. We implemented the feedback controller in LabVIEW for this application to allow simple in-situ phase tuning of the interferometer and feedback parameters. These options allowed us to perform visibility measurements of our signal and set the signal phase.

⁶We used Thorlabs PDA10A amplified photodiodes. If unamplified photodiodes are used, then the output of the photodiodes will be a current signal. This can be converted into a voltage signal using a transimpedance amplifier.

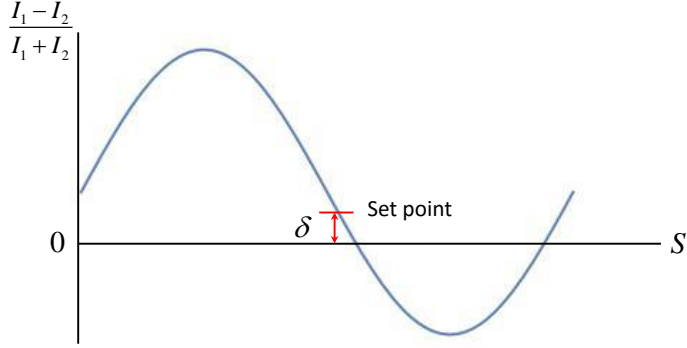


Figure G.2: As the path-length difference between the two interferometer arms S changes, different intensities will be detected by the two photodiodes. The feedback stabilizes the interferometer system at the set point which can be controlled by varying δ .

where K_p and K_i are proportional and integral feedback parameters, respectively. While there are algorithmic methods, such as the Ziegler–Nichols method [162], for tuning these parameters, these algorithms do not necessarily provide optimal interferometer feedback. For example, if the gain parameters are set too high, then sharp impulses (as can occur if the table is bumped) will destabilize the interferometer and can cause a 2π phase shift in the interferometer⁷. Instead, manually tuning K_p and K_i generally yields better results. To do this, we set both of the parameters to zero and then increased K_p until the interferometer corrects impulses quickly, but did not jump between fringes when the system is perturbed. The K_i term was then increased slowly until any remaining “steady-state” error was corrected. Depending on the type of noise in the system, often K_i can be kept small or even zero.

The optimal values of K_p and K_i will change with δ because the intensity of $\frac{dn}{dS}$, where S is the interferometer path length difference, will change for different portions of the interference fringe (see Fig. G.2). The optimal feedback signal sensitivity (and thus optimal feedback performance for correctly tuned K_p and K_i) will occur when $\frac{dn}{dS}$ is maximal i.e., in the steep part of the fringe. This will occur when:

$$\delta = \frac{I_1^{max} + I_1^{min} - I_2^{max} - I_2^{min}}{I_1^{max} + I_1^{min} + I_2^{max} + I_2^{min}}, \quad (\text{G.3})$$

where I^{max} and I^{min} are the minimum and maximum voltage outputs of the amplified photodiodes.

⁷If the stabilization laser is a different wavelength than the signal laser (as is often the case), then a 2π phase shift of the stabilization laser will not cause the same phase shift for the signal.

References

- [1] W. Heisenberg, “Über den anschaulichen inhalt der quantentheoretischen kinematik und mechanik,” *Zeitschrift für Physik*, vol. 43, no. 3-4, pp. 172–198, 1927.
- [2] M. Ozawa, “Universally valid reformulation of the heisenberg uncertainty principle on noise and disturbance in measurement,” *Physical Review A*, vol. 67, no. 4, p. 042105, 2003.
- [3] F. J. MacWilliams and N. J. A. Sloane, *The theory of error correcting codes*. Elsevier, 1977.
- [4] W. K. Wootters and W. H. Zurek, “A single quantum cannot be cloned,” *Nature*, vol. 299, no. 5886, pp. 802–803, 1982.
- [5] C. H. Bennett, G. Brassard, C. Crépeau, R. Jozsa, A. Peres, and W. K. Wootters, “Teleporting an unknown quantum state via dual classical and einstein-podolsky-rosen channels,” *Physical review letters*, vol. 70, no. 13, p. 1895, 1993.
- [6] C. Monroe, D. Meekhof, B. King, W. Itano, and D. Wineland, “Demonstration of a fundamental quantum logic gate,” *Physical Review Letters*, vol. 75, no. 25, p. 4714, 1995.
- [7] L. Isenhower, E. Urban, X. Zhang, A. Gill, T. Henage, T. A. Johnson, T. Walker, and M. Saffman, “Demonstration of a neutral atom controlled-not quantum gate,” *Physical review letters*, vol. 104, no. 1, p. 010503, 2010.
- [8] A. Berkley, H. Xu, R. Ramos, M. Gubrud, F. Strauch, P. Johnson, J. Anderson, A. Dragt, C. Lobb, and F. Wellstood, “Entangled macroscopic quantum states in two superconducting qubits,” *Science*, vol. 300, no. 5625, pp. 1548–1550, 2003.
- [9] F. Jelezko, T. Gaebel, I. Popa, M. Domhan, A. Gruber, and J. Wrachtrup, “Observation of coherent oscillation of a single nuclear spin and realization of a two-qubit conditional quantum gate,” *Physical Review Letters*, vol. 93, no. 13, p. 130501, 2004.
- [10] A. Furusawa, J. L. Sørensen, S. L. Braunstein, C. A. Fuchs, H. J. Kimble, and E. S. Polzik, “Unconditional quantum teleportation,” *Science*, vol. 282, no. 5389, pp. 706–709, 1998.
- [11] I. P. Kaminow, *An Introduction to Electrooptic Devices: Selected Reprints and Introductory Text By*. academic press, 2013.
- [12] M. Pechal, L. Huthmacher, C. Eichler, S. Zeytinoğlu, A. A. Abdumalikov, S. Berger, A. Wallraff, and S. Filipp, “Microwave-controlled generation of shaped single photons in circuit quantum electrodynamics,” *Phys. Rev. X*, vol. 4, no. 4, p. 041010, 2014.
- [13] J. Carolan, C. Harrold, C. Sparrow, E. Martín-López, N. J. Russell, J. W. Silverstone, P. J. Shadbolt, N. Matsuda, M. Oguma, M. Itoh, *et al.*, “Universal linear optics,” *Science*, vol. 349, no. 6249, pp. 711–716, 2015.
- [14] R. Fickler, R. Lapkiewicz, W. N. Plick, M. Krenn, C. Schaeff, S. Ramelow, and A. Zeilinger, “Quantum entanglement of high angular momenta,” *Science*, vol. 338, no. 6107, pp. 640–643, 2012.

- [15] C. Paterson, “Atmospheric turbulence and orbital angular momentum of single photons for optical communication,” *Physical review letters*, vol. 94, no. 15, p. 153901, 2005.
- [16] M. Krenn, R. Fickler, M. Fink, J. Handsteiner, M. Malik, T. Scheidl, R. Ursin, and A. Zeilinger, “Communication with spatially modulated light through turbulent air across vienna,” *New Journal of Physics*, vol. 16, no. 11, p. 113028, 2014.
- [17] N. Bozinovic, Y. Yue, Y. Ren, M. Tur, P. Kristensen, H. Huang, A. E. Willner, and S. Ramachandran, “Terabit-scale orbital angular momentum mode division multiplexing in fibers,” *Science*, vol. 340, no. 6140, pp. 1545–1548, 2013.
- [18] R. Dorn, S. Quabis, and G. Leuchs, “Sharper focus for a radially polarized light beam,” *Physical review letters*, vol. 91, no. 23, p. 233901, 2003.
- [19] G. Milione, T. A. Nguyen, J. Leach, D. A. Nolan, and R. R. Alfano, “Using the nonseparability of vector beams to encode information for optical communication,” *Optics letters*, vol. 40, no. 21, pp. 4887–4890, 2015.
- [20] S. Berg-Johansen, F. Töppel, B. Stiller, P. Banzer, M. Ornigotti, E. Giacobino, G. Leuchs, A. Aiello, and C. Marquardt, “Classically entangled optical beams for high-speed kinematic sensing,” *Optica*, vol. 2, pp. 864–868, Oct 2015.
- [21] K. Nakagawa, A. Iwasaki, Y. Oishi, R. Horisaki, A. Tsukamoto, A. Nakamura, K. Hirosawa, H. Liao, T. Ushida, K. Goda, *et al.*, “Sequentially timed all-optical mapping photography (stamp),” *Nature Photonics*, 2014.
- [22] C. H. Bennett and S. J. Wiesner, “Communication via one-and two-particle operators on einstein-podolsky-rosen states,” *Physical review letters*, vol. 69, no. 20, p. 2881, 1992.
- [23] C. H. Bennett, D. P. DiVincenzo, P. W. Shor, J. A. Smolin, B. M. Terhal, and W. K. Wootters, “Remote state preparation,” *Physical Review Letters*, vol. 87, no. 7, p. 077902, 2001.
- [24] C. Bennett, “G. brassard in proceedings of ieee inter conf,” *On Comp, System and signal processing, Bangalore, India*, 1984.
- [25] M. A. Nielsen and I. L. Chuang, *Quantum computation and quantum information*. Cambridge university press, 2010.
- [26] D. C. Burnham and D. L. Weinberg, “Observation of simultaneity in parametric production of optical photon pairs,” *Physical Review Letters*, vol. 25, no. 2, p. 84, 1970.
- [27] X. Li, P. L. Voss, J. E. Sharping, and P. Kumar, “Optical-fiber source of polarization-entangled photons in the 1550 nm telecom band,” *Physical review letters*, vol. 94, no. 5, p. 053601, 2005.
- [28] P. G. Kwiat, “Nonclassical effects from spontaneous parametric down-conversion adventures in quantum wonderland.,” 1993.
- [29] L. E. Vicent, A. B. U’Ren, R. Rangarajan, C. I. Osorio, J. P. Torres, L. Zhang, and I. A. Walmsley, “Design of bright, fiber-coupled and fully factorable photon pair sources,” *New Journal of Physics*, vol. 12, no. 9, p. 093027, 2010.
- [30] P. G. Kwiat, E. Waks, A. G. White, I. Appelbaum, and P. H. Eberhard, “Ultrabright source of polarization-entangled photons,” *Physical Review A*, vol. 60, no. 2, p. R773, 1999.
- [31] J. Armstrong, N. Bloembergen, J. Ducuing, and P. Pershan, “Interactions between light waves in a nonlinear dielectric,” *Physical Review*, vol. 127, no. 6, p. 1918, 1962.
- [32] S. Sauge, M. Swillo, M. Tengner, and A. Karlsson, “A single-crystal source of path-polarization entangled photons at non-degenerate wavelengths,” *Optics express*, vol. 16, no. 13, pp. 9701–9707, 2008.

- [33] M. Hentschel, H. Hübel, A. Poppe, and A. Zeilinger, “Three-color sagnac source of polarization-entangled photon pairs,” *Optics express*, vol. 17, no. 25, pp. 23153–23159, 2009.
- [34] J. Brendel, N. Gisin, W. Tittel, and H. Zbinden, “Pulsed energy-time entangled twin-photon source for quantum communication,” *Physical Review Letters*, vol. 82, no. 12, p. 2594, 1999.
- [35] J. Franson, “Two-photon interferometry over large distances,” *Physical Review A*, vol. 44, no. 7, p. 4552, 1991.
- [36] J. Rarity and P. Tapster, “Experimental violation of bells inequality based on phase and momentum,” *Physical Review Letters*, vol. 64, no. 21, p. 2495, 1990.
- [37] A. Mair, A. Vaziri, G. Weihs, and A. Zeilinger, “Entanglement of the orbital angular momentum states of photons,” *Nature*, vol. 412, no. 6844, pp. 313–316, 2001.
- [38] S. Walborn, S. Pádua, and C. Monken, “Conservation and entanglement of hermite-gaussian modes in parametric down-conversion,” *Physical Review A*, vol. 71, no. 5, p. 053812, 2005.
- [39] N. K. Langford, R. B. Dalton, M. D. Harvey, J. L. OBrien, G. J. Pryde, A. Gilchrist, S. D. Bartlett, and A. G. White, “Measuring entangled qutrits and their use for quantum bit commitment,” *Physical review letters*, vol. 93, no. 5, p. 053601, 2004.
- [40] S. Walborn, S. Pádua, and C. Monken, “Hyperentanglement-assisted bell-state analysis,” *Physical Review A*, vol. 68, no. 4, p. 042313, 2003.
- [41] W.-B. Gao, C.-Y. Lu, X.-C. Yao, P. Xu, O. Gühne, A. Goebel, Y.-A. Chen, C.-Z. Peng, Z.-B. Chen, and J.-W. Pan, “Experimental demonstration of a hyper-entangled ten-qubit schrödinger cat state,” *Nature Physics*, vol. 6, no. 5, pp. 331–335, 2010.
- [42] A. N. Sharma, K. McCusker, J. Barreiro, and P. G. Kwiat, “Exploring a four-qubit hilbert space using hyperentangled photons,” in *Frontiers in Optics*, pp. FTh3D–5, Optical Society of America, 2015.
- [43] D. Collins, N. Gisin, N. Linden, S. Massar, and S. Popescu, “Bell inequalities for arbitrarily high-dimensional systems,” *Physical review letters*, vol. 88, no. 4, p. 040404, 2002.
- [44] P. W. Shor, J. A. Smolin, and A. V. Thapliyal, “Superactivation of bound entanglement,” *Physical review letters*, vol. 90, no. 10, p. 107901, 2003.
- [45] M. Fujiwara, M. Takeoka, J. Mizuno, and M. Sasaki, “Exceeding the classical capacity limit in a quantum optical channel,” *Physical review letters*, vol. 90, no. 16, p. 167906, 2003.
- [46] M. B. Hastings, “Superadditivity of communication capacity using entangled inputs,” *Nature Physics*, vol. 5, no. 4, pp. 255–257, 2009.
- [47] A. S. Holevo, “Bounds for the quantity of information transmitted by a quantum communication channel,” *Problemy Peredachi Informatsii*, vol. 9, no. 3, pp. 3–11, 1973.
- [48] L. Vaidman and N. Yoran, “Methods for reliable teleportation,” *Physical Review A*, vol. 59, no. 1, p. 116, 1999.
- [49] N. Lütkenhaus, J. Calsamiglia, and K.-A. Suominen, “Bell measurements for teleportation,” *Physical Review A*, vol. 59, no. 5, p. 3295, 1999.
- [50] S. Takeuchi, J. Kim, Y. Yamamoto, and H. H. Hogue, “Development of a high-quantum-efficiency single-photon counting system,” *Applied Physics Letters*, vol. 74, no. 8, pp. 1063–1065, 1999.
- [51] A. J. Miller, S. W. Nam, J. M. Martinis, and A. V. Sergienko, “Demonstration of a low-noise near-infrared photon counter with multiphoton discrimination,” *Applied Physics Letters*, vol. 83, no. 4, pp. 791–793, 2003.

- [52] K. Mattle, H. Weinfurter, P. G. Kwiat, and A. Zeilinger, “Dense coding in experimental quantum communication,” *Physical Review Letters*, vol. 76, no. 25, p. 4656, 1996.
- [53] Z. Zhao, A.-N. Zhang, Y.-A. Chen, H. Zhang, J.-F. Du, T. Yang, and J.-W. Pan, “Experimental demonstration of a nondestructive controlled-not quantum gate for two independent photon qubits,” *Physical review letters*, vol. 94, no. 3, p. 030501, 2005.
- [54] P. Walther and A. Zeilinger, “Experimental realization of a photonic bell-state analyzer,” *Physical Review A*, vol. 72, no. 1, p. 010302, 2005.
- [55] T. Schaetz, M. Barrett, D. Leibfried, J. Chiaverini, J. Britton, W. Itano, J. Jost, C. Langer, and D. Wineland, “Quantum dense coding with atomic qubits,” *Physical review letters*, vol. 93, no. 4, p. 040505, 2004.
- [56] D. Bouwmeester, J.-W. Pan, M. Daniell, H. Weinfurter, and A. Zeilinger, “Observation of three-photon greenberger-horne-zeilinger entanglement,” *Physical Review Letters*, vol. 82, no. 7, p. 1345, 1999.
- [57] J. T. Barreiro, T.-C. Wei, and P. G. Kwiat, “Beating the channel capacity limit for linear photonic superdense coding,” *Nature physics*, vol. 4, no. 4, pp. 282–286, 2008.
- [58] L. Aolita and S. Walborn, “Quantum communication without alignment using multiple-qubit single-photon states,” *Physical review letters*, vol. 98, no. 10, p. 100501, 2007.
- [59] C. Schuck, G. Huber, C. Kurtsiefer, and H. Weinfurter, “Complete deterministic linear optics bell state analysis,” *Physical review letters*, vol. 96, no. 19, p. 190501, 2006.
- [60] T.-C. Wei, J. T. Barreiro, and P. G. Kwiat, “Hyperentangled bell-state analysis,” *Physical Review A*, vol. 75, no. 6, p. 060305, 2007.
- [61] N. Pisenti, C. Gaebler, and T. Lynn, “Distinguishability of hyperentangled bell states by linear evolution and local projective measurement,” *Physical Review A*, vol. 84, no. 2, p. 022340, 2011.
- [62] J. W. Hardy, *Adaptive optics for astronomical telescopes*. Oxford University Press, 1998.
- [63] B. E. Saleh, M. C. Teich, and B. E. Saleh, *Fundamentals of photonics*, vol. 22. Wiley New York, 1991.
- [64] C. H. Bennett, D. P. DiVincenzo, J. A. Smolin, and W. K. Wootters, “Mixed-state entanglement and quantum error correction,” *Physical Review A*, vol. 54, no. 5, p. 3824, 1996.
- [65] D. Bouwmeester, J.-W. Pan, K. Mattle, M. Eibl, H. Weinfurter, and A. Zeilinger, “Experimental quantum teleportation,” *Nature*, vol. 390, no. 6660, pp. 575–579, 1997.
- [66] Y.-H. Kim, S. P. Kulik, and Y. Shih, “Quantum teleportation of a polarization state with a complete bell state measurement,” *Physical Review Letters*, vol. 86, no. 7, p. 1370, 2001.
- [67] R. Ursin, T. Jennewein, M. Aspelmeyer, R. Kaltenbaek, M. Lindenthal, P. Walther, and A. Zeilinger, “Communications: Quantum teleportation across the danube,” *Nature*, vol. 430, no. 7002, pp. 849–849, 2004.
- [68] M. Riebe, H. Häffner, C. Roos, W. Hänsel, J. Benhelm, G. Lancaster, T. Körber, C. Becher, F. Schmidt-Kaler, D. James, *et al.*, “Deterministic quantum teleportation with atoms,” *Nature*, vol. 429, no. 6993, pp. 734–737, 2004.
- [69] M. Barrett, J. Chiaverini, T. Schaetz, J. Britton, W. Itano, J. Jost, E. Knill, C. Langer, D. Leibfried, R. Ozeri, *et al.*, “Deterministic quantum teleportation of atomic qubits,” *Nature*, vol. 429, no. 6993, pp. 737–739, 2004.
- [70] M. Baur, A. Fedorov, L. Steffen, S. Filipp, M. da Silva, and A. Wallraff, “Benchmarking a quantum teleportation protocol in superconducting circuits using tomography and an entanglement witness,” *Physical review letters*, vol. 108, no. 4, p. 040502, 2012.

- [71] W. Pfaff, B. Hensen, H. Bernien, S. B. van Dam, M. S. Blok, T. H. Taminiau, M. J. Tiggelman, R. N. Schouten, M. Markham, D. J. Twitchen, *et al.*, “Unconditional quantum teleportation between distant solid-state quantum bits,” *Science*, vol. 345, no. 6196, pp. 532–535, 2014.
- [72] J. F. Sherson, H. Krauter, R. K. Olsson, B. Julsgaard, K. Hammerer, I. Cirac, and E. S. Polzik, “Quantum teleportation between light and matter,” *Nature*, vol. 443, no. 7111, pp. 557–560, 2006.
- [73] M. Erhard, H. Qassim, H. Mand, E. Karimi, and R. W. Boyd, “Real-time imaging of spin-to-orbital angular momentum hybrid remote state preparation,” *Physical Review A*, vol. 92, no. 2, p. 022321, 2015.
- [74] V. Bužek, M. Hillery, and R. Werner, “Optimal manipulations with qubits: Universal-not gate,” *Physical Review A*, vol. 60, no. 4, p. R2626, 1999.
- [75] N. A. Peters, J. T. Barreiro, M. E. Goggin, T.-C. Wei, and P. G. Kwiat, “Remote state preparation: arbitrary remote control of photon polarization,” *Physical review letters*, vol. 94, no. 15, p. 150502, 2005.
- [76] J. T. Barreiro, T.-C. Wei, and P. G. Kwiat, “Remote preparation of single-photon hybrid entangled and vector-polarization states,” *Physical review letters*, vol. 105, no. 3, p. 030407, 2010.
- [77] D. W. Leung and P. W. Shor, “Oblivious remote state preparation,” *Physical review letters*, vol. 90, no. 12, p. 127905, 2003.
- [78] D. Boschi, S. Branca, F. De Martini, L. Hardy, and S. Popescu, “Experimental realization of teleporting an unknown pure quantum state via dual classical and einstein-podolsky-rosen channels,” *Physical Review Letters*, vol. 80, no. 6, p. 1121, 1998.
- [79] W.-T. Liu, W. Wu, B.-Q. Ou, P.-X. Chen, C.-Z. Li, and J.-M. Yuan, “Experimental remote preparation of arbitrary photon polarization states,” *Physical Review A*, vol. 76, no. 2, p. 022308, 2007.
- [80] W. Rosenfeld, S. Berner, J. Volz, M. Weber, and H. Weinfurter, “Remote preparation of an atomic quantum memory,” *Physical review letters*, vol. 98, no. 5, p. 050504, 2007.
- [81] S. K. Goyal, P. E. Boukama-Dzoussi, S. Ghosh, F. S. Roux, and T. Konrad, “Qudit-teleportation for photons with linear optics,” *Scientific reports*, vol. 4, 2014.
- [82] J.-W. Pan, D. Bouwmeester, H. Weinfurter, and A. Zeilinger, “Experimental entanglement swapping: Entangling photons that never interacted,” *Physical Review Letters*, vol. 80, no. 18, p. 3891, 1998.
- [83] H. J. Bernstein, “Superdense quantum teleportation,” *Quantum Information Processing*, vol. 5, no. 6, pp. 451–461, 2006.
- [84] A. K. Pati, “Minimum classical bit for remote preparation and measurement of a qubit,” *Physical Review A*, vol. 63, no. 1, p. 014302, 2000.
- [85] H.-K. Lo, “Classical-communication cost in distributed quantum-information processing: a generalization of quantum-communication complexity,” *Physical Review A*, vol. 62, no. 1, p. 012313, 2000.
- [86] B. Zeng and P. Zhang, “Remote-state preparation in higher dimension and the parallelizable manifold S^{n-1} ,” *Physical Review A*, vol. 65, no. 2, p. 022316, 2002.
- [87] C.-s. Yu, H.-s. Song, and Y.-h. Wang, “Remote preparation of a qudit using maximally entangled states of qubits,” *Physical Review A*, vol. 73, no. 2, p. 022340, 2006.
- [88] J. Briët, H. Buhrman, M. Laurent, T. Piovesan, and G. Scarpa, “Zero-error source-channel coding with entanglement,” in *The Seventh European Conference on Combinatorics, Graph Theory and Applications*, pp. 157–162, Springer, 2013.

- [89] D. Bruß, M. Cinchetti, G. M. D'Ariano, and C. Macchiavello, “Phase-covariant quantum cloning,” *Physical Review A*, vol. 62, no. 1, p. 012302, 2000.
- [90] J. T. Barreiro, N. K. Langford, N. A. Peters, and P. G. Kwiat, “Generation of hyperentangled photon pairs,” *Physical review letters*, vol. 95, no. 26, p. 260501, 2005.
- [91] D. F. James, P. G. Kwiat, W. J. Munro, and A. G. White, “Measurement of qubits,” *Physical Review A*, vol. 64, no. 5, p. 052312, 2001.
- [92] S. Massar and S. Popescu, “Optimal extraction of information from finite quantum ensembles,” *Physical review letters*, vol. 74, no. 8, p. 1259, 1995.
- [93] G. C. Berkhout, M. P. Lavery, J. Courtial, M. W. Beijersbergen, and M. J. Padgett, “Efficient sorting of orbital angular momentum states of light,” *Physical review letters*, vol. 105, no. 15, p. 153601, 2010.
- [94] D. Bruß and C. Macchiavello, “Optimal state estimation for d-dimensional quantum systems,” *Physics Letters A*, vol. 253, pp. 249–251, 1999.
- [95] S. Barz, E. Kashefi, A. Broadbent, J. F. Fitzsimons, A. Zeilinger, and P. Walther, “Demonstration of blind quantum computing,” *Science*, vol. 335, no. 6066, pp. 303–308, 2012.
- [96] E. Schrödinger, “Probability relations between separated systems,” *Mathematical Proceedings of the Cambridge Philosophical Society*, vol. 32, pp. 446–452, 1936.
- [97] M. F. Pusey, “Negativity and steering: A stronger peres conjecture,” *Physical Review A*, vol. 88, no. 3, p. 032313, 2013.
- [98] P. Skrzypczyk, M. Navascués, and D. Cavalcanti, “Quantifying einstein-podolsky-rosen steering,” *Physical review letters*, vol. 112, no. 18, p. 180404, 2014.
- [99] L. Viola and S. Lloyd, “Dynamical suppression of decoherence in two-state quantum systems,” *Physical Review A*, vol. 58, no. 4, p. 2733, 1998.
- [100] H. Buhrman, R. Cleve, J. Watrous, and R. De Wolf, “Quantum fingerprinting,” *Physical Review Letters*, vol. 87, no. 16, p. 167902, 2001.
- [101] C. Elliott, “Building the quantum network*,” *New Journal of Physics*, vol. 4, no. 1, p. 46, 2002.
- [102] M. Peev, C. Pacher, R. Alléaume, C. Barreiro, J. Bouda, W. Boxleitner, T. Debuisschert, E. Diamanti, M. Dianati, J. Dynes, *et al.*, “The secoqc quantum key distribution network in vienna,” *New Journal of Physics*, vol. 11, no. 7, p. 075001, 2009.
- [103] M. Sasaki, M. Fujiwara, H. Ishizuka, W. Klaus, K. Wakui, M. Takeoka, S. Miki, T. Yamashita, Z. Wang, A. Tanaka, *et al.*, “Field test of quantum key distribution in the tokyo qkd network,” *Optics Express*, vol. 19, no. 11, pp. 10387–10409, 2011.
- [104] D. Stucki, N. Walenta, F. Vannel, R. T. Thew, N. Gisin, H. Zbinden, S. Gray, C. Towery, and S. Ten, “High rate, long-distance quantum key distribution over 250 km of ultra low loss fibres,” *New Journal of Physics*, vol. 11, no. 7, p. 075003, 2009.
- [105] X.-S. Ma, T. Herbst, T. Scheidl, D. Wang, S. Kropatschek, W. Naylor, B. Wittmann, A. Mech, J. Kofler, E. Anisimova, *et al.*, “Quantum teleportation over 143 kilometres using active feed-forward,” *Nature*, vol. 489, no. 7415, pp. 269–273, 2012.
- [106] J. Yin, J.-G. Ren, H. Lu, Y. Cao, H.-L. Yong, Y.-P. Wu, C. Liu, S.-K. Liao, F. Zhou, Y. Jiang, *et al.*, “Quantum teleportation and entanglement distribution over 100-kilometre free-space channels,” *Nature*, vol. 488, no. 7410, pp. 185–188, 2012.
- [107] T. Graham, H. J. Bernstein, H. Javadi, B. Geldzahler, and P. Kwiat, “Superdense teleportation for space applications,” in *SPIE Sensing Technology+ Applications*, pp. 912302–912302, International Society for Optics and Photonics, 2014.

- [108] J. Wang, J.-Y. Yang, I. M. Fazal, N. Ahmed, Y. Yan, H. Huang, Y. Ren, Y. Yue, S. Dolinar, M. Tur, *et al.*, “Terabit free-space data transmission employing orbital angular momentum multiplexing,” *Nature Photonics*, vol. 6, no. 7, pp. 488–496, 2012.
- [109] G. A. Tyler and R. W. Boyd, “Influence of atmospheric turbulence on the propagation of quantum states of light carrying orbital angular momentum,” *Optics letters*, vol. 34, no. 2, pp. 142–144, 2009.
- [110] T. M. Graham, H. J. Bernstein, T.-C. Wei, M. Junge, and P. G. Kwiat, “Superdense teleportation using hyperentangled photons,” *Nature Communications*, vol. 6, 2015.
- [111] B. Fang, O. Cohen, M. Liscidini, J. E. Sipe, and V. O. Lorenz, “Fast and highly resolved capture of the joint spectral density of photon pairs,” *Optica*, vol. 1, no. 5, pp. 281–284, 2014.
- [112] R. W. Boyd, *Nonlinear optics*. Academic press, 2003.
- [113] J.-P. Bourgoin, B. L. Higgins, N. Gigov, C. Holloway, C. J. Pugh, S. Kaiser, M. Cranmer, and T. Jennewein, “Free-space quantum key distribution to a moving receiver,” *Optics Express*, vol. 23, no. 26, pp. 33437–33447, 2015.
- [114] J.-P. Bourgoin, *Experimental and theoretical demonstration of the feasibility of global quantum cryptography using satellites*. PhD thesis, University of Waterloo, 2014.
- [115] J. Jin, S. Agne, J.-P. Bourgoin, L. N. Zhang, Yanbao, and T. Jennewein, “Efficient time-bin qubit analyzer compatible with multimode optical channels,” *arXiv preprint arXiv:1509.07490*, 2015.
- [116] E. Hecht, *Optics*. Addison-Wesley, 2002.
- [117] L. C. Andrews and R. L. Phillips, *Laser beam propagation through random media*, vol. 52. SPIE press Bellingham, WA, 2005.
- [118] J. Altepeter, E. Jeffrey, P. Kwiat, S. Tanzilli, N. Gisin, and A. Acín, “Experimental methods for detecting entanglement,” *Physical review letters*, vol. 95, no. 3, p. 033601, 2005.
- [119] F. Marsili, V. Verma, J. Stern, S. Harrington, A. Lita, T. Gerrits, I. Vayshenker, B. Baek, M. Shaw, R. Mirin, *et al.*, “Detecting single infrared photons with 93% system efficiency,” *Nature Photonics*, vol. 7, no. 3, pp. 210–214, 2013.
- [120] X. Sun, M. A. Krainak, J. B. Abshire, J. D. Spinhirne, C. Trottier, M. Davies, H. Dautet, G. R. Allan, A. T. Lukemire, and J. C. Vandiver, “Space-qualified silicon avalanche-photodiode single-photon-counting modules,” *Journal of Modern Optics*, vol. 51, no. 9-10, pp. 1333–1350, 2004.
- [121] M. Marisaldi, P. Maccagnani, F. Moscatelli, C. Labanti, F. Fuschino, M. Prest, A. Berra, D. Bolognini, M. Ghioni, I. Rech, *et al.*, “Single photon avalanche diodes for space applications,” in *Nuclear Science Symposium and Medical Imaging Conference (NSS/MIC), 2011 IEEE*, pp. 129–134, IEEE, 2011.
- [122] G. Fujii, N. Namekata, M. Motoya, S. Kurimura, and S. Inoue, “Bright narrowband source of photon pairs at optical telecommunication wavelengths using a type-II periodically poled lithium niobate waveguide,” *Optics express*, vol. 15, no. 20, pp. 12769–12776, 2007.
- [123] N. Gisin, G. Ribordy, W. Tittel, and H. Zbinden, “Quantum cryptography,” *Reviews of modern physics*, vol. 74, no. 1, p. 145, 2002.
- [124] D. J. MacKay and R. M. Neal, “Near shannon limit performance of low density parity check codes,” *Electronics letters*, vol. 32, no. 18, pp. 1645–1646, 1996.
- [125] C. H. Bennett, G. Brassard, C. Crépeau, and U. M. Maurer, “Generalized privacy amplification,” *Information Theory, IEEE Transactions on*, vol. 41, no. 6, pp. 1915–1923, 1995.
- [126] I. Ali-Khan, C. J. Broadbent, and J. C. Howell, “Large-alphabet quantum key distribution using energy-time entangled bipartite states,” *Physical review letters*, vol. 98, no. 6, p. 060503, 2007.

- [127] M. Mohseni and D. Lidar, “Direct characterization of quantum dynamics,” *Physical review letters*, vol. 97, no. 17, p. 170501, 2006.
- [128] M. Mohseni, A. Rezakhani, and D. Lidar, “Quantum-process tomography: Resource analysis of different strategies,” *Physical Review A*, vol. 77, no. 3, p. 032322, 2008.
- [129] A. Bendersky, F. Pastawski, and J. P. Paz, “Selective and efficient estimation of parameters for quantum process tomography,” *Physical review letters*, vol. 100, no. 19, p. 190403, 2008.
- [130] I. Ivonovic, “Geometrical description of quantal state determination,” *Journal of Physics A: Mathematical and General*, vol. 14, no. 12, p. 3241, 1981.
- [131] G. M. D’Ariano, “Universal quantum observables,” *Physics Letters A*, vol. 300, no. 1, pp. 1–6, 2002.
- [132] Z.-W. Wang, Y.-S. Zhang, Y.-F. Huang, X.-F. Ren, and G.-C. Guo, “Experimental realization of direct characterization of quantum dynamics,” *Physical Review A*, vol. 75, no. 4, p. 044304, 2007.
- [133] J. T. Barreiro, T.-C. Wei, and P. G. Kwiat, “Beating the channel capacity limit for linear photonic superdense coding,” *Nature physics*, vol. 4, no. 4, pp. 282–286, 2008.
- [134] W.-T. Liu, W. Wu, P.-X. Chen, C.-Z. Li, and J.-M. Yuan, “Direct characterization of quantum dynamics with single-photon two-qubit states,” *Physical Review A*, vol. 77, no. 3, p. 032328, 2008.
- [135] D. Nigg, J. T. Barreiro, P. Schindler, M. Mohseni, T. Monz, M. Chwalla, M. Hennrich, and R. Blatt, “Experimental characterization of quantum dynamics through many-body interactions,” *Physical review letters*, vol. 110, no. 6, p. 060403, 2013.
- [136] I. L. Chuang and M. A. Nielsen, “Prescription for experimental determination of the dynamics of a quantum black box,” *Journal of Modern Optics*, vol. 44, no. 11-12, pp. 2455–2467, 1997.
- [137] J. B. Altepeter, D. Branning, E. Jeffrey, T. Wei, P. G. Kwiat, R. T. Thew, J. L. O’Brien, M. A. Nielsen, and A. G. White, “Ancilla-assisted quantum process tomography,” *Physical Review Letters*, vol. 90, no. 19, p. 193601, 2003.
- [138] M. Mohseni, A. Rezakhani, J. Barreiro, P. Kwiat, and A. Aspuru-Guzik, “Quantum process estimation via generic two-body correlations,” *Physical Review A*, vol. 81, no. 3, p. 032102, 2010.
- [139] N. A. Peters, J. T. Barreiro, M. E. Goggin, T.-C. Wei, and P. G. Kwiat, “Remote state preparation: arbitrary remote control of photon polarization,” *Physical review letters*, vol. 94, no. 15, p. 150502, 2005.
- [140] J. Altepeter, E. Jeffrey, P. Kwiat, S. Tanzilli, N. Gisin, and A. Acín, “Experimental methods for detecting entanglement,” *Physical review letters*, vol. 95, no. 3, p. 033601, 2005.
- [141] M. D. de Burgh, N. K. Langford, A. C. Doherty, and A. Gilchrist, “Choice of measurement sets in qubit tomography,” *Physical Review A*, vol. 78, no. 5, p. 052122, 2008.
- [142] S. Walborn, S. Pádua, and C. Monken, “Hyperentanglement-assisted bell-state analysis,” *Physical Review A*, vol. 68, no. 4, p. 042313, 2003.
- [143] S. B. L. Allen and M. Padgett, *Optical Angular Momentum*. Taylor & Francis, London, 2003.
- [144] A. Shaham and H. Eisenberg, “Realizing controllable depolarization in photonic quantum-information channels,” *Physical Review A*, vol. 83, no. 2, p. 022303, 2011.
- [145] A. Gilchrist, N. K. Langford, and M. A. Nielsen, “Distance measures to compare real and ideal quantum processes,” *Physical Review A*, vol. 71, no. 6, p. 062310, 2005.
- [146] M. Mohseni, A. T. Rezakhani, and A. Aspuru-Guzik, “Direct estimation of single-and two-qubit hamiltonians and relaxation rates,” *Physical Review A*, vol. 77, no. 4, p. 042320, 2008.

- [147] D. Gross, Y.-K. Liu, S. T. Flammia, S. Becker, and J. Eisert, “Quantum state tomography via compressed sensing,” *Physical review letters*, vol. 105, no. 15, p. 150401, 2010.
- [148] A. Shabani, R. Kosut, M. Mohseni, H. Rabitz, M. Broome, M. Almeida, A. Fedrizzi, and A. White, “Efficient measurement of quantum dynamics via compressive sensing,” *Physical review letters*, vol. 106, no. 10, p. 100401, 2011.
- [149] K. Chen, C.-M. Li, Q. Zhang, Y.-A. Chen, A. Goebel, S. Chen, A. Mair, and J.-W. Pan, “Experimental realization of one-way quantum computing with two-photon four-qubit cluster states,” *Physical review letters*, vol. 99, no. 12, p. 120503, 2007.
- [150] U. Levy, C.-H. Tsai, L. Pang, and Y. Fainman, “Engineering space-variant inhomogeneous media for polarization control,” *Optics letters*, vol. 29, no. 15, pp. 1718–1720, 2004.
- [151] S. L. Braunstein and C. M. Caves, “Statistical distance and the geometry of quantum states,” *Physical Review Letters*, vol. 72, no. 22, pp. 3439–3443, 1994.
- [152] F. Hausdorff, “Dimension und äußeres maß,” *Mathematische Annalen*, vol. 79, no. 1-2, pp. 157–179, 1918.
- [153] H. Minkowski, “Gesammelte abhandlungen von hermann minkowski, unter mitwirkung von andreas speiser und hermann weyl hrsg. von david hilbert,” 1911.
- [154] D. de Laat, F. M. de Oliveira Filho, and F. Vallentin, “Upper bounds for packings of spheres of several radii,” in *Forum of Mathematics, Sigma*, vol. 2, p. e23, Cambridge Univ Press, 2014.
- [155] B. Brown and A. Lohmann, “Computer-generated binary holograms,” *IBM Journal of research and Development*, vol. 13, no. 2, pp. 160–168, 1969.
- [156] R. W. Gerchberg, “A practical algorithm for the determination of phase from image and diffraction plane pictures,” *Optik*, vol. 35, p. 237, 1972.
- [157] M. Pasienski and B. DeMarco, “A high-accuracy algorithm for designing arbitrary holographic atom traps,” *Optics express*, vol. 16, no. 3, pp. 2176–2190, 2008.
- [158] K. Zielnicki, *Pure sources and efficient detectors for optical quantum information processing*. PhD thesis, UNIVERSITY OF ILLINOIS AT URBANA-CHAMPAIGN, 2014.
- [159] J. B. Altepeter, *Testing the limits of nonlocality*. PhD thesis, Ph. D. thesis, University of Illinois at Urbana-Champaign, Urbana, IL, 2006.
- [160] R. Blume-Kohout, “Optimal, reliable estimation of quantum states,” *New Journal of Physics*, vol. 12, no. 4, p. 043034, 2010.
- [161] A. N. Bugge, S. Sauge, A. M. M. Ghazali, J. Skaar, L. Lydersen, and V. Makarov, “Laser damage helps the eavesdropper in quantum cryptography,” *Physical review letters*, vol. 112, no. 7, p. 070503, 2014.
- [162] J. G. Ziegler and N. B. Nichols, “Optimum settings for automatic controllers,” *trans. ASME*, vol. 64, no. 11, 1942.